Modeling and performance analysis of chalcogenide prism based plasmonic biosensor comprising of gold nanoparticle film

Kaushik Brahmachari, Mina Ray*
Department of Applied Optics and Photonics, University of Calcutta,
Technology Campus, JD-2, Sector-III, Salt Lake City, Kolkata, India- 700 098

ABSTRACT

In this work, admittance loci method is used to model and analyze performance of a chalcogenide prism based plasmonic biosensor comprising of gold metal nanoparticle film for detection of wavelength dependent refractive index change of human blood sample under angular interrogation mode. The wavelength dependent performance of the plasmonic biosensor based on the choice of chalcogenide (2S2G) as a coupling prism material has been discussed with the help of Figure-of-Merit (FOM) plot.

Keywords: Admittance loci method, plasmonic biosensors, chalcogenide (2S2G), human blood sample, FOM

1. INTRODUCTION

In a prism coupler based plasmonic configuration, an incident p-polarized light interacts with surface plasmon wave which propagates along metal-dielectric interface resulting occurrence of surface plasmon resonance (SPR)[1]. Admittance loci based method is very useful for modeling multilayer optical thin film structures[2] and it has been used to model chalcogenide (2S2G) prism based plasmonic bio sensing structures for sensing purposes[3-6]. A work on human blood group detection based on SPR has been reported[7]. Performance of plasmonic sensor with different bimetallic nanoparticle alloy combinations has been demonstrated earlier[8,9].

In this work, we have modeled a chalcogenide prism based plasmonic biosensor using admittance loci approach and analyzed its performance in terms of Figure-of-Merit (FOM).

2. THEORETICAL BACKGROUND

A plasmonic biosensor can be modeled using admittance loci method where the Virtual Reference Plane (VRP) moves from the sample and ends at the front surface (prism) of the plasmonic biosensor structure. Figure1 shows schematic diagram of a plasmonic biosensor structure consisting of chalcogenide prism, gold metal nanoparticle film and biosample (human blood) with refractive indices represented by n_p, n_m and n_{sample} respectively.

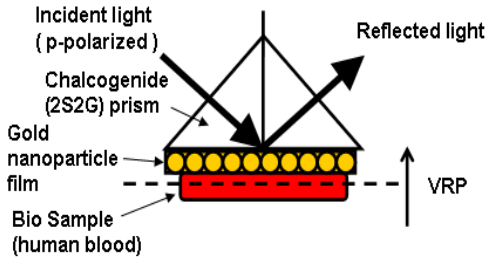

Figure 1. Schematic diagram of an admittance loci design based structure of a plasmonic biosensor.

*mraphy@caluniv.ac.in; phone +91 33 23522411; caluniv.ac.in

The dielectric constant of gold at different wavelength (λ) has been calculated using Drude model as

$$\varepsilon_m(\lambda) = 1 - \frac{\lambda^2}{\lambda_p^2(1 + i\frac{\lambda}{\lambda_c})} \tag{1}$$

where λ_p, λ_c are the plasma wavelength and collision wavelength respectively.

The inverse of collision wavelength as a function of particle size ($R_{particle}$) is given by

$$\frac{1}{\lambda_c(R_{particle})} = \frac{1}{\lambda_c(bulk)} + \frac{v_f}{2\pi c R_{particle}} \tag{2}$$

where λ_c (bulk) is the bulk collision wavelength, c is the velocity of light in free space and v_f is the Fermi velocity. The values of plasma wavelength, bulk collision wavelength and Fermi velocity of gold are taken from literature[8].

The phase introduced by the gold metal nanoparticle film is given by

$$\delta_m = \left(\frac{2\pi}{\lambda}\right) d_m \left(n_m^2 - k_m^2 - n_p^2 \sin^2\theta_i - 2in_m k_m\right)^{1/2} \tag{3}$$

where, n_m, k_m are the real and imaginary part of the complex refractive index of gold metal, n_p is the refractive index of prism material, d_m is the thickness of the gold metal nanoparticle film, λ is the wavelength of incident light and θ_i is the angle of incidence.

The admittance of a plasmonic biosensor can be written as

$$Y = \frac{\eta_{sample}\cos\delta_m + i\eta_m \sin\delta_m}{\cos\delta_m + i(\eta_{sample}/\eta_m)\sin\delta_m} \tag{4}$$

The reflectance of a plasmonic biosensor is given by

$$R = \left(\frac{\eta_p - Y}{\eta_p + Y}\right)\left(\frac{\eta_p - Y}{\eta_p + Y}\right)^* \tag{5}$$

In above equations, η_p, η_m, η_{sample} are the admittances of prism, gold metal film and biosample respectively.

The resonance condition is given by

$$Kn_p \sin\theta_{SPR} = K\sqrt{\frac{\varepsilon_{mr} n_{sample}^2}{\varepsilon_{mr} + n_{sample}^2}} \tag{6}$$

where, ε_{mr} is the real part of dielectric constant of gold metal and K is the free space wave number.

The Figure-of-Merit (FOM) of a plasmonic biosensor can be written as

$$FOM = \frac{S}{FWHM} \tag{7}$$

where, S is the sensitivity and $FWHM$ (Full Width Half Maximum) is the half width of SPR sensing curve.

3. RESULTS AND DISCUSSION

Admittance loci plots of a plasmonic biosensor structure using gold metal nanoparticle film having nanoparticle sizes of 6 nm and 8 nm at 700 nm and 800 nm wavelengths are shown in figure 2(a) and in figure 2(b). The wavelength dependent refractive index of chalcogenide (2S2G) has been taken from[3]. Here, human blood has been taken as a biosample for sensing purpose[7]. From figure 2(a) at 700 nm wavelength for gold nanoparticle size of 6 nm, it is seen that the starting admittance for the gold nanoparticle film is on the imaginary axis. The locus point moves from 2.793i on imaginary axis corresponding to gold film thickness of 0 nm and ends at 2.38 (close to refractive index of chalcogenide prism 2.3291 at 700 nm wavelength) on real axis corresponding to gold film thickness of 39.6 nm for an angle of incidence of 39.18°, which indicates effective plasmon excitation. The calculated values of starting and ending admittances and incident angles for two wavelengths are tabulated in Table 1.

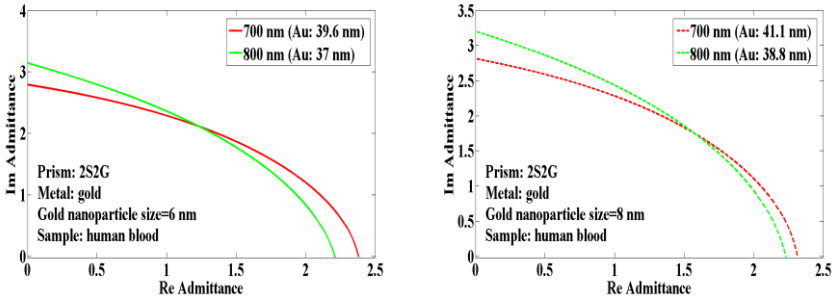

Figure 2. Admittance loci plots of a chalcogenide prism based plasmonic biosensor at 700 nm and 800 nm wavelengths for gold nanoparticle sizes of (a) 6 nm and (b) 8 nm.

Table 1. Admittance related parameters for 2S2G prism based plasmonic biosensor

Wavelength (nm)	Gold nanoparticle size (in nm)	Thickness of gold metal film (in nm)	Starting imaginary admittance	End admittance	Angle of incidence (in degrees)
700	6	39.6	2.793i	2.38, -0.008624i	39.18
	8	41.1	2.814i	2.314, -0.005287i	39.14
800	6	37	3.145i	2.213, -0.01712i	38.93
	8	38.8	3.203i	2.232, -0.01242i	38.85

SPR sensing curves of a chalcogenide prism based plasmonic biosensor for gold nanoparticle sizes of 6 nm and 8 nm at 700 nm and 800 nm wavelengths are shown in figure 3(a), which reveals that plasmonic biosensor using bigger sized gold nanoparticles displays narrower SPR curves compared to sensor using smaller sized gold nanoparticles. Figure 3(b) depicts the Figure-of-Merit (FOM) plot for gold nanoparticle sizes of 6 nm and 8 nm respectively. It is evident that sensor using bigger sized gold nanoparticles show higher FOM than sensor using smaller sized gold nanoparticles. So, our FOM plot suggests using bigger sized gold nanoparticles for more accurate SPR sensing.

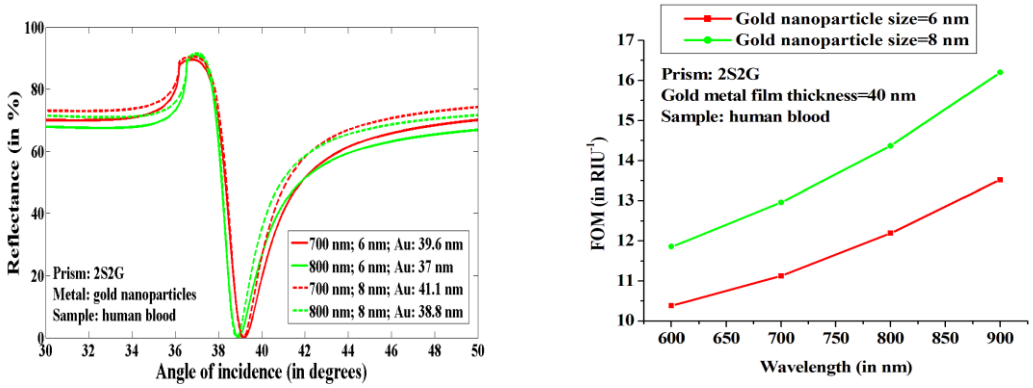

Figure 3. (a) SPR sensing curves and (b) FOM plot for gold nanoparticle sizes of 6 nm and 8 nm of a chalcogenide prism based plasmonic bio sensor.

4. CONCLUDING REMARKS

In this report, we have modeled and analyzed the wavelength dependent performance of chalcogenide (2S2G) prism based plasmonic biosensor using admittance loci method. Simulated admittance loci plots have shown efficient plasmon excitation due to closeness of real part of end admittance value to the actual refractive index value of chalcogenide prism material. Simulated SPR sensing curves recommend using bigger sized gold metal nanoparticles for more accurate plasmonic dip position determination. It is seen from our simulated FOM plot that as wavelength increases, FOM also increases. So, we recommend operating the biosensor at higher wavelength region rather than to operate it at lower wavelength region in order to achieve better performance.

ACKNOWLEDGEMENTS

Authors wish to acknowledge Centre for Research in Nanoscience and Nanotechnology (CRNN), University of Calcutta. Kaushik Brahmachari is grateful to Technical Education Quality Improvement Programme (TEQIP PHASE II), University College of Technology, University of Calcutta for awarding Senior Research Assistantship to carry out this work.

REFERENCES

[1] Otto, A., "Excitation of nonradiative surface plasma waves in silver by the method of frustrated total reflection", Z. Phys. 216, 398-410 (1968).
[2] Macleod, A. H., [Thin-Film Optical Filters], CRC Press Publishers, New York, 403-425 (2010).
[3] Brahmachari, K., Ray, M., "Modelling of chalcogenide glass based plasmonic structure for chemical sensing using near infrared light", Optik - Int. J. Light Electron Opt. 124(21), 5170-5176 (2013).
[4] Brahmachari, K., Ray, M., "Performance of admittance loci based design of plasmonic sensor at infrared wavelength", Opt. Eng. 52(8), 087112-1-8 (2013).
[5] Brahmachari, K., Ray, M., "Admittance loci based design of nanoplasmonic sensor using ceramic and chalcogenide materials", Sens. Actuators A: Phys. 212, 102-109 (2014).
[6] Brahmachari, K., Ray, M., "Admittance loci based design of a nanobioplasmonic sensor and its performance analysis", Sens. Actuators B: Chem. 208, 283-290 (2015).
[7] Sharma K. A., Jha, R., Pattanaik, S. H., "Design considerations for surface plasmon resonance based detection of human blood group in near infrared", J. Appl. Phys. 107, 034701-1-7 (2010).
[8] Sharma K. A., Mohr J. G., "On the performance of surface plasmon resonance based fibre optic sensor with different bimetallic nanoparticle alloy combinations", J. Phys. D: Appl. Phys. 41, 0551061-7 (2008).
[9] Brahmachari, K., Ray, M., "Admittance loci based design of a plasmonic structure using Ag-Au bimetallic alloy film", ISRN Optics, 2013, 946832-1-7 (2013).

Michelson Interferometer based liquid refractive index sensor using micro fiber

Vanita Bhardwaj*, Rahul Kumar Gangwar and Vinod Kumar Singh
Department of Applied Physics, Indian School of Mines, Dhanbad 826004, India
*Email Id: bhardwajphyism@gmail.com

Abstract

In this article a liquid refractive index sensor based on Michelson Interferometer is fabricated in which the interference occurs due to Fresnel reflections from coupler ends. The two sensing probes are immersed in the solvent and solution and their corresponding power is obtained from Optical Spectrum Analyzer (OSA). In this experiment the sensitivity of the Michelson Interferometer based liquid refractive index sensor is measured. The experimental result shows that the sensitivity of this proposed sensor with sensing length of 20cm is 762.4 dBm/RIU.

Key Words: Optical sensors, Refractive index sensor, micro fiber, Optical spectrum analyzer.

1. Introduction

In the past few years the refractive Index sensor and its usefulness in various applications have got wide interest of researchers [1]. Many refractive index sensors are fabricated using different techniques for example Fabry Perot Interferometers (FPT) [2], Mach Zehnder interferometer [3] and Michelson Interferometer [4], in which researcher are used different types of optical fibers like Fiber Brag Grating (FBG) [5], Long period fiber gratings (LPFG) [6], Surface Plasmon resonance (SPR) [7], Photonic crystal fiber (PCF) [8] etc.

In the field of chemical sensing [9], biological sensing [10], optical communication [11] and optical sensors, Interferometric method is one of the important methods to measure refractive index. Optical fiber sensor based on Michelson Interferometer have a lot of advantages and widely used in many applications such as temperature sensor, Refractive index sensor.

In this paper, we present a Michelson Interferometer based liquid refractive index sensor using micro fiber .The interference spectrum was generated by Michelson Interferometer. Fresnel reflection gives two interfering waves obtained from the ends of the couplers. Refractive index for different liquids can be derived by calculating fringe contrast of the interference pattern from the reflected spectrum. The RI sensitivity and fringe contrast of the new sensor are 762.4 dBm/RIU and 89.75 respectively.

2. Sensor configuration and principle

In this article we demonstrate a liquid refractive index sensor using micro fiber to measure the refractive index of sodium chloride solution (NaCl) at different concentration by calculating fringe contrast variations of a fiber Michelson Interferometer. The two sensing probes, one of which is immersed in water acts as a reference head and the second probe is immersed in NaCl solution acts as a sensing head, are used in this experiment. The Fresnel reflection obtained from fiber and liquid interface will change according to the change in refractive index of liquid.

The experiment set up used to perform this experiment is shown in fig 1. This set up contains laser source having operating wavelength 1550 nm, two optical fibers probes with sensing ends, 2×2 3dB fiber optic coupler, optical

spectrum analyzer (OSA) and NaCl solution of different concentrations. The light sent from the laser source was split into two beams (beam 3 and beam 4) first by the coupler and second reflected beam by the sensor-solution interface. Both reflected light interfered at the coupler and detected by OSA.

The reflected intensity of the beam 3 is obtained by Fresnel equation:

$$I_{3R}(\lambda) = \frac{1}{2}\left(\frac{n_f - n_{x0}}{n_f + n_{x0}}\right)^2 I_0(\lambda) \qquad (1)$$

Similarly, the reflected intensity of beam 4 is given by

$$I_{4R}(\lambda) = \frac{1}{2}\left(\frac{n_f - n_x}{n_f + n_x}\right)^2 \qquad (2)$$

Where $I_0(\lambda)$the output intensity of the Laser is source and n_f is the refractive index of the fiber core, n_{xo} and n_x is the refractive indices of the solvent and solution, respectively.

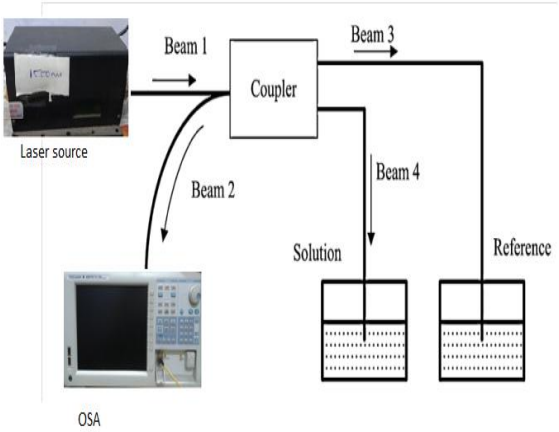

Fig. 1. Experimental set up for Liquid Refractive Index sensor

The interference pattern of the liquid is shown in Fig 2a is observed reflection spectra of the sensor for sodium chloride solution with variation of its refractive index by changing mass concentration.
From Eq.(3), the maximum and minimum of the $I_2(\lambda)$ can be obtained as follows:

$$I_{2max}(\lambda) = I_{3R}(\lambda) + \frac{1}{2} I_{4R}(\lambda) + 2\sqrt{\frac{1}{2} I_{3R}(\lambda) \frac{1}{2} I_{4R}(\lambda)} \qquad (5)$$

$$I_{2min}(\lambda) = \frac{1}{2} I_{3R}(\lambda) + \frac{1}{2} I_{4R}(\lambda) - 2\sqrt{\frac{1}{2} I_{3R}(\lambda) \frac{1}{2} I_{4R}(\lambda)} \qquad (6)$$

The corresponding fringe contrast is given by

$$\text{V}=10\log_{10}\left[\frac{I_{2max}}{I_{2min}}\right] = 10\log_{10}\left[\frac{n_f^2 - n_{xo}\, n_x}{n_f(n_{xo} - n_x)}\right]^2 \qquad (7)$$

3. Experimental result and discussion

The observed spectrum of the proposed sensor is shown in fig. 2 (a). The variation of fringe contrast V with the RI of the solution n_x is shown in fig 3. As shown in fig 2(b), with increase in n_x fringe contrast V decreases (when $n_x > n_{xo}$). With the decreasing solution concentration the resolution of sensor increases.

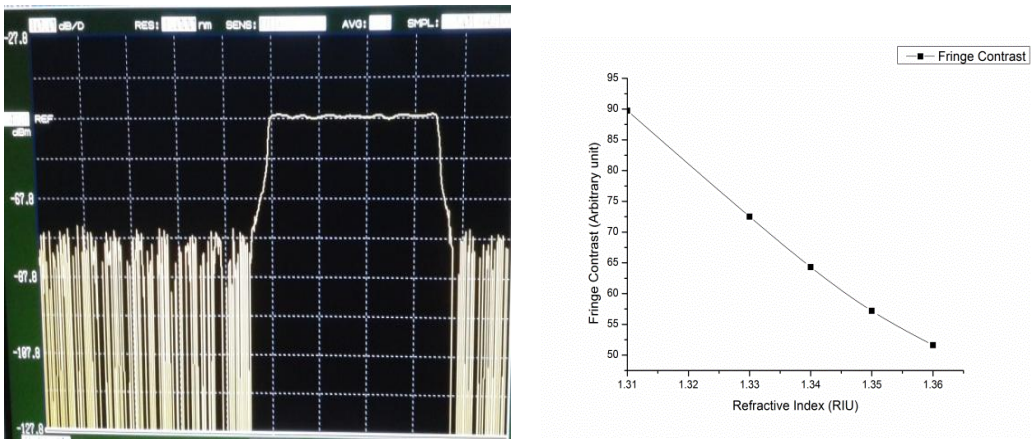

(a) (b)

Fig. 2. (a) Measured spectral response of the sensing system in sodium chloride, (b) The measured fringe contrast variation with refractive index

In this experiment 2×2 3dB coupler was used. The length of arm 3 and 4 of the coupler is kept about 80cm.The fibers used in this experiment is multimode fibers and the reflective spectra were observed from OSA. In our performed experiments, the reference head and the sensor head were immersed into distilled water and sodium chloride solutions, respectively. The refractive index of solution varies with variation of its mass concentrations and the solutions of known concentrations were prepared before measurement. After each and every measurement, the sensing fiber ends were cleaned with distilled water or ethanol and then immersed in another liquid. The range of refractive index changes from 1.31 to 1.36. The sensitivity of this refractive index sensor is found to be 762.4 dBm/RIU.

The comparison of experimental and theoretical result of fringe contrast is shown in fig. 3.

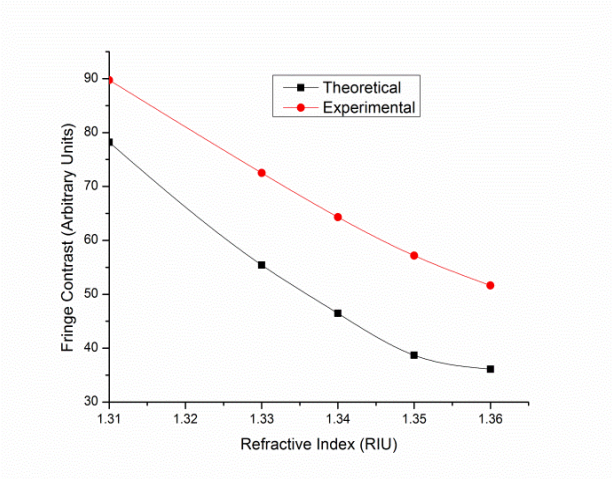

Fig. 3. Variation of Fringe contrast with Refractive Index.

IV. Conclusion

In the present work, the fringe contrast of the fabricated sensor based on Michelson interferometer decreases with increasing refractive index of solution. The sensitivity of this sensor is 762.4 dBm/RIU. The performance of sensor may be improved by increasing fringe contrast, which can be achieved by increasing the sensing length or by replacing normal coupler to the polarization maintaining fiber coupler. The sensor could be find wide range of physical, chemical and biological applications.

Acknowledgement

This work is supported by Department of Applied Physics, Indian School Of Mines, Dhanbad.

References

[1] G. Tsigarids, D. Polyzos, Ailaonnou, M. Fakis, P. Persephonics, "Theoretical and experimental study of RI sensors based on etched fiber bragg gratings," IEEE Photonics 209, 9-15 (2014).

[2] Ming-shun Jiang, Qing-mei Sui, Zhong-wei Jin, Fa-ye Zhang, Lei Jia, "Temperature-independent optical fiber Fabry–Perot refractive-index sensor based on hollow-core photonic crystal fiber," Optik, 125, 3295-3298 (2014).

[3] Huaqing Yua,b,n, Liangbin Xionga, hihong Chena, Qianguang Li a, Xunong Yi a, Yu Dingc,Feng Wangc, Hao Lva, Yaoming Dinga, "Ultracompact and high sensitive refractive index sensor based on Mach–Zehnder interferometer," Optics and Laser in Engineering, 56, 50-53 (2014).

[4] Hongyun Meng, Wei Shen, Guanbin Zhang, Xiaowei Wu, Wei Wang, Chunhua Tan, Xuguang Huang,"Michelson interferometer-based fiber-optic sensing of liquid refractive index," Sensors and Actuators B: Chemical 160, 720-723 (2011).

[5] P. Moyo, J.M.W. Brownjohn, R.Suresh, S.C.Tjin, "Development of fiber bragg grating sensor for monitoring civil infrastructure," Engineering Structures 27, 1828-1834 (2005).

[6] Chunying Guana,b, Xiaozhong Tiana, Shuqiang Lia, Xing Zhonga, Jinhui Shia, Libo Yuana, "Long period fiber grating and high sensitivity refractive index sensor based on hollow eccentric optical fiber," Sensors and Actuators B: Chemical 188, 768-771 (2013).

[7] Gaurav Guptaa, Mitsunori Sugimotob, Yoshikazu Matsuic, Jun Kondoha, **"**Use of a low refractive index prism in surface Plasmon resonance biosensing," Sensors and Actuators B: Chemical 130, 689-695 (2007).

[8] Shuyan Zhang, Xia Yu, Ying Zhang,Ping Shum, Yating Zhang, Li Xia, and Deming Liu, "Theoretical Study of Dual-Core Photonic Crystal Fibers With Metal Wire," IEEE Photonics, 4, 1178 (2012).

[9] Arunava Mukherjeea et al., "Characterization of a fiber optic liquid refractive index sensor," Sensors and Actuators B:Chemical 145, 265-271 (2009).

[10] Angela Leunga, P. Mohana Shankarb, Raj Mutharasan, "A review of fiber-optic biosensors," Sensors and Actuators B: Chemical 125, 688-703 (2007).

[11] Tao Zhanga, Guoying Fenga, Zheyi Songa, Shouhuan Zhoua, "A single-element interferometer for measuring refractive index of transparent liquids," Optics Communication, Article in press.

Spatially Bessel modulated nonlinear optical similaritons in asymmetric twin-core fibers

Thokala Soloman Raju * and T. Bibiya Nancy †
Department of Physics, Karunya University, Coimbatore 641114, India

C. N. Kumar
Department of Physics, Panjab University, Chandigarh 160014, India

Prasanta K. Panigrahi
Indian Institute of Science Education and Research-Kolkata, Mohanpur, Nadia 741252, India

We explore the exact optical similaritons of a generalized nonlinear Schrödinger equation(GNLSE) with space-time modulated dispersion, nonlinearity, external potential and inhomogeneous source. We show that this equation is appropriate for the description of wave propagation through asymmetric twin-core fiber, in which we control the dynamics of the pulse propagating through passive fiber by controlling the dynamics of the self-similar wave propagating through the active fiber. By utilizing multivariate similarity transformation, we map the non-autonomous GNLSE to autonomous NLSE with a homogeneous external source. Furthermore, by using Möbius transformation, we find periodic waves, solitary waves and pure cnoidal and pure snoidal solutions as exact solutions. As an application, we study the dynamics of these similaritons for a spatial Bessel modulated nonlinearity.

I. INTRODUCTION

By now, it has been well established that the nonlinear Schrödinger equation (NLSE) and its variants describe wave propagation through nonlinear optical fibers. Solitons which emerge as the solutions of NLSE, due to a delicate balance between nonlinearity and dispersion or diffraction, are considered to be the natural carriers of high-bit-rate information via long-haul telecommunication networks. Recently, there is a tremendous interest in obtaining self-similar waves or similaritons for NLSE with distributive parameters [1–3]. Self-similar waves are similar to solitons with an added advantage of their modulating behaviors both in the width and amplitude as a function of the length of the fibers. More recently, there is a resurgence of interest in obtaining space-time modulated self-similar waves that propagate self-similarly subject to simple scaling rules in a nonlinear fiber [4, 5].

All the aforementioned works are restricted to the study of self-similar propagation through single-core fibers. Although, it is easier to fabricate twin-core fibers (TCF) with some built-in asymmetry, the nonlinear pulse propagation in these types of couplers has not received much attention in the literature.

To name a few, solitary waves in TCF [6] and compression of self-similar waves in asymmetric TCF were investigated [7, 8]. For our problem, we consider the propagation of waves in an asymmetric twin core fiber. The model equation is NLSE with space-time modulated dispersion, nonlinearity, external potential, and an external source. Utilizing a multivariate similarity transformation, we map the nonautonomous dynamical system to an autonomous one. Then by using one more transformation, we obtain an elliptic equation. With the aid of Möbius transformation, we find periodic, solitary wave, and pure cnoidal solutions as exact solutions. Toward the end we study the dynamics of these self-similar waves for a spatially Bessel modulated nonlinearity.

II. SIMILARITON WAVE PACKETS IN ASYMMETRIC TWIN-CORE FIBERS

The generalized nonlinear Schrödinger equation with space-time modulated parameters may be written as:

$$i\frac{\partial}{\partial z}\psi + \frac{1}{2}\beta(z,x)\frac{\partial^2}{\partial x^2}\psi + \gamma(z,x)|\psi|^2\psi + R(z,x)\psi + \eta(z,x)e^{i\Phi+iB(z,x)} = 0. \tag{1}$$

Here, $\beta(z,x)$ corresponds to the diffraction coefficient, $\gamma(z,x)$ the nonlinearity coefficient, $R(z,x)$ is the external potential, $\psi(z,x)$ corresponds to the complex envelope of the electric field, and $\eta(z,x)$ is the inhomogeneous source.

* Electronic address: soloman@karunya.edu
† Presenting Author

In order to obtain the exact analytical solutions of Eq. (1), use shall be made of the following multivariate similarity transformation [1, 5]

$$\psi(z,x) = A(z,x)Q(z,X(z,x))e^{i[\Phi+B(z,x)]}, \tag{2}$$

where the multivariate self-similar variable $X(z,x)$, the amplitude AQ, and the combined phase $\Phi + B$ are all functions of z and x. Writing the amplitude of ψ as a product of two auxiliary functions allows for more freedom in the treatment of Eq. (1). The ultimate aim is to transform nonautonomous Eq. (1) into the standard NLS equation with constant coefficients. Substituting Eq. (4) into Eq. (1), we may extract the following equation which is the NLSE with a homogeneous external source:

$$i\frac{\partial}{\partial z}Q + \frac{1}{2}\frac{\partial^2}{\partial X^2}Q + \sigma|Q|^2Q + Ke^{i(X-vz)} = 0, \tag{3}$$

requiring that the following relations are satisfied:

$$\beta(z,x)X_x^2 = 1, \tag{4}$$

$$\chi(z,x)A^2 = \sigma, \tag{5}$$

and

$$\eta(z,x) = KA(z,x). \tag{6}$$

Equation (8) indicates that the space-time modulated external source is proportional to the amplitude of the self-similar wave. Figure 1 depicts this source for (a) Bessel nonlinearity for $n = 1, 2, 3$ and (b) Airy modulated nonlinearity. Now we separately assemble terms containing Q and Q_X from the remaining terms of the equation. Equating the coefficients of Q and Q_X to zero, we get following system of equations

$$\frac{\partial}{\partial x}\left(A^2\frac{\partial X}{\partial x}\right) = 0, \tag{7}$$

$$-\frac{\partial B}{\partial z} + \frac{\beta}{2A}\frac{\partial^2 A}{\partial x^2} - \frac{\beta}{2}\left(\frac{\partial B}{\partial x}\right)^2 + R = 0, \tag{8}$$

$$\frac{\partial B}{\partial x} = -\frac{1}{\beta}\frac{X_z}{X_x}, \tag{9}$$

$$\frac{\partial}{\partial z}A^2 + \beta\frac{\partial}{\partial x}\left(A^2\frac{\partial B}{\partial x}\right) = 0, \tag{10}$$

From Eq. (7) we find

$$A^2 = \frac{\lambda^2(z)}{X_x}, \tag{11}$$

where $\lambda(z)$ is an integration constant. Substituting Eq. (11) into Eq. (10) and also using Eq. (9) we obtain

$$\frac{\lambda_z}{\lambda} - \frac{X_xX_{xz}}{X_x^2} + \frac{\beta_x}{2\beta}\frac{X_z}{X_x} + \frac{X_zX_{xx}}{X_x^2} = 0. \tag{12}$$

Eq. (4) leads to

$$\frac{\beta_x}{2\beta} = -\frac{X_{xx}}{X_x}. \tag{13}$$

Substituting Eq. (13) into Eq. (12) we get

$$X(z,x) = \lambda(z)F(x) + \theta(z), \tag{14}$$

where $\theta(z)$ is an integration constant.
For $\sigma = 1$ one obtains from Eqs. (4), (5), (11) & (14)

$$F_x = \lambda\chi \tag{15}$$

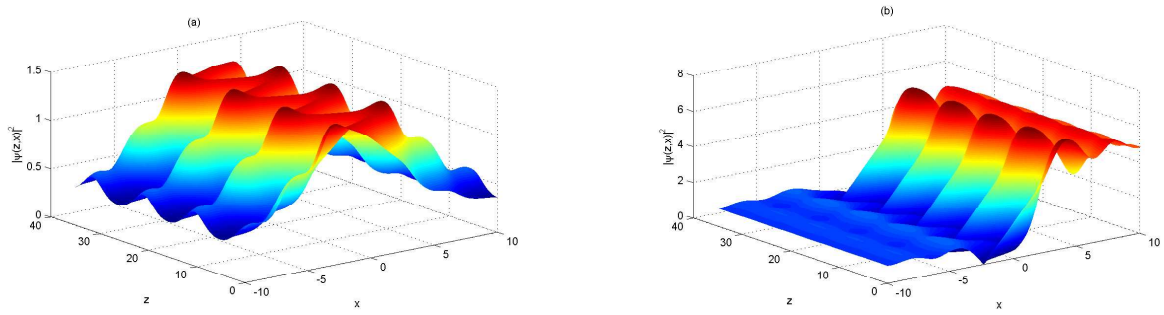

FIG. 1: Plot depicting the evolution of (a) bright similariton and (b) kink-similariton for Bessel modulated nonlinearity.

and

$$\beta(z,x) = \frac{1}{\lambda^4 \chi^2}. \tag{16}$$

Using Eq. (9) and Eq. (14) we may express phase $B(z,x)$ as

$$B(z,x) = -\frac{1}{2}\lambda\lambda_z F^2 - \lambda\theta_z F + \varphi(z). \tag{17}$$

where $\varphi(z)$ is an integration constant. Substituting Eqs. (4), (11), (14) and (17) in Eq. (8), we may express external potential $R(z,x)$ as

$$R(z,x) = -\frac{1}{2}\lambda\lambda_{zz}F^2 - \frac{3F_{xx}^2 - 2F_xF_{xxx}}{8\lambda^2 F_x^4} + \varphi_z + \frac{\theta_z^2}{2} - \lambda\theta_{zz}F. \tag{18}$$

Using one more transformation:

$$Q = f(\xi)e^{i\xi}, \tag{19}$$

we reduce Eq. (3) to an elliptic equation:

$$f'' + af + bf^3 + K = 0. \tag{20}$$

III. MÖBIUS TRANSFORM WAVE PACKET SIMILARITONS

We use Möbius transform to solve Eq (5). Hence, we consider an expression for $f(\xi)$ of the form :

$$f = \frac{A + Bg}{1 + Dg}, \tag{21}$$

where, $g(m,\xi)$ is a Jacobian elliptic function. For the sake of illustration, we have taken $g(m,\xi) = \mathrm{cn}$ and $g(m,\xi) = \mathrm{sn}$. For the Jacobian elliptic modulus tends to one, we obtain a bright-similariton and a kink-similariton. In order to showcase their dynamical behaviors, we have chosen the spatially modulated Bessel nonlinearity: $\gamma(x) = b_0 + J_n^2(x)$ where, $J_n(x)$ is the Bessel function of order n. Figure 1, (a) depicts the breather sech-similariton and (b) breather kink-similariton for $n = 3$.

IV. CONCLUSION

Utilizing multivariate similarity transformation, we have mapped a nonautonomous GNLSE to normal NLSE with a homogeneous source. With the aid of a Möbius transformation we found exact periodic, soliton, and pure Jacoian elliptic solutions. Under certain physical conditions, we have reduced the coupled NLSEs to a single-wave equation that aptly describes similariton propagation through asymmetric twin-core fiber amplifiers. As an application, we have studied the dynamical behaviors of the sech-similariton and kink-similariton for a Bessel modulated nonlinearity. Although, not presented here, we have checked the numerical stability of these similaritons, using a semi-implicit Crank-Nicolson finite difference algorithm, and found that these wave packets are quite stable against finite perturbations.

Acknowledgement

T.S.R. would like to thank DST, Government of India, for financial support through Fast Track Project (Young Scientist Award), during the course of this work.

---

[1] V. N. Serkin and A. Hasegawa, Phys. Rev. Lett. **85**, 4502 (2000).
[2] V.I. Kruglov, A.C. Peacock, and J.D. Harvey, Phys. Rev. Lett. **90**, 113902 (2003).
[3] L. Wu, J. F. Zhang, L. Li, Q. Tian, and K. Porsezian, Opt. Express **16**, 6352 (2008).
[4] J. Belmonte-Beitia, V. M. Pérez-García, V. Vekslerchik, and V. V. Konotop, Phys. Rev. Lett. **100** 164102 (2008).
[5] Wei-Ping Zhong, Milivoj R. Belić, and Tingwen Huang, J.Opt. Soc Am. B **30**, 1276 (2013).
[6] B. A. Malomed, I. M. Skinner, P. L. Chu, and G. D. Peng, Phys. Rev. E **53**, 4084 (1996).
[7] T. Soloman Raju, P. K. Panigrahi, and K. Porsezian, Phys. Rev. E **72**, 046612 (2005).
[8] T. Soloman Raju and P. K. Panigrahi, Phys. Rev. A **84**, 033807 (2011).

Chirped dissipative double-kink and fractional-transform quadratic solitons induced by localized nonlinear gain

Thokala Soloman Raju * and Tejaswi Hegde †
Department of Physics, Karunya University, Coimbatore 641114, India

C. N. Kumar
Department of Physics, Panjab University, Chandigarh 160014, India

Prasanta K. Panigrahi
Indian Institute of Science Education and Research-Kolkata, Mohanpur, Nadia 741252, India

We propose a model for the formation of stable chirped dissipative double-kink and fractional-transform quadratic solitons induced by localized nonlinear gain, in optical media with χ^2 (quadratic) nonlinearity. We further demonstrate that by modulating the properties of the gain medium, one can control the width of these localized waves. It is observed that the nonlinear chirp associated with each of these waves is directly proportional to the intensity of the wave.

I. INTRODUCTION

Much attention has been paid to the study of dissipative spatial solitons in different media, including lasers with saturable gain and absorption, systems where light evolution is governed by the cubic-quintic complex Ginzburg-Landau equation, and in semiconductor amplifiers. It is interesting to note that the localized waves such as solitary waves do not only exist in conservative systems, but also in dissipative systems, where the self-localization is supported by the delicate balance between the diffraction and self-focusing, as in lossless media, and between loss and gain. Recently, dissipative χ^2 solitons were studied in models of spatially uniform cavities and $\mathcal{PT}$-symmetric systems. Nevertheless, the study of formation of double-kink and fractional-transform dissipative solitons induced by a transversally modulated nonlinear gain has not been explored yet.

It is well known that nonlinear pulse propagation in optical medium is governed by nonlinear Schrödinger equation (NLSE) which is completely integrable and allows for either bright or dark optical solitons depending on the signs of dispersion or nonlinearity. These conventional solitons are chirp free pulses because the chirp produced by group velocity dispersion is balanced by the chirp produced by the Kerr nonlinearity. Serkin and his collaborators are the pioneers in demonstrating the existence of chirped solitons in a nonlinear dynamical system such as NLSE with gain/loss, higher order and variable coefficient terms[1–5]. The chirp of an optical pulse is usually understood as the time dependence of its instantaneous frequency. The chirped solitons have been utilized to achieve efficient chirp and pedestal free pulse compression [6]. Hence, chirped pulses are useful in the design of optical devices such as fibre optic amplifier, optical pulse compressors and solitary wave based communication links [3, 7]. In many optical applications, it is desirable to reduce the pulse power required to form a soliton, particularly for switching applications. The switching devices are very useful in connecting input and output ports. In order to reduce the required power and the switching threshold, one can use materials with high nonlinear index coefficients than that of silica. The objective of the present work is to extend the analysis of dissipative solitons in χ^2 nonlinearity induced by a transversally modulated nonlinear gain.

II. OUR MODEL

Below, we introduce our model with the "hot spot" acting on the fundamental frequency (FF). This scenario is captured with the help of coupled dimensionless equations for local amplitudes of FF (u_1) and second harmonic (SH)(u_2) in the spatial domain, under conditions for the degenerate χ^2 interaction in the presence of dissipation and localized nonlinear gain:

$$i\frac{\partial u_1}{\partial \xi} = -\frac{1}{2}\frac{\partial^2 u_1}{\partial \eta^2} - u_1^* u_2 \exp(-i\beta\xi) + i g_1(\eta) u_1$$
$$i\frac{\partial u_2}{\partial \xi} = -\frac{1}{2}\frac{\partial^2 u_2}{\partial \eta^2} - u_1^2 \exp(i\beta\xi) - i g_2 u_2, \quad (1)$$

* Electronic address: soloman@karunya.edu
† Presenting Author

where η and ξ are transverse coordinate and propagation distance, β corresponds to wave-number mismatch, and $g_1(\eta)$ corresponds to transversally modulated gain and g_2 signifies homogeneous loss, respectively.

We take note that in the cascading limit, which, in the present case, corresponds to large values of β and γ_2, the SH field can be eliminated:

$$u_2 \approx (\beta - ig_2)^{-1}\exp(i\beta\xi)u_1^2, \tag{2}$$

and the remaining equation for the FF fied to

$$iu_z = -\frac{1}{2}u_{tt} - \Gamma_1|u|^2u - i\Gamma_2|u|^2u + ig(t)u, \tag{3}$$

reduces to the "hot spot" model. Here $\Gamma_1 = \frac{\beta}{\beta^2+g_2^2}$ and $\Gamma_2 = \frac{g_2}{\beta^2+g_2^2}$.

III. CHIRPED SOLITON-LIKE SOLUTIONS

To start with, we have chosen the following form for complex field

$$u(z,t) = \rho(t)\, e^{i(\phi(t)+\gamma z)}, \tag{4}$$

where ρ and ϕ are the real functions of t and γ is the propagation constant. The corresponding chirp is given by $\delta\omega(t) = -\frac{\partial}{\partial t}[(\phi(t)+\gamma z] = -\phi_t(t)$. Substituting Eq. (4) in Eq. (3) and separating out the real and imaginary parts of the equation, we arrive at the following coupled equations in ρ and ϕ,

$$\rho_{tt} - 2\gamma\rho - \phi_t^2\rho + 2\Gamma_1\rho^3 = 0 \tag{5}$$

and

$$2\phi_t\rho_t + \phi_{tt}\rho + 2\Gamma_2\rho^3 - 2g(t)\rho = 0. \tag{6}$$

To solve these coupled equations, one can choose the ansatz

$$\phi_t = c_1 + c_2\rho^2. \tag{7}$$

Hence, chirping is given as $\delta\omega(t) = -(c_1 + c_2\rho^2)$, where c_1 and c_2 denote the constant and nonlinear chirp parameters, respectively. It means chirping of wave is directly proportional to the intensity of wave. Using ansatz Eq. (7), Eqs. (5) and (6) reduces to

$$\rho_{tt} = (2\gamma + c_1^2)\rho + (2c_1c_2 - 2\Gamma_1)\rho^3 + c_2^2\rho^5, \tag{8}$$

$$g(t) = c_1\frac{\rho_t}{\rho} + 2c_2\ \rho\rho_t + \Gamma_2\rho^2. \tag{9}$$

The elliptic equation given by Eq. (8) can be mapped to ϕ^6 field equation to obtain a variety of solutions such as periodic, kink and solitary wave type solutions [8]. In general, all traveling wave solutions of Eq. (8) can be expressed in a generic form by means of the Weierstrass $\wp$ function. In this work, we report only those soliton-like solutions for which gain profile, given by Eq. (9), remains localized. For $c_2 = 0$, Eq. (8) reduces to well known cubic elliptic equation for which non-chirped soliton solutions can be easily found. Here, we studied Eq. (8) for different parameter conditions and obtained chirped soliton solutions. The reported solutions consist various soliton solutions like double-kink, fractional-transform, bell and kink-type solitons. For double-kink and bell-type solitons, we consider the case $c_1 = 0$ because for non-zero values of c_1 the corresponding gain will no longer be localized.

A. Double-kink solitons

Eq. (8) admits double-kink solutions of the form

$$\rho(t) = \frac{m\sinh(nt)}{\sqrt{\epsilon + \sinh^2(nt)}}, \tag{10}$$

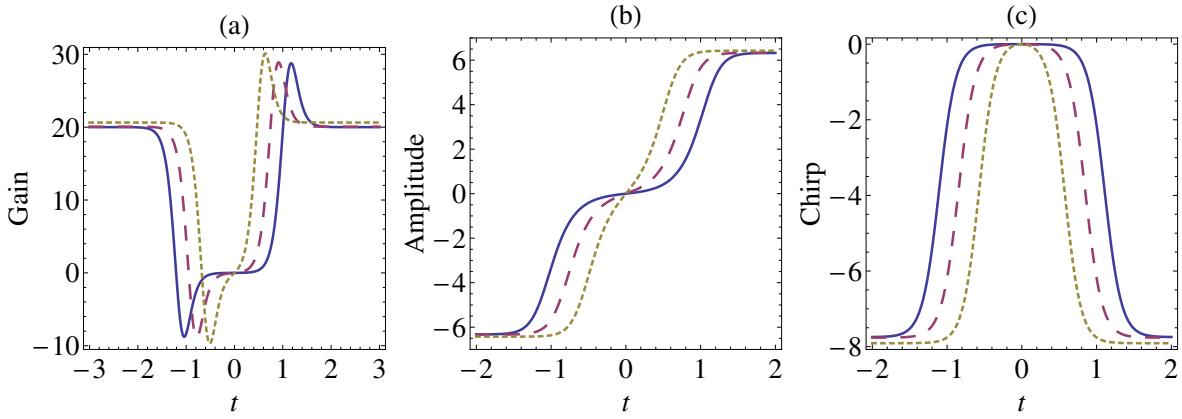

FIG. 1: (a) Gain, (b) amplitude, and (c) chirp profiles for double-kink solitons for different values of ϵ, $\epsilon = 5000$ (thick line), $\epsilon = 500$ (dashed line) and $\epsilon = 50$ (dotted line). The other parameters used in the plots are $\Gamma_1 = 1, \gamma = 10$ and $\Gamma_2 = 0.5$.

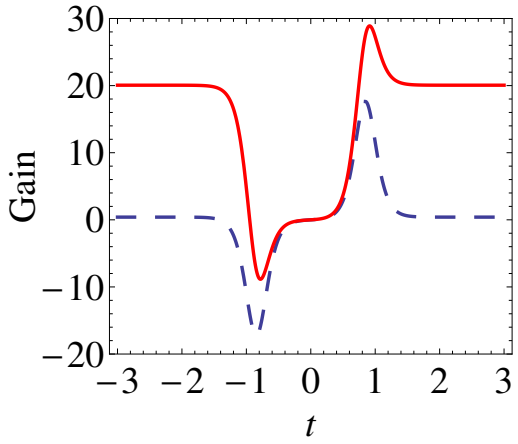

FIG. 2: Gain profile for double-kink solitons for $\Gamma_2 = 0.5$ (thick line) and $\Gamma_2 = 0.01$ (dashed line). The parameters used in the plots are $\epsilon = 500,\ \Gamma_1 = 1$ and $\gamma = 10$.

where $m = \sqrt{\frac{2\gamma(2\epsilon-3)}{\sigma(\epsilon-3)}}$, $n = \sqrt{\frac{2\gamma\epsilon}{\epsilon-3}}$, $c_2 = \frac{\sqrt{2(m^2\Gamma_1-\gamma)}}{m^2}$ and $c_1 = 0$. The choice $c_1 = 0$ has been made in order to avoid the singularities in gain profile. Here, ϵ is a free parameter which controls the width of soliton solutions. The interesting double-kink feature of the solution is prominent for large values of ϵ. Now, for $m,\ n$ and c_2 to be real numbers, ϵ should be always greater than 1 and never be equal to $3/2$ and 3. Depending upon the model parameter, solutions are possible for some constraint conditions on ϵ and γ :

- for $\Gamma_1 = -1$, ϵ should lie between $1 < \epsilon < 3/2$ with negative values of γ.
- for $\Gamma_1 = +1$, ϵ can take any value either in the region $3/2 < \epsilon < 3$ with negative γ or $\epsilon > 3$ with positive value of γ.

For solution given in Eq. (10), the gain will be of the following form

$$g(t) = \frac{m^2\left(\Gamma_2 \sinh^2(nt)\left(\epsilon + \sinh^2(nt)\right) + c_2 n\epsilon \sinh(2nt)\right)}{\left(\epsilon + \sinh(nt)^2\right)^2}, \tag{11}$$

and the chirping will be

$$\delta\omega(t) = -\frac{c_2\, m^2 \sinh^2(nt)}{\epsilon + \sinh^2(nt)}. \tag{12}$$

The variation of gain, amplitude and chirp for different values of ϵ is shown in Fig. 1. The parameters used in the plots are $\Gamma_1 = 1,\ \gamma = 10$ and $\Gamma_2 = 0.5$. One can point out that as the value of ϵ changes, there is a small change in the gain profile which

in turn have significant effect on the amplitude and chirp of double-kink solution. Hence, one can observe that the double-kink feature of the wave is more prominent for a gain medium with large values of ϵ, and different gain medium effects only the width of the double-kink wave whereas the amplitude of the wave always remains same. From the plot of chirp, it is clear that it has a maximum at the center of the wave and saturates at the some finite value with time.

From the expressions of amplitude, gain and chirp(Eqs. (10)-(12), it is clear that the dissipation coefficient Γ_2 has no effect on amplitude and chirp of wave, whereas it has significant effect on the gain expression. Hence, for different values of Γ_2, only the gain profile is modified which results a localized solution. In Fig. 2, the gain profile is shown for different values of Γ_2, $\Gamma_2 = 0.5$ and $\Gamma_2 = 0.01$. The other parameters used in the plots are $\epsilon = 500,\ \Gamma_1 = 1$ and $\gamma = 10$. From the plots, it is clear that the gain profile is transversally localized and has more amplitude for large values of Γ_1.

IV. CONCLUSION

It is demonstrated that nonlinear losses due to dissipation are exactly balanced by localized gain and induces the optical solitons in nonlinear medium. We report the existence of chirped double-kink [8], fractional-transform [9], bell and kink-type soliton solutions. The parameter domain is delineated in which these optical solitons exist. The width of double-kink solitons can be controlled by modulating the gain profile. Interestingly, fractional-transform solutions support either bright or dark solitons depending on model parameters. Further, bell and kink-type solitons are found to exist in this system for different choice of parameters. The chirp related to solitons has also been identified and found that it is directly proportional to the intensity of wave. The amplitude of localized gain is directly proportional to the value of dissipation coefficient and saturates at some finite value as the retarded time approaches its asymptotic value.

ACKNOWLEDGEMENT

T.S.R. wishes to thank DST, Government of India, for financial support through Young Scientist Award, during the course of this work.

[1] Serkin, V.N.; Hasegawa, A.; Belyaeva, T.L. *Phys. Rev. Lett.* **2007**, 98, 074102.
[2] Serkin, V.N.; Hasegawa, A.; Belyaeva, T.L. *J. Mod. Opt.* **2010**, 57, 1456-1472.
[3] Kruglov, V.I.; Peacock, A.C.; Harvey, J.D. *Phys. Rev. Lett.* **2003**, 90, 113902.
[4] Wang, J.; Li, L.; Jia, S. *Opt. Commun.* **2007**, 274, 223-230.
[5] Goyal, A.; Gupta, R.; Kumar, C.N.; Raju, T.S.; Panigrahi, P.K. *Opt. Commun.* **2013**, 300, 236-243.
[6] Senthilnathan, K.; Nakkeeran, K.; Li, Q.; Wai, P.K.A. *Opt. Commun.* **2012**, 285, 1449-1455.
[7] Desaix, M.; Helezynski, L.; Anderson, D.; Lisak, M. *Phys. Rev. E* **2002**, 65, 056602.
[8] Alka; Goyal, A.; Gupta, R.; Kumar, C.N.; Raju, T.S. *Phys. Rev. A* **2011**, 84, 063830.
[9] Vyas, V.M.; Raju, T.S.; Kumar, C.N.; Panigrahi, P.K. *J. Phys. A: Math. Gen.* **2006**, 39, 9151-9159.

A self-referencing surface plasmon resonance sensor

Shankar Pidishety
Department of Electrical Engineering, Indian Institute of technology, Madras,
Chennai, India, 600036

ABSTRACT

A zero cross sensitivity (CS) deliverable self-referencing surface plasmon resonance sensor (SPR) scheme is explored based on the retroreflecting prism configuration with single spectroscopic read out. The relationship between external and internal incident angles in retroreflection configuration results in the excitation of two spectroscopically distinct surface plasmons (SPs) modes corresponding to each side of the prism. The characteristics of two SPs modes are independent and thus used in differential refractive index (RI) sensing via self-referencing (SR) modes technique. By applying SR sensing theory, it is shown that the CS can be minimized to zero through the demonstrated configuration. This configuration is flexible for using in wavelength interrogation measurement method as well. The excited SPs modes are also tunable to acquire either identical or non-identical sensitivity by selecting corresponding film thickness. From the preliminary experimentation on SR configuration and theoretical investigation on deliverability of zero CS, it can be expected that the presented scheme is a better SR configuration for high accurate differential RI sensing applications.

Keywords: Self-reference sensor, surface plasmon resonance, cross sensitivity, plasmonics

1. INTRODUCTION

The surface plasmon resonance mode excited at the metal-air interface is highly sensitive to proximal RI changes [1, 2]. Thus it has been extensively used in different sensor systems for a wide range of sensing applications including for bio-molecular interactions, chemicals detection, food quality test and environmental monitoring [2, 3]. Most of the SPR sensors are based on single resonance mode and are incapable of distinguishing between the signal response to specific change and non-specific change, generally encountered in sensing bio-molecular interactions and complex analyte detection [4]. Specific response is due to surface RI change resulting from the binding of analyte molecule with recognition surface layer, while the unwanted non-specific response is due to bulk RI change induced by temperature fluctuations, interaction of non-target molecules and concentration variations in the complex analyte [5, 6]. This leads to an increase in unwanted CS, i.e., sensitivity of the sensing system for specific response and non-specific responses [6]. Hence, the CS must be suppressed for an efficient differential sensing system.

To differentiate between the bulk and surface RI changes and minimize the cross sensitivity a novel class of self-referencing SPR sensors have been developed based on the excitation of more than one SPR mode in the same system, wherein one of the modes can be used for specific detection, while the other mode for non-specific detection [5]. Realizing a dual mode excitation system, with a single read out has been a challenging task [5]. The multi-layer structure which supports two resonance modes of unlike penetration depths either at two different wavelengths or at two different incident angles is the most common experimental technique to achieve such a configuration [7]. The concept behind using two or more SPs modes for differential sensing is to limit the sensing depth or the range of a particular excited mode in probing the particular RI change of the sensing medium [8]. A specific sensing range for the excited mode can be achieved by tuning its penetration depth of excited SPs mode. Thus if the sensing system is accomplished by the excitation of two SP modes of different penetration depths, the mode of smaller penetration depth limits its sensing range to probe the surface RI changes on the recognition layer while the other mode probes the bulk RI changes due its longer sensing range or the penetration depth [8]. For example, as the long-range (LR) and short-range (SR) SP modes are characterized by different penetration depth and thus sensitivity, the simultaneous excitation of these modes is used for differential sensing by isolating their sensitivities to probe the specific RI changes in the analyte [6]. Such sensitivity isolation of the two or more simultaneously excited SPs modes in a single sensing system can significantly minimize the cross sensitivity and thereby enhance the differential sensing efficiency [8].

Thus, various configurations have been developed based on long-range and short-range surface plasmon (LR-SR-SP) modes, multi-step self-assembly, planar waveguide structures, wavelength division multiplexing and localized SP in nano rods [6, 9, references therein]. As controlling the penetration depth of different plasmon modes excited in the same system at different wavelengths is a critical issue in wavelength interrogation (WI) method, an alternative angular interrogation (AI) technique has also been reported [9, 10]. In this context, an angular interrogation based simple self-referencing SPR sensor is configured and demonstrated using a right angle prism in retroreflection scheme here.

2. EXPERIMENTAL DETAILS

The two sides (1, 2) of the right angle BK7prism are coated with the gold film and is used as retroreflector to excite the two surface plasmon modes at two distinct internal angles as schematically shown in Fig.1-(a). The thickness of the metal films coated on the two sides 1 and 2 are measured using the profilometer (Ambios XP-1, USA) to be d1 = 50±2 and d2 = 45±2nm respectively. The TM-polarized optical beam from the He-Ne laser (Newport, USA, λ = 632.8 nm) is used to excite the plasmons at the metal-air interface on the two sides of the prism. The incident angle is changed using the computer-controlled rotation stage (Thorlabs, USA) and the intensity of the retroreflected light is measured using the power meter (Ophir, USA).

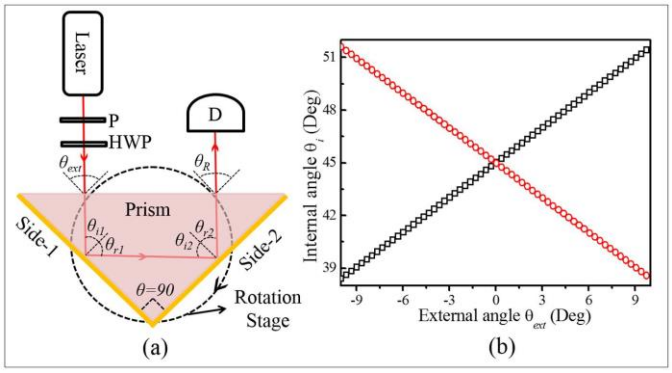

Figure 1. (a): Schematic of the experimental setup. P-Glan-Thompson polarizer, HWP-half-wave plate and D- detector, (b): Relationship between the external and internal angles.

2.1 Theory

The theoretical formalism for the retroreflection scheme can be understood based on Fresnel reflection coefficients of a three layer (prism (p)-metal (m)-air (a)) geometrical structure, similarly that of the Kretschmann-Raether geometry [1]. The resultant reflection coefficient for TM-polarized light at the two sides can be written as

$$R_{12} = \left| r^{p}_{(pma)1} \right|^2 * \left| r^{p}_{(pma)2} \right|^2 \tag{1}$$

Where, $r^{p}_{(pma)1}$ with i=1,2 for side-1 and side-2 of the prism, is the Fresnel reflection coefficient. The relationship between the external angle θ_{ext} and the internal angle at the 1 and 2 interfaces, respectively θ_{i1} and θ_{i2}, shown in Fig.1-(b), expressed as

$$\theta_{i1} = 45 \pm \sin^{-1}\left[\frac{\sin(\theta_{ext})}{\varepsilon_p}\right], \theta_{i2} = 45 \mp \sin^{-1}\left[\frac{\sin(\theta_{ext})}{\varepsilon_p}\right], \tag{2}$$

Where, $\varepsilon_p (= \varepsilon_{(p)1,2})$ is the dielectric constant of the prism and the sign "±" is decided by direction of change in the external angle with respect to the prism normal. In the retroreflection scheme, the incident light experiences two of three layered (p-m-a) interfaces on the side-1 and 2 of the prism at different angles leading to the excitation of two SP modes at the respective interfaces.

3. RESULTS AND DISCUSSION

It is clear from Eq. (2) that the internal angles θ_{i1} and θ_{i2} varies linearly as a function of external angle θ_{ext} as shown in Fig.1-(b). As the external angle changes with respect to normal to the prism base, one of the internal angle (θ_{i1}) increases, while the other (θ_{i2}) decreases linearly. Both the internal angles coincide at the angle θi1 = θi2 = 45^o for

normal incidence of external angle i.e., for θ_{ext} = 0. The TM-polarized He-Ne laser light reflects sequentially from the two sides of the Au coated prim as we increase the external angle (θ_{ext}). When one of the two internal angles equals the resonance angle ($k_x = k_{SPP}$ [1]), it excites SPs at one interface , while the other interface behaves as a good reflector due to the fact that its internal angle is away from resonance and beyond TIR angle.

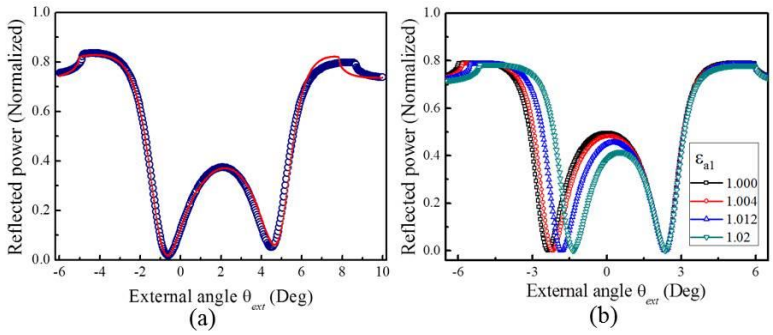

Figure 2. (a): Experimental measurement of the self-reference based characteristic SPR curve shows modes M1 and M2 (open circle) with theoretical fit (continuous line), (b): A theoretical result of mode M1 shift due to the RI change at side-1.

The experimentally measured SPR modes M1 and M2 corresponding to the metal-air interface of side-1 and 2, respectively, are fitted to the theoretical resonance curve (R_{12}-vs- θ_{ext}), is shown in Fig. 2-(a). The obtained real and imaginary parts of the dielectric constant and thickness of the Au film corresponding to sides-1 and 2, respectively are, "ε_{mr1} = -10.46±0.5, " ε_{mi1} = 1.58±0.02, d1 = 50±3nm and " ε_{mr2} = -12.36±0.6, " ε_{mr2} = 2.34±0.03, d2 = 45±3nm which are in agreement with literature values [1]. As the film thickness d1 and d2 coated on the two sides of the prism are not equal, the two SP modes excited at side-1 and side-2 exhibit unequal amplitudes and have asymmetric angular distribution with reference to θ_{ext} = 0 as shown in Fig. 2-(a). This results in the excitation of SP modes with different penetration depths and hence different sensitivities. From the result shown in Fig. 2-(b) it is clear that the excited SP mode M1 of one side does not influence the mode M2 on the other side, thus any combination of either similar or dissimilar modes can be excited by optimizing the coated metal film thickness [8]. Another experimental advantage of the present geometry is that the detector can be held stationary, as the incident beam retroreflects to the same position on the detector but in a direction opposite to the incident light (see in Fig. 1-(a)). This helps in effectively minimizing the mechanical noise.

The investigation on possibility of reaching to the reach zero CS in proposed retroreflection scheme is limited to only theoretical studies and is presented here. A simple study shown in Fig. 2-(b), where the two similar SPs modes M1 and M2 are excited by optimizing the film thickness d1 and d2 and changed the RI of ambient medium near mode M1. It is clear that only the resonance angle of modes M1 shifts while M2 remains. The theory presented in ref. [38] is applied to the configuration of two similar modes, and realized the deliverability of zero CS in the retroreflected scheme. Consider a configuration that consist a binding or recognition layer is coated on the sensing region of side-2, while side-1 coated with non-bonding layer to ensure M1 responds to only bulk refractive index change of the analyte. Hence, mode M2 shifts for both surface (Δd, here "d" is surface layer thickness) and bulk RI (Δn_B) change of analyte, while M1 shifts for only bulk RI (Δn_B) change of the same analyte. As the sensitivity of the modes M1 and M2 are equal, resultant angular shifts can be compared. Let the sensitivity of the M1 mode for bulk index change (Δn_B) is $S_{B\text{-}M1}$ and for surface RI change is $S_{S\text{-}M1}$ (= 0), while the sensitivity of the M2 mode for the bulk (Δn_B) and surface RI change (Δd) are $S_{B\text{-}M2}$ and $S_{S\text{-}M2}$, respectively. As the two modes respond to index change on the respective sides, linearly, the shifts θ_{iM1} and θ_{iM2} can be calculated as

$$\theta_{iM1} = S_{B-M1}\Delta n_B, \theta_{iM2} = S_{B-M2}\Delta n_B + S_{S-M2}\Delta d \quad (3)$$

Also, Δd and (ΔnB) are calculated from the resultant (difference between angular shifts) angle shift $\Delta\theta_{i(|M1\text{-}M1|)}$, and the CS ($\psi$=1/$\chi$) can be calculated as

$$\Delta d = \Delta\theta_{i(|M1-M2|)} / S_{S-M2}, \Delta n_B = \Delta\theta_{iM2} - \Delta\theta_{i(|M1-M2|)} / S_{B-M2} \quad (4)$$

$$\chi = \left| \frac{S_{S-M2}}{0} - \frac{S_{B-M2}}{S_{B-M1}} \right| \tag{5}$$

From Eq. (5), the parameter χ value can go to infinity. This means that the CS (ψ) can reach to zero. From the above discussion it is shown that the two spatially separated similar SPs modes can be used for self-reference sensing application using the proposed configuration with deliverable zero CS.

4. CONCLUSION

The TM-polarized incident light beam retroreflected from the two sides through the base of the prism and excite SPs at the metal-air interface on the two sides of the prism, in a modified Kretschmann-Raether geometry. Such a SPR sensor configuration is better suited for self-referencing high throughput sensing applications. By applying SR sensing theory, it is realized that the CS can be minimized to zero through the retroreflection configuration. The possibility of measuring the two SPs modes by single spectroscopic read-out can significantly reduce the spurious error due to the intensity fluctuations as compared to the two beam based SR sensing system. Unlike the KR geometry, the detector is held stationary in this configuration. This helps in effectively minimizing the mechanical noise. It is also possible to increase the number of modes by two times (6modes) as compared to that of maximum limit (3modes) of the current techniques by using multilayered structure. This configuration is flexible for using in wavelength interrogation measurement method as well. Hence, the presented scheme is expected to be a better SR configuration for high accurate differential RI sensing applications.

5. ACKNOWLEDGEMENT

Author acknowledges Prof. Nirmal K. V, University of Hyderabad's help in facilitating laboratory to carry out the preliminary experiments.

EFERENCES

[1] H. Raether, Surface Plasmons on Smooth and Rough Surfaces sand on Gratings (Springer Verlag, 1986).
[2] J. Homola, S. S. Yee, and G. Gauglitz, "Surface plasmon resonance sensors: review," Sensors and Actuators B: Chemical 54, 3-15 (1999).
[3] J. Homola, "Surface plasmon resonance sensors for detection of chemical and biological species" Chem. Rev.108, 462-493 (2008).
[4] J. Homola, H. B. Lu, G. G. Nenninger, J. Dostlek, and S. S. Yee, "A novel multichannel surface plasmon resonance biosensor," Sensors and Actuators B: Chemical. 76, 403-410 (2001).
[5] J. Homola, "Present and future of surface plasmon resonance biosensors," Anal. Bioanal. Chem. 377, 528-539 (2003).
[6] R. Slavik, J. Homola, and H. Vaisocherova, "Advanced biosensing using simultaneous excitation of short and long range surface plasmons," Measurement Science and Technology. 17, 932-938 (2006).
[7] F. Abeles and T. Lopez-Rios, "Decoupled optical excitation of surface plasmons at the two surfaces of a thin film," Opt. Commun. 11, 89-92 (1974).
[8] J. Guo, "Multi-mode self-referencing surface plasmon resonance sensors," Thesis Diss.{Electr. Comput. Eng. (2013).
[9] J. Guo, P. D. Keathley, and J. T. Hastings, "Dual-mode surface-plasmonresonance sensors using angular interrogation," Opt. Lett. 33, 512514 (2008).
[10] Y. Wan, Z. Zheng, Z. Lu, J. Liu, and J. Zhu, "Self-referenced sensing based on a waveguide-coupled surface plasmon resonance structure for background-free detection," Sensors and Actuators B: Chemical 162, 35-42 (2012).

Performance analysis of wavefront compensation at various light intensity and noise level condition in a closed loop laboratory adaptive optics system.

Satya Ranjan Behera[*a], B. Raghavendra Prasad[a]
[a]Indian Institute of Astrophysics, II Block, Koramangala, Bangalore 560 034, India

ABSTRACT

For implementation of Adaptive Optics technique a laboratory setup is needed to evaluate schemes and principles. Each component needs to be studied and evaluated experimentally in order to predict the performance of the Adaptive Optics system. The incoming wavefront is corrected from wavefront sensor by reconstruction algorithm and compensated by deformable mirror. In this paper the wavefront is compensated at various light intensity levels with noises like photon noise, background noise and readout noise. The input and output wavefront accuracy is measured with intensity and noise level.

Keywords : Shack Hartmann sensor, Centroiding algorithm, Deformable mirror, Control loop.

1. INTRODUCTIONS

In order to understand the performance of Adaptive Optics system a laboratory model has been proposed [1]. Components including Shack-Hartmann (SH) wavefront sensor, micromachine membrane deformable mirror (DM) have been studied experimentally. The collimated beam results in unshifted spots on the shack hartmann sensor. The first DM generates a deformation in the input wavefront and changes the spot pattern according to the voltage in each actuators. By the method center of gravity (CoG) local slopes are determined from the shifted spots [2].Applying the reconstruction algorithm to the wavefront slopes we can obtain the shapes of input wavefront. The accuracy of reconstructing the phase from slope measurements depends on the reconstruction algorithm alone [3]. whereas centroiding inaccuracies depend on various experimental conditions like incident light intensity, photon noise, readout noise, background noise, number of detector pixels per subaperture, size of the Shack-Hartmann spot and the shift in the Shack-Hartmann spot from the subaperture center . In order for output wavefront to be plane the shape of the reconstructed wavefront have to be inverted and the corresponding voltages given to the second DM. In this paper, we present an experimental comparison of output wavefront and input wavefront accuracy at various light intensity conditions [4]. A numerical evaluation of these algorithms suggests that their performance depends strongly on light intensity and noise conditions.

2. ADAPTIVE OPTICS FOR HIMALAY CHANDRA TELESCOPE

Atmospheric turbulence has imposed a serious constraint on the angular resolution of ground based astronomical telescopes. Without any form of compensation, atmospheric turbulence blurs the images and limits the angular resolution. The goal of an AO system is to correct aberrations in the incoming wavefront.

The Indian Astronomical Observatory (IAO), located near Leh in Ladakh, India, has one of the world's highest sites for optical, infrared. A 2-m aperture optical-infrared telescope, the Himalayan Chandra Telescope (HCT) is installed at IAO . The location of the 2-m HCT is at an altitude of 4500 meters above mean sea level. This is an ideal site for the astronomer to install telescope. The site has high number of spectroscopic and photometric nights approximately 250 and 180 respectively. The median seeing condition is < 1 arcsec. The median wind speed (υ) is 2.2m/s. The rms seeing condition (r_0) of IAO Hanle is 12.7cm at 500 nm [5]. In order to design AO system for IAO Hanle, Strehl ratio in infrared band 1.1μm is calculated theoretically. Its theoritical value is 0.5.

The first step in implementing AO technique in an application includes setup of a laboratory on an optical table aiming to evaluate schemes and principles. Before the components can be incorporated in a closed-loop setup each component needs to be study and evaluated experimentally in order to predict performance of the Adaptive Optics system. The optical lay out of this experiment is given below.

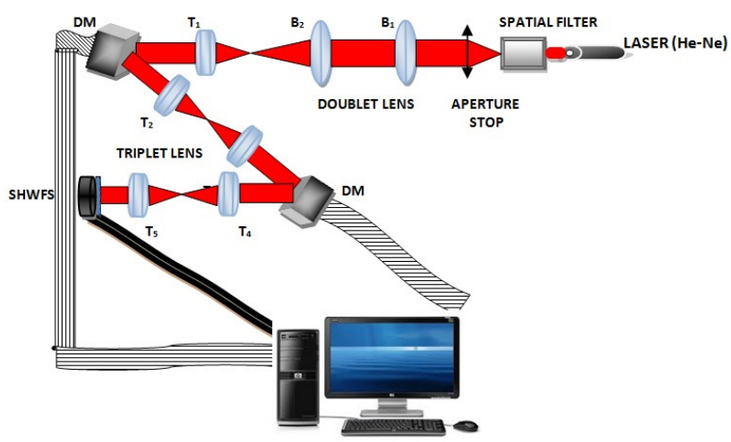

Figure 1 Schematic optical layout

*srbehera@iiap.res.in ;phone no - +91-9663923070

3. EXPERIMENTAL SETUP

A 15mW He-Ne laser (λ=632.8*nm*) was used as a source of light. Neutral Density Filter (NDF) was used to control the light intensity. Spatial Filter (SF) which removes the laser speckle noise was used for beam cleaning. $D_1$and D_2 are two collimating lenses of focal length f =25*cm* . T1 imaging lenses of focal length 12.5 cm is used to reduce the size of collimated beam. The beam falls on DM_1 which is a continuous MEMS deformable mirror (Multi-DM) from Boston Micromachines with 140 actuators and a maximum stroke of 5.5 μm having aperture area *s*=4.95*mm*. This DM_1 is acts as a turbulent wavefront generator. The reflected beam is allowed to pass T_2 and T_3 (focal length f= 12.5 *cm*) which are in fourier geometry. Fourier geometry removes the high frequency components. The collimated beam falls on another DM_2. This DM_2 is acts as a wavefront corrector. Finally the reflected beam from the DM_2 is fall on the Shack-Hartmann wavefront sensor passing the fourier lens T_4 and T_5 (focal length f= 12.5 *cm*). The DM_2 is placed on the image plane of DM_1. The SCMOS camera is also placed in image plane of the DM_2. The wavefront sensor has 100x100 sub apertures having equal diameter and pitch $p_\mu = 200\mu m$. The focal length of the wavefront sensor is f_μ =40 *mm*. The imaging camera is a high resolution low noise SCMOS camera from Photonic Science having sensor size 1920 x 1080. Each pixel is 6.5μm with readout noise as low as $1.2e^-$.

In order to sense the entire DM active area, the minimum number of subapertures to be used must be greater than the ratio, $\frac{s}{p_\mu}$ and hence 25 x 25 SHWS subapertures are used in this experiment. Each subaperture corresponds to $\frac{p_\mu}{p_{cmos}}$ = 31 pixels on the SCMOS. To avoid subaperture cross talk, the maximum voltage applied to the actuators of the DM was kept below 40 V. Below figure shows experimental setup

Figure 2 experimental setup for wavefront compensation

4. WAVEFRONT COMPENSATION PROCEDURE

The CCD frames are acquired as matrices using the Matlab image acquisition toolbox in real-time. In the absence of the microlens array and with zero voltages on all the DM actuators, a background image (BKD) is taken. Another reference pattern (REF) is taken by placing the mircolens array in front of the CMOS. A low-resolution higher order Zernike mode (Z_6^2) is addressed on the DM_1 actuators. The shifted spot pattern (SP) is then recorded. The maximum grayscale in theimage corresponds to 40V and minimum grayscale is 0V to avoid cross talk. Each of the matrices BKD, REF and SP are of size 775 x 775, since we are using a SHWS sensor with 25x25 subapertures and each subaperture corresponds to 31x31 pixels on the CMOS. BKD is subtracted from REF and SP. and simple CoG centroiding is performed on the resulting spot pattern images andthe local wavefront tilts are determined.

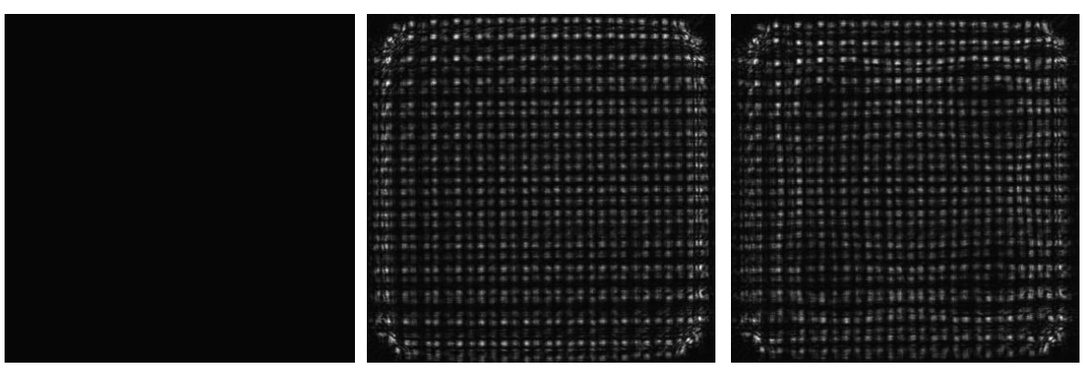

Figure 3 (a) BKD image ,(b)REF images and (c) SH spot pattern corresponding to Z_6^2

The steps followed for wavefront compensation are given below

4.1 Wavefront sensing :

The beam of light is sampled to many individual beams by the lenslets. It forms multiple spots in its focal plane. The local tilt of the wavefront across each lens can then be calculated from the position of the focal spot on the sensor [6].

$$\frac{\partial W(x,y)}{\partial x} = \frac{\Delta x}{F}, \frac{\partial W(x,y)}{\partial y} = \frac{\Delta y}{F}. \quad (1)$$

4.2 Simple Centre of Gravity

In the CoG technique, the centroid location of a single SHS subaperture spot, (xc, yc) for an intensity distribution $I(x, y)$ is evaluated, $(x_c, y_c) = \frac{\Sigma_{ij} x_{ij} I_{ij}}{\Sigma_{ij} I_{ij}}$ (2)

where, X is a vector containing '*x*' and '*y*' positional coordinates corresponding to intensity.

4.3 Sampling geometry :

Local gradients are measured at discrete locations of the wavefront. Depending on the position at which phase differences are estimated with reference to the location of slope measurements. In this experiment Fried'sgeometry has used [7].

$$S_{ij}^{x} = \frac{\left[\left(\frac{\emptyset_{i+1,j} + \emptyset_{i+1,j+1}}{2}\right) - \left(\frac{\emptyset_{i,j} + \emptyset_{i,j+1}}{2}\right)\right]}{h}$$

$$S_{ij}^{y} = \frac{\left[\left(\frac{\emptyset_{i,j+1} + \emptyset_{i+1,j+1}}{2}\right) - \left(\frac{\emptyset_{i,j} + \emptyset_{i+1,j}}{2}\right)\right]}{h}$$

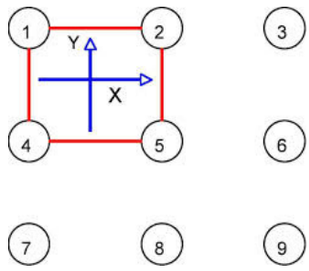

Figure 4 Fried geometry

4.4 Reconstruction algorithm.

The control algorithm is vital link between wavefront sensor and wavefront corrector in an adaptive optics. It converts wave aberration measurement made by wavefront sensor to a set of actuator commands that is applied to Deformable mirror. The algorithm has been created in MATLAB platform. The method used for reconstruction is zonal method. The phase is determined on a discrete set of points distributed over the telescope aperture. The slope vector *S* contains x- and y-slopes for all valid subapertures in the pupil. The phase vector contains all controllable actuators.

$$S = A * \emptyset \quad (3)$$

A is called interaction matrix . It is associated with each actuator when applying an unitary voltage to it and keeping all the others to zero.The wavefront Φ is estimated by the least square solution [8].

$$\emptyset = (A^T * A)^{-1} * A^T * S \quad (4)$$

4.5 Control system :

The reconstruction wavefront is 26 x 26 in phase. For getting a plane wavefront the second DM_2 has to be invert in such a way that the reflected beam from the second DM_2 is conjugate in phase from the first DM_1. The method used for wavefront correction is the actuators are activated from the phase map by wavefront reconstruction process. The measured slope vector [s] is given by Eq. (3). The deformed phase is corrected by the deformable mirror through a multiplication of the actuator influence function matrix [Zp] and the voltage vector [9].

$$\emptyset = z_P * v \quad (5)$$

From this equation we get the actuator voltage $v = [z_P^{-1}] * \emptyset$ (6)

For compensation a known zernike polynomial is given in DM_2. Also the reconstructed wavefront is resized to 12x12 and given for compensation in DM_2.

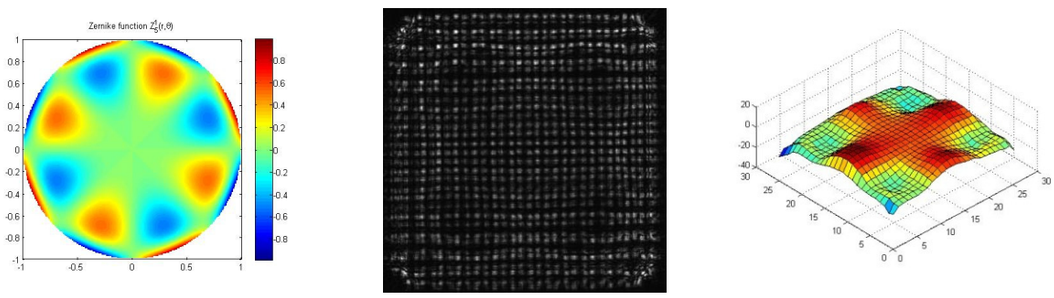

Figure 5 (a) Z(6,2) zernike input,(b) SH spot pattern, (c) reconstruction of wavefront which is 26x26 grid

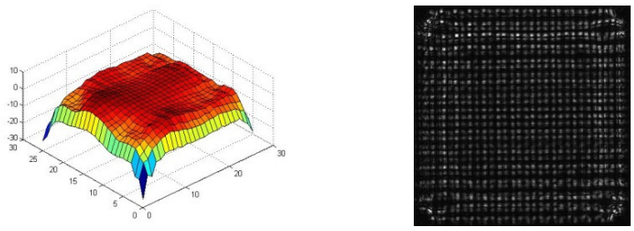

Figure 6 (a) wavefront shape after compensation (b) SH spots pattern after wavefront compensation

In this experiment wavefront compensation is carried with 24 zernike polynomials. In DM_1, the input wavefront created by the 24 zernike polynomials are given and the actuators changes their shapes according to voltages applied to them. The wavefront is reconstructed and resized to a 12x12 grid. The resulting wavefront is inverted and given as input to the DM_2. The final SH spots recorded. The correlation coefficient between input and output wavefront is found out. Correlation coefficient for unshifted SH spots and reconstructed SH spots after the wavefront compensation is also found out. It is found that both of these cases the correlation coefficient are in the order of 0.64.

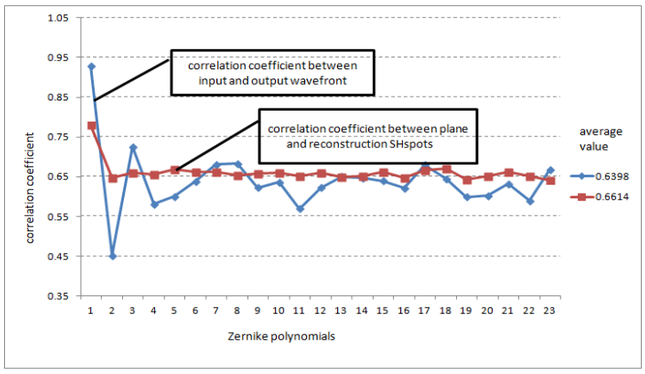

Figure 7 correlation coefficient for zernike polynomials

By changing the optical density of the neutral density (ND) filter, SH spots are obtained at different optical densities of the ND filter, till the SH spots are saturated. It has been seen that the wavefront compensation is consistent and the correlation coefficient remains constant between the optical densities of 1 to 3. The SH spots saturate below an optical density of 1 and the correlation coefficient falls to 0.4 at an optical density of 0.08. The presence of photon noise and background noise was not found to have significant contribution to the correlation coefficient.

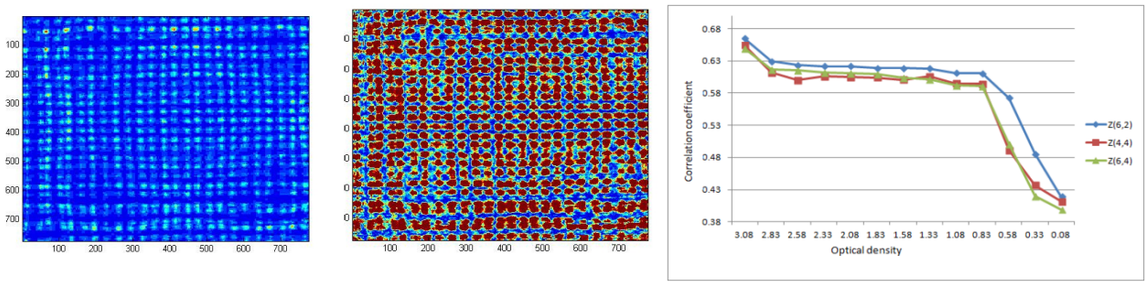

Figure 8 SH spots with the laser source transmitted through a ND filter of optical density of (a) 3 and (b) 0.08. (c) correlation coefficient for various light intensities with different zernike polynomials

5. CONCLUSION

There is good correlation between the input wavefront and the reconstructed wavefront when the optical density of the ND transmission filter was between 1 - 3. When the optical density is reduced below 1, the correlation coefficient falls rapidly.

.

REFERENCES

[1] S. H. ,. P. S. K. ,. BAIK, "Closed-Loop Adaptive Optics System for Wave-Front Correction," *Korea Atomic Energy Research Institute*, Apr. 2001.

[2] R. K. Tyson, *Adaptive Optics*. CRC publication, 2006.

[3] J. ,. Herrmann, "Least-squares wave front errors of minimum norms," *J. Opt. Soc. Am*, 1980.

[4] M. B. ,. Roopashree, "Experimental evaluation of centroiding algorithms at different light intensity and noise levels," in , 2011.

[5] "Estimates of precipitable water vapour from GPS data over the Indian subcontinent," *J. atmospheric & solar terrestrial physics*, 1999.

[6] J. ,. Porter, *Adaptive Optics for vision science*. Wiley interscience, 2005.

[7] D. L. ,. Fried, "Least square fitting a wave-front distortion estimate to an array of phase difference measurements," *J. Opt. Soc. Am*, vol. 67, p. 370, 1977.

[8] M. B. ,. Roopashree, "PERFORMANCE ANALYSIS OF FOURIER AND VECTOR MATRIX MULTIPLY METHODS FOR PHASE RECONSTRUCTION FROM SLOPE MEASUREMENTS," *ICOP*, 2009.

[9] L. A. U. ,. Larsoon, " Activities in Adaptive Optics- Characterisation of components," *Swedish Defence Reasearch Agency*, 2000.

[10] R. K. Tyson, *Principles of Adaptive Optics (Academic press Newyork)*. Newyork: CRC Press, 1998.

Simulation of Optical Gain in Type-I GaAsP/AlGaAs Nano-heterostructures

H. K. Nirmal[a], F. Rahman[b], M. J. Siddiqui[c], P. A. Alvi*[a]

[a]Department of Physics, Banasthali University, Banasthali Vidyapith-304022, Rajasthan (INDIA)
[b]Department of Physics, Aligarh Muslim University, Aligarh-202022, UP (INDIA)
[c]Department of Electronics, Faculty of Engineering and Technology, Aligarh Muslim University, Aligarh-202022, UP (INDIA)

ABSTRACT

This paper emphasizes over numerical simulation of optical gain existing in the type-I GaAsP/AlGaAs nano-heterostructures. The entire structure is assumed to be grown over the GaAs substrate. In order to calculate the optical gain of the structure, first the 4 x 4 Kohn-Luttinger Hamiltonian is solved to determine the sub-band dispersion and corresponding envelope wave functions; and then transition matrix elements calculations is designed to perform calculations of momentum matrix elements and dipole moments of selected transitions taking into account spin concept of the charge carriers. The calculated optical gain corresponding to maximum intensity meets at photonic energy ~ 1.64 eV and at corresponding wavelength ~ 756 nm. The maximum gain value corresponds to e1-hh1 transitions. The simulated results are found to match with experimental results. The experimental EL (electroluminescence) spectra for the simulated heterostructure are also found in match.
Keywords: Nano-heterostructure, Optical gain, GaAsP, AlGaAs, K.P Method, Type-I structure

1. INTRODUCTION

Heterostructures are very important for opto-electronic device applications [1]. There has been progressive evolution and radical changes in the history of semiconductor lasers. The idea of degenerately doped p-n junction based semiconductor laser was introduced in 1961 [2]. A very important point was marked that lower current densities could be obtained if the semiconductors forming the p-n junction have different forbidden gaps. Later on the concept of double heterostructure was proposed and developed [3]. In the double heterostructures (DHs) based lasing structures, an active media of extremely thin quantum well layer of narrow gap semiconductor were embedded in a wide gap barrier. Researchers have approached a lot of techniques to study the performance of semiconductor lasing heterostructures. These include numerical modeling, analytical solution or circuit modeling of rate equations determining the physical line of action of lasing heterostructures [4-6]. Recently, R. Yadav et al. [7] have simulated the optical gain of $In_{0.90}Ga_{0.10}$ $As_{0.59}P_{0.41}$/InP lasing nano-heterostructure and found that the maximum gain is corresponding to the wavelength lying in the near infra red region.

The present paper focuses on the numerical simulation of optical gain and analysis of the gain spectrum of *p*-$Al_{0.45}Ga_{0.55}As$/$GaAs_{0.84}P_{0.16}$/*n*- $Al_{0.45}Ga_{0.55}As$ diode structure that consists of QW (quantum well) of thickness 140 Å and material GaAsP sandwiched between AlGaAs layers of thickness 100 Å. The overall structure is supposed to be grown on GaAs. The reason behind the selection of GaAs substrate is the matching of lattice constants between the substrate and AlGaAs layers in order to avoid the strain factor.

*E-mail corresponding author: drpaalvi@gmail.com; Phone: +91-1438-228647

2. THEORETICAL BACKGROUND

The valence and conduction band profiles, as well as size quantized levels and wave functions of electrons and holes in the $GaAs_{0.84}P_{0.16}$ QW under investigation were numerically calculated. The numerical calculations were performed in the framework of the program "Heterostructure Design Studio 2.25" in the vicinity of the zone centre at the Γ point. There was used the model developed in [8], which considers the 4×4 Luttinger-Kohn Hamiltonian and describes the conduction band, light and heavy hole subbands but doesn't take into account the valence split-off subband because it does hang about 300 meV below the top of the valence band in $GaAs_{0.84}P_{0.16}$ [9].

In the calculations, the hole wave functions were expanded in basis functions of Luttinger-Kohn representation with the total angular momentum J = 3/2, and its projections $m_J = \pm 1/2$ and $m_J = \pm 3/2$ correspond to light holes and heavy holes respectively [8]. From the electron and hole wave functions, matrix elements of electron-photon interaction operator for interband transitions and, further, optical gain may be calculated. The optical gain was calculated for the TE (Transverse Electric) mode using the standard gain expression [10-13].

3. RESULTS AND DISCUSSION

The band dispersion for the bulk GaAsP material (on substrate AlGaAs) has been calculated by using eight-band Kane model along k_z with setting k_x and $k_y = 0$. The dispersion curve of bulk GaAsP has been shown in figure 1 (a). In figure 1 (a), it is clear that conduction band is almost parabolic while the valence subbands (Light, Heavy and Split off holes) are not. It has also been shown that light hole subband is above the heavy hole subband indicating that there is little lattice mismatch between the substrate GaAs and GaAsP QW. This mismatching shows the tensile strain in the QW.

After studying the band structure of bulk GaAsP material, the calculations have been performed for $GaAs_{0.84}P_{0.16}$ QW. The performed calculations shows that in the strained $GaAs_{0.84}P_{0.16}$ QW within the heterostructure, the first light hole (LH1) level is the ground state in valence band while the first heavy hole (HH1) level is the next one in the energy scale; refer to figure 1 (b). Next, from the electron and hole wave functions, matrix elements of electron-photon interaction operator for interband transitions and, further, optical gain have been calculated.

Optical transitions between the lowest electron level E1 and the highest hole level LH1 in the valence band determine an optical gap that is equal to the experimentally observed emitted photon energy. The calculated optical gain has been shown in figure 2. In figure 2, the spin dependent optical gain due to individual electrons and holes having parallel and anti-parallel spins is shown. The total optical gain has also been shown. The total optical gain corresponding to maximum intensity has been optimized at photonic energy ~ 1.64 eV and at corresponding wavelength ~ 756 nm (NIR region), that is found agreed with the experimental result; see figure 3.

4. CONCLUSION

The 4 x 4 Kohn-Luttinger Hamiltonian has been solved to determine the sub-band dispersion and corresponding envelope wave functions for p- $Al_{0.45}Ga_{0.55}As/GaAs_{0.84}P_{0.16}$/n- $Al_{0.45}Ga_{0.55}As$ nano-heterostructure. Taking into account spin concept of electron and hole, the transition matrix elements calculations is designed to perform calculations of momentum matrix elements and dipole moments of selected transitions. Finally, the optical gain for the structure has been calculated. The calculated optical gain corresponding to maximum intensity meets at photonic energy ~ 1.64 eV and at corresponding wavelength ~ 756 nm (NIR region), that is found agreed with the experimental result.

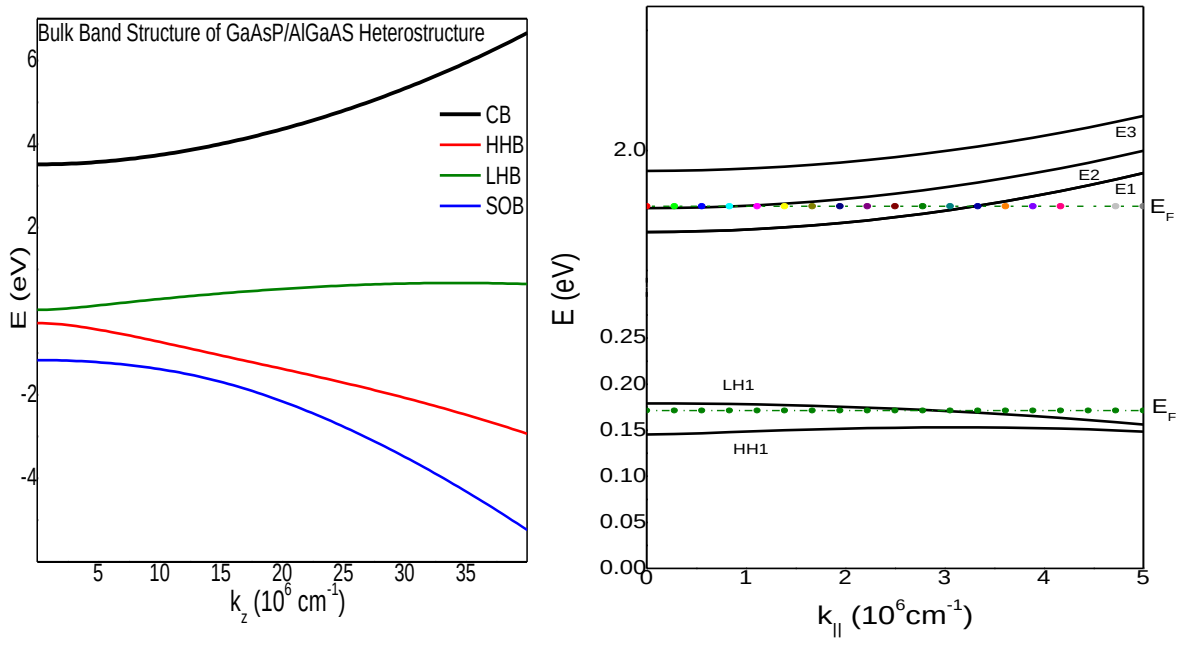

(a) **(b)**

Figure 1. Energy band structure of (a) bulk GaAsP (b) GaAsP quantum well of 14 nm width formed in structure.

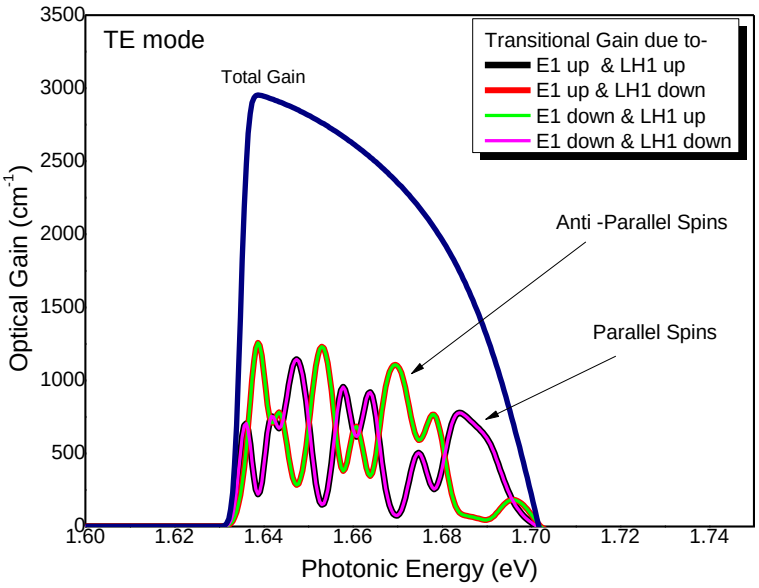

Figure 2. Optical gain of *p*- $Al_{0.45}Ga_{0.55}As/GaAs_{0.84}P_{0.16}$/*n*- $Al_{0.45}Ga_{0.55}As$ nano-heterostructure.

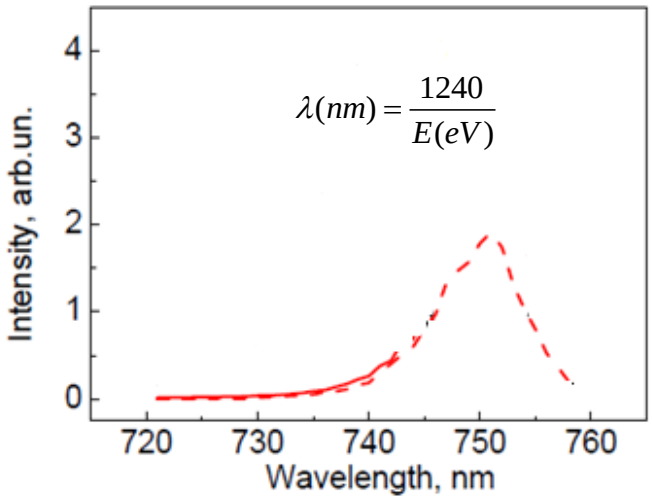

Figure 3. Plot of Intensity versus wavelength (Experimental result; ref. 8)

ACKNOWLEDGEMENT

P. A. Alvi is thankful to Prof. Aditya Shastri (Vice-Chancellor, Banasthali University) for supporting the research work. Authors are also thankful to Dr. Konstantin I. Kolokolov (Physics Department, M. V. Lomonosov Moscow State University, Leninskie Gory 1, 119991 Moscow, Russia) for providing the software package.

REFERENCES

[1] P. A. Alvi, Sapna Gupta, Puja Vijay, G. Sharma, M. J. Siddiqui, "Affects of Al concentration on GaN/$Al_xGa_{1-x}N$ new modeled multilayer nano-heterostructure" Physica B: Condensed Matter, Vol. 405, Issue 17, pp. 3624-3629 (2010).

[2] N. G. Basov, O. N. Krokhin, and Yu. M. Popov, "Production of negative-temperature states in p–n junctions of degenerate semiconductors," JETP, 40, 1320 (1961).

[3] Zh. I. Alferov and R. F. Kazarinov, "Double heterostructure laser", Authors Certificate no. 27448, Application no. 950 840, priority from March 30 (1963).

[4] T. W. Carr and T. Erneux, "Dimensionless rate equations and simple conditions for self-pulsing in laser diodes," IEEE J.Quantum Electron., 37, 1171-1177 (2001).

[5] L. Ansari, A. Zarifkar, and M. K. Moravvej-Farshi, "A circuit model for analyzing SCH- QW lasers considering chirp characteristic," in Proc. 4th Int. Conf Optical Communications and Networks (ICOCN), Bangkok, Thailand, 332-335 (2005).

[6] M. R. Salehiand B. Cabon, "Circuit modeling of quantum-well lasers for optoelectronic integrated circuits (ICs)including physical effect of deep-level traps", IEEE J. Quantum Electron, 38, 1510-1514 (2002).

[7] Rashmi Yadav, Pyare Lal, F. Rahman, S. Dalela, and P. A. Alvi, "Investigation of material gain of $In_{0.90}Ga_{0.10}As_{0.59}P_{0.41}$/InP lasing nano-heterostructure" International Journal of Modern Physics B, Vol. 28, No. 10, 1450068 (2014).

[8] K I Kolokolov, A M Savin, S D Beneslavski, N Ya Minina and O P Hansen, "Energy spectrum and topology evolution of the Fermi surface of two-dimensional holes in GaAs/$Al_{0.5}Ga_{0.5}$As heterostructures under uniaxial compression: Theory and experiment" Phys. Rev. B 59 7537 (1999).

[9] I. Vurgaftman, J. R. Meyer and L. R. Ram-Mohan, "Band parameters for III-V compound semiconductors and their alloys" J. Appl. Phys. 89 5815 (2001).

[10] S. L. Chuang, Physics of Optoelectronic Devices, Wiley, New York, (1995).
[11] P. A. Alvi, Pyare Lal, S. Dalela, M. J. Siddiqui, "An Extensive Study on Simple and GRIN SCH based $In_{0.71}Ga_{0.21}Al_{0.08}As$/InP Lasing heterostructure", Physica Scripta, 85, 035402 (2012).
[12] P. A. Alvi, Pyare Lal, Rashmi Yadav, Shobhna Dixit, S. Dalela, "Modal gain characteristics of GRIN-InGaAlAs/InP lasing nano-heterostructures" Superlattices and Microstructures, Vol. 61, pp. 1-12 (2013).
[13] P. A. Alvi, "Strain-induced non-linear optical properties of straddling-type indium gallium aluminum arsenic/indium phosphide nanoscale-heterostructures", Materials Science in Semiconductor Processing, Vo. 31 pp. 106-115 (2015).

Determination of linewidth enhancement factor of a semiconductor laser through post-detection dc level measurement of an IM-FM lightwave

Taraprasad Chattopadhyay*, Prosenjit Bhattacharyya, Chiranjib Ghosh
Department of Physics, Visva-Bharati University, Santiniketan, West Bengal-731235, India
Email:*tara_vb@hotmail.com

ABSTRACT

In this paper, we have proposed and demonstrated a simple and novel method of linewidth enhancement factor (LEF) determination of a semiconductor laser lasing at 1557.1 nm which requires no high-cost optical equipment like an optical spectrum analyzer. The Method is based on narrowband optical frequency modulation (FM) generation in the direct modulation of the laser diode, which implies that only the carrier and two first order sidebands are significant in the spectrum of the optical FM part. Second and higher order sidebands are neglected in the narrowband FM case while calculating the FM index. The FM index is calculated from the post-detection dc level measurement in a InGaAs photodiode. The LEF is computed from a knowledge of FM and IM indices. The outcome of this paper is that the LEF decreases linearly with increasing bias current of the laser diode above threshold for a given intensity modulation (IM) index. The calculations hold good so long as the generated optical FM is narrowband in character.

Keywords: Semiconductor laser, linewidth enhancement factor, intensity modulation, frequency modulation, photodiode.

1. INTRODUCTION

Laser is a coherent source of light. It has a narrow linewidth. The linewidth of a laser is predicted by Schawlow-Townes formula[1] where the linewidth varies inversely with the laser output power. Although this formula predicts the linewidth satisfactorily for gas lasers, it fails to predict the linewidth for semiconductor lasers. C. H. Henry in his paper[2] introduced the concept of a factor called as the linewidth enhancement factor (α) which modifies the Schawlow-Townes formula for linewidth as $\Delta\nu_H = \Delta\nu_{ST}\left(1+\alpha^2\right)$. Here, $\Delta\nu_H$ is the actual linewidth of the semiconductor laser as calculated from Henry formula and $\Delta\nu_{ST}$ is the linewidth predicted by Schawlow-Townes formula.

The linewidth enhancement factor (LEF) modifies the fundamental characteristics of a semiconductor laser to a great extent, such as broadening of linewidth, chirp or frequency variation of the laser under direct modulation of the laser diode, phenomenon of optical injection locking making the locking range asymmetric around the free-running lasing frequency, modal stability and behavior of the laser diode under feedback. Thus, the LEF affects the phenomenon of a semiconductor laser adversely in the field of high speed coherent communication.

The linewidth enhancement factor (α) is defined as $\alpha = -\frac{4\pi}{\lambda}\frac{\partial n/\partial N}{\partial G/\partial N}$, where λ is the wavelength of the laser diode (LD), n is the refractive index of the active region of the laser, N is the carrier concentration and G is the linear gain of the active region of the LD. Since $\frac{\partial n}{\partial N} < 0$, α is a positive quantity.

Several methods[3-22] have been proposed and demonstrated for the measurement of LEF in semiconductor laser. These are determination of α by measuring lockband asymmetry of an injection-locked laser[3,4], measurement of optical sideband amplitude[5] generated through rf modulation of a LD, interferometric measurement[6], and amplified spontaneous emission method[7]. These techniques often require a costly equipment like an optical spectrum analyzer for measurement.

2. EXPERIMENTAL SETUP

The experimental arrangement is shown in Figure 1 below. A laser diode (LD) lasing at 1557.1 nm is bias current-modulated and operated above the threshold level of the LD. The dc bias current and the modulating signal current are added through a bias tee and applied to the LD. The dc bias current is set well above the threshold current ($I_{th} = 41.6$ mA) so that the bias current swing does not bring down the operating point below the threshold level.

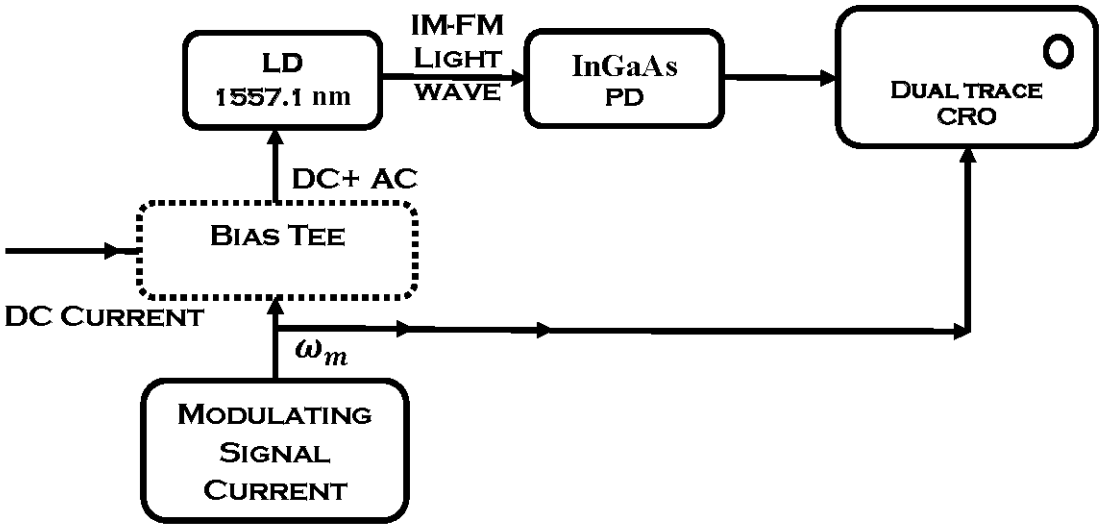

Figure 1. Experimental circuit diagram for the determination of linewidth enhancement factor of the LD.

The output of the LD is a lightwave which is simultaneously intensity and frequency modulated. The frequency modulation index kept very small typically below 0.5 in order that the generated FM is a narrowband one. In narrowband FM only the carrier and two sidebands on either side of the carrier are present. Second and higher order sidebands being very small in amplitude can be neglected in narrowband FM. This narrowband IM-FM signal when detected in the InGaAs photodiode we get a signal and dc whose magnitude depend upon the FM index of the narrowband FM. Since LEF is directly related with the FM index, we can determine the LEF of the LD by this method.

3. ANALYSIS

Let m be the intensity modulation index and m_f denote the FM index of the generated narrowband IM-FM lightwave. The linewidth enhancement factor (α) is calculated from the relation $\alpha = (2m_f / m)$. It has been found[22] that the contribution to LEF due to adiabatic chirp is very small even in the low modulation frequency region. The modulated intensity of the Fabry-Perot laser diode (FPLD) is represented as

$$I(t) = I_0(1 + m\cos\omega_m t) \tag{1}$$

where I_0 is the laser intensity in absence of modulation, m is the intensity modulation (IM) index and ω_m is the modulation frequency in radian. The frequency modulation of the LD is described by $\sin(\omega_c + m_f \sin\omega_m t)$, where ω_c is the lightwave carrier frequency in radian. We restrict the IM index, $m <$ 10 % so that the generated FM has an index $m_f < 0.5$. Under this condition, the FM lightwave is said to be a narrowband FM. In narrowband FM, only the first order sidebands on either side of the carrier will have significant amplitude while second and other higher order sidebands will have much smaller amplitudes so that they can be neglected in power calculation of the FM lightwave.

The output current of the photodiode (I_{PD}) is expressed as

$$\begin{aligned} I_{PD} &= \eta P_{in} \\ &= \eta \alpha_e I_0 (1 + m\cos\omega_m t)\left[J_0^2(m_f) + 2J_1^2(m_f)\right] \end{aligned} \tag{2}$$

where P_{in} is the input optical power of the photodiode (PD), η is the responsivity of the PD, α_e is the emission cross-section of the LD. we can write, $\alpha_e I_0 = P_0$ where P_0 is the unmodulated power of the LD.

The output voltage of the PD is given by

$$\begin{aligned} v_{PD} &= I_{PD} R_L \\ &= \eta P_0 R_L (1 + m\cos\omega_m t)\left[J_0^2(m_f) + 2J_1^2(m_f)\right] \end{aligned} \tag{3}$$

where R_L is the photodiode load resistance. Now, v_{PD} is a combination of dc and ac voltages. The dc voltage output of the PD is written as

$$v_{DC} = \eta P_0 R_L \left[J_0^2(m_f) + 2J_1^2(m_f)\right] \tag{4}$$

v_{DC} is experimentally measured, η is determined from the response of the PD, P_0 is measured by an optical power meter and R_L is known. Then, the FM index (m_f) of the generated FM lightwave is determined from the relation

$$J_0^2(m_f) + 2J_1^2(m_f) = \frac{v_{DC}}{\eta P_0 R_L} \tag{5}$$

The variation of FM index (m_f) with the LD bias current above threshold is plotted in Figure 2. It is seen from Figure 2 that the FM index decreases linearly with the increase in LD bias current above threshold for a fixed IM index (m) equal to 5%.

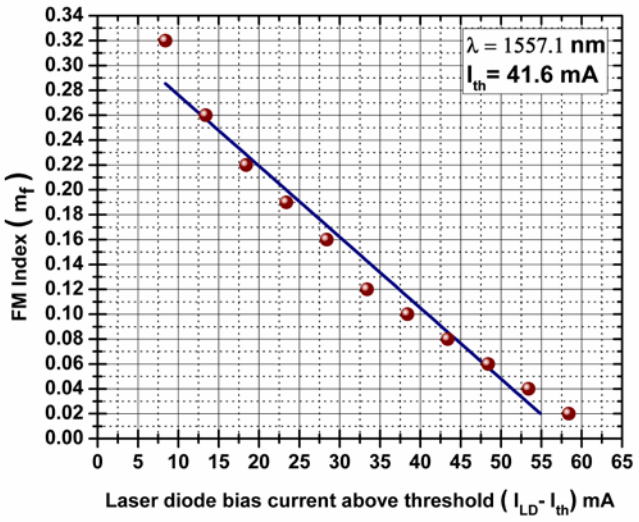

Figure 2. Variation of FM index (m_f) with LD bias current above threshold. The straight line is an empirical fit.

The IM index (m) is calculated from the following relation

$$m = \frac{I_{\text{mod}}}{I_{LD} - I_{th}} \tag{6}$$

whrere I_{mod} is the modulating signal current amplitude. I_{LD} is the laser diode current and I_{th} is the threshold current of the LD. The LD modulation frequency is 3 MHz, modulation sensitivity $S = 0.1$ mA/mW, load resistance (R_L) of the PD is 50Ω. Laser diode temperature is kept constant at $23^0 C$. Threshold current (I_{th}) of LD is 41.6 mA. Lasing wavelength (λ) is 1557.1 nm. The linewidth enhancement factor (LEF) calculated from the relation $\alpha = (2m_f / m)$ is plotted in Figure 3. The LEF decreases linearly with the LD bias current above threshold (Figure 3).

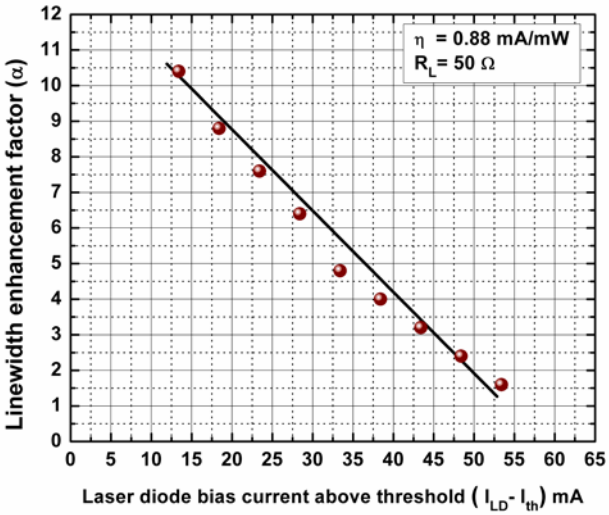

Figure 3. Variation of Linewidth enhancement factor (α) with LD bias current above threshold. The straight line is an empirical fit.

The reason for this fall of LEF with LD bias current is given as follows. An increase in LD bias current produces a corresponding increase in carrier concentration in the active region of the LD. The refractive index of the active region decreases with the increase in carrier concentration. The linear gain of the active medium increases with the increase in carrier concentration. As a result, the numerator in the expression for LEF in the introduction decreases and the denominator increases. This produces a fall in LEF with the increasing carrier concentration and hence with the LD bias current above threshold.

4. CONCLUSION

A simple and novel method of linewidth enhancement factor determination through post-detection dc level measurement of a directly modulated FPLD generating a narrowband FM signal has been presented and demonstrated in this paper. The LEF decreases linearly with increasing bias current of the LD above threshold which has been explained in this paper. The variation of LEF with LD bias current follows from a linear fall in optical FM index with LD bias current, the IM index being kept fixed at 5% level. The theory is based on narrowband optical FM generation and as such its accuracy is better the smaller is the value of the FM index. Departure from the linear nature of fall of LEF with LD bias current is seen as the FM index tends to be higher.

5. ACKNOWLEDGEMENT

The authors are thankful to the Council of Scientific and Industrial Research (CSIR), New Delhi for providing funds for this research work under project no. 03(1291)/13/EMR-II.

REFERENCES

[1] Schawlow A. L. and Townes C. H., "Infrared and optical masers," Phys. Rev. 112 (6), 1940 (1958).

[2] Henry C. H., "Theory of linewidth of semiconductor lasers," IEEE J. Quantum Electronics, QE-18, 259-264 (1982).

[3] Liu G., Jin X. and Chuang S. L., "Measurement of linewidth enhancement factor of semiconductor lasers using an injection locking technique," IEEE Photon. Tech. Lett., 13(5), 410-412 (2001).

[4] Iiyama K., Hayashi K. and Ida Y., "Simple method for measuring the linewidth enhancement factor of semiconductor laser by optical injection locking," Optics Lett., 17, 1128-1130 (1992).

[5] Li H., "RF modulation measurement of linewidth enhancement factor and nonlinear gain of vertical cavity surface emitting lasers," IEEE Photon. Tech. Lett., 8, 1594-1596 (1996).

[6] Ehrhardt J., Vilkeneuve A., Stegeman G. I., Nakajima H., Laudreau J. and Ougazzaden A., "Interferometric measurement of the linewidth enhancement factor of 1.55μm strained multi quantum well InGaAs-InGaAsP amplifier," IEEE Photon. Tech. Lett., 4 (12), 1335-1338 (1992).

[7] Newell T. C., Dessert D. J., Stintz A., Fuch B., Malley A. J. and Lester L. F., "Gain and linewidth enhancement factor in InAs quantum dot laser diodes," IEEE Photon. Tech. Lett., 11, 1527-1529 (1999).

[8] Agrawal G. P., "Intensity dependence of the linewidth enhancement factor and its implications for semiconductor lasers," IEEE Photon. Tech. Lett., 1 (8), 212-214 (1989).

[9] Harder C., Vahala K. and Yariv A., "Measurement of linewidth enhancement factor α of semiconductor lasers," Appl. Phys. Lett., 42 (4), 328-330 (1983).

[10] Kudo K., Shim J. I., Komori K. and Arai S., "Reduction of effective linewidth enhancement factor αeff of DFB lasers with complex coupling coefficient," IEEE Photon. Tech. Lett. 4, 531-533 (1992).

[11] Gan K-G. and Bowers J. E., "Measurement of gain, group index, group velocity dispersion and linewidth enhancement factor of an InGaN multiple quantum well laser diode," IEEE Photon. Tech. Lett., 15 (5), 1256-1258 (2004).

[12] Provost J. –G. and Grillof F., "Measuring the chirp and the linewidth enhancement factor of optoelectronic devices with a Mach-Zehnder interferometer," IEEE Photon. Journal, 3 (3), 476-488 (2011).

[13] Nillafranca A., Lazaro J. A., Salinas I. and Gaoces I., "Measurement of linewidth enhancement factor in DFB laser using a high resolution optical spectrum analyzer," IEEE Photon. Tech. Lett., 17 (11), 2268-2271 (2005).

[14] Yu Y., Ginliani G. and Donati S., "Measurement of linewidth enhancement factor of semiconductor lasers based on optical feedback self-mixing effect," IEEE Photon. Tech. Lett., 11 (4), 990-992 (2004).

[15] Li W., Zhi W., Huang, W-P., "Linewidth enhancement factor for ultrafast dynamics in bulk semiconductor optical amplifiers," Proc. Conference on Lasers & Electro Optics & The Pacific Rim Conference on Lasers and Electro-Optics (CLEO/PACIFIC RIM '09), 1-2, (2009). doi: 10.1109/CLEOPR.2009.5292158.

[16] Yanguang Y., Jiangtao X., Chicharo J.F., T. Bosch, "Toward automatic measurement of the linewidth-enhancement factor using optical feedback self-mixing interferometry with weak optical feedback," IEEE J. Quantum Electronics, 43 (7), 527-534 (2007).

[17] Villafranca A., Villafranca A., Giuliani G., Garces I., "Mode-resolved measurements of the linewidth enhancement factor of a Fabry–Perot laser," IEEE Photon. Tech. Lett., 21 (17), 1256-1258 (2009).

[18] Miloszewski J. M., Wartak M.S., Weetman P., Hess O., "Analysis of linewidth enhancement factor for quantum well structures based on InGaAsN/GaAs material system," J. Appl. Phys., 106 (6), 063102 - 063102-5 (2009).

[19] Provost J., Grillot F., "Measuring the linewidth enhancement factor of optoelectronics devices based on a Mach-Zehnder interferometer," Proc. 23rd Annual Meeting of the IEEE Photonics Society, 425-426 (2010). doi: 10.1109/PHOTONICS.2010.5698941.

[20] Shu-Wei C.,"Dressed Linewidth Enhancement Factors in Small Semiconductor Lasers," IEEE Journal of Selected Topics in Quantum Electronics, 21 (6), Article#: 1500408 (2015), doi: 10.1109/JSTQE.2014.2359542.

[21] Joshi S., Chimot N., Ramdane A., Lelarge F., "On the nature of the linewidth enhancement factor in p-doped quantum dash based lasers," Appl. Phys. Lett., 105 (24), 241117 - 241117-3 (2014). doi: 10.1063/1.4904831.

[22] Nguyen Q-T., Besnard P., Vaudel O., Shen A. and Duan G-H., "Strong dependance of the linewidth enhancement factor onto an externally injected optical signal for locked Fabry-Perot laser diode," Proc. Lasers and Electro-optics 2009 and the European Quantum Electronics Conference (CLEO Europ-EQEC 2009), 1(2009). doi: 10.1109/CLEOE-EQEC 2009.5191594.

Influence of meridional and skew rays on evanescent field based absorption sensor

Siraj Sidhik[a], Jijo V Ittiarah[a] and Tarun Kumar Gangopadhyay*[a]
[a]CSIR - Central Glass and Ceramic Research Institute (CGCRI), Kolkata-700032, India
*Corresponding Author: tkg@cgcri.res.in

ABSTRACT

An optical fiber comprises of two classes of rays namely meridional rays and leaky skew rays. Evanescent field (EF) based absorption sensor deals with the interaction of evanescent wave with the desired analyte. The propagation of both meridional and skew rays results in the generation of EF. The major difference between them is the nature of propagation that influences the EF interaction in the sensor. A detailed analysis on the effect of meridional and skew rays on the evanescent field based absorption sensor is presented.

Keywords: evanescent field, meridional ray, skew ray, absorption

1. INTRODUCTION

Evanescent field (EF) based absorption technique turns out to be a milestone in the development of fiber optic chemical sensor [1]–[3]. An optical fiber allows the propagation of both meridional and skew rays which independently contributes to EF interaction [4]. As a result, the influence of both these rays on the evanescent wave absorption coefficient needs to be studied. Also, for the design of spectroscopy and sensor, a detailed analysis of meridional and skew rays in terms of evanescent field absorption is required. Evanescent field contribution of meridional rays can be expounded using Fresnel's law by considering the attenuated total internal reflection. The contrast in the nature of propagation of skew rays to the meridional rays makes it inapplicable to the Fresnel law.

In the present work, the theoretical analysis of evanescent wave absorption for meridional and skew rays is investigated. The quantitative proportion of meridional and skew rays is analyzed to validate its role in evanescent wave absorption spectroscopy which can be further utilized to optimize the design of evanescent field based fiber optic chemical sensor.

2. PRINCIPLE OF OPERATION

Consider a light ray of wavelength λ incident at point Q at the core-cladding interface of a step index optical fiber. The refractive index (RI) of the core is n_1 and the cladding is n_2. The schematic diagram is shown in Fig. 1. With respect to the normal QO, the angle of incidence and reflection of the propagating light ray is β. Both incident and reflected ray makes an angle θ_z with the axial direction QZ, θ_s represents the angle between the tangent to point Q and the projection of the reflected ray R.

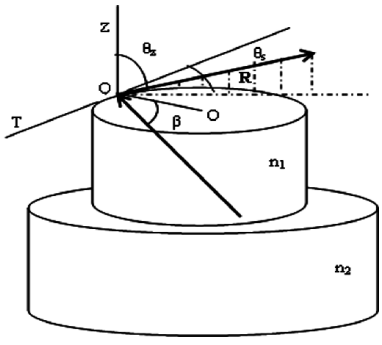

Fig. 1 Schematic diagram of light propagation through step index optical fiber

For an optical fiber, having large core diameter (V > 1) geometric optics proves to be an effective method for analysis and hence it is used for the analysis of absorption coefficient of meridional rays and skew rays. Let P_0 be the power transmitted through the optical fiber in the absence of an absorbing medium then the evanescent wave that is generated is represented by,

$$P=P_0\exp(-x/dp) \tag{1}$$

where x is the perpendicular distance from the interface, dp is the penetration depth. The penetration depth is given by,

$$dp=\frac{\lambda}{2\pi n_1\sqrt{\sin^2\theta-(n_2/n_1)^2}} \tag{2}$$

When the cladding region is replaced by an absorbing medium, the RI of the cladding is denoted as $n_2 = n_1 - jn_{2*}$ and the bulk absorption coefficient of the provided absorbing medium is given by [5]

$$\alpha=\frac{4\pi n_2^*}{\lambda} \tag{3}$$

where n_2* represents a constant value. Assuming weak absorption, the evanescent wave absorption coefficient for meridional rays is given by [5]

$$\gamma_m(\theta_z)=\frac{\alpha\lambda n_2\sin^2\theta_z}{\pi d\cos\theta_z\sqrt{\cos^2\theta_z-(n_2/n_1)^2}\,(n_1^2-n_2^2)} \tag{4}$$

Similarly, the evanescent wave absorption due to leaky skew rays is given by [5],

$$\gamma_s(\theta_z)=\left(\frac{\alpha^2\lambda^2}{4\pi^2 dn_1\sqrt{n_1^2-n_2^2}}\right)\left(\frac{\theta_z}{\theta_c}\right)^2\left[\sqrt{1-\left(\frac{\theta_z}{\theta_c}\right)^2\sin^2\theta_s}\right]\times\exp\left[\left(-\frac{2}{3}V\right)\frac{(1-(\theta_z/\theta_c)^2\sin^2\theta_s)^{3/2}}{(\theta_z/\theta_c)^2-1}\right] \tag{5}$$

where θ_c is the critical angle and V is normalized frequency parameter.

3. RESULTS AND DISCUSSION

The theoretical analysis of evanescent wave absorption for meridional and skew rays is presented here. The quantitative proportion of meridional and skew rays is analyzed to validate its role in evanescent wave absorption spectroscopy. The evanescent wave absorption coefficient of meridional rays for three different absorbing medium is presented in Fig.2

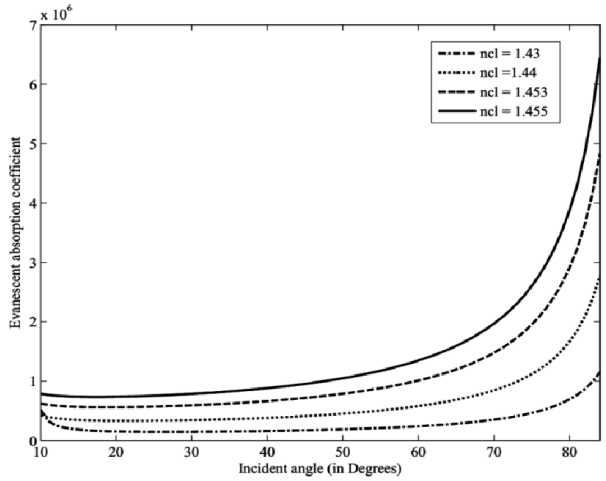

Fig. 2 Evanescent wave absorption coefficient for meridional rays propagating through optical fiber

Here the angle of incidence is varied continuously and it is observed that when the angle of incidence becomes equal to or greater than the critical angle, the evanescent wave absorption coefficient increases drastically. It is also observed from the simulation results that as the refractive index of the absorbing medium become closer to that of the core refractive index (weakly guided condition) the evanescent wave absorption coefficient increases. Similarly, the

evanescent wave absorption coefficient for leaky skew rays as a function of incident angle θ_z for θ_s of 10º and 30º is simulated and presented in Fig. 3.

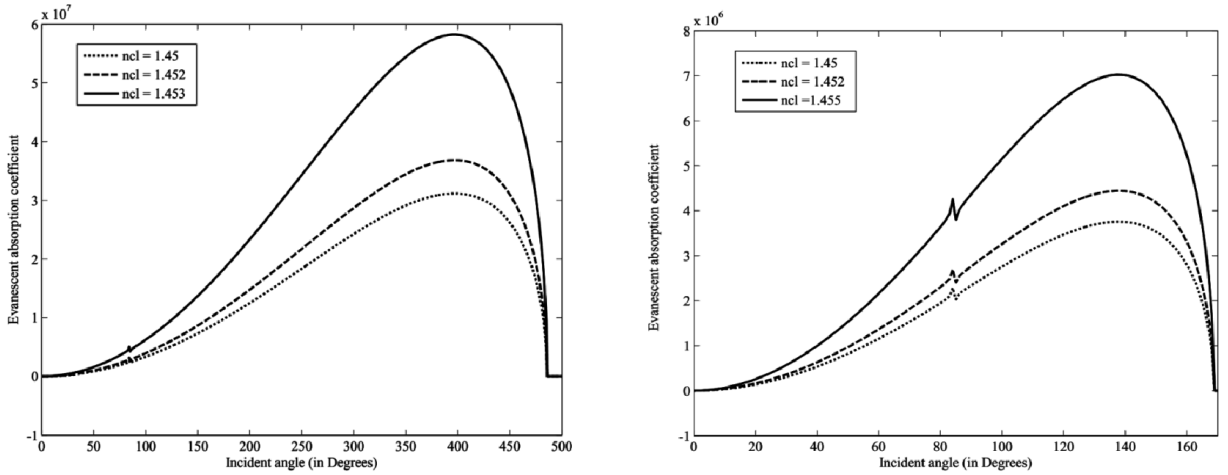

Fig. 3 (a) Evanescent wave absorption coefficient at θ_s of 10º (b) Evanescent wave absorption coefficient at θ_s of 30º

From the plot it can be observed that, the evanescent wave absorption for leaky skew rays exist over a wider range compared to meridional rays. It can also be noted that the evanescent wave absorption coefficient for skew rays increases once the angle of incidence becomes greater that the critical angle. From the two plots we can see that as the skewness parameter (θ_s) increases, the evanescent wave absorption coefficient increases. Fig. 4 illustrates the comparison of evanescent wave absorption coefficient for meridional and leaky skew rays. The contrast in the range of absorption for both these rays is completely evident from the simulated plot.

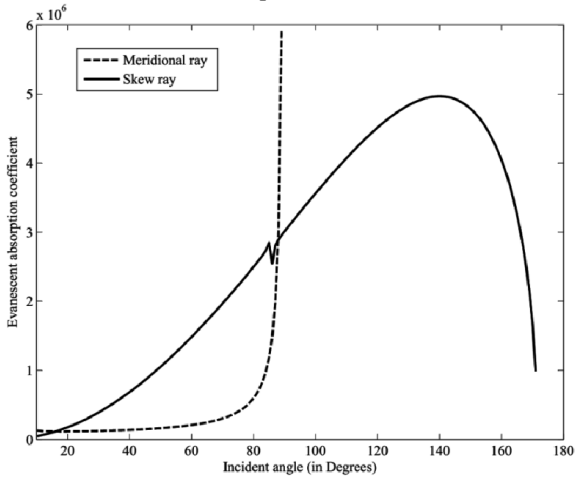

Fig. 4 Comparison of evanescent wave absorption coefficient for meridional and skew rays

The evanescent wave absorption coefficient for meridional ray is much higher compared to that of the leaky skew rays. But the major difference between them is that, the leaky skew rays are distributed over a wider range, normally several times θc. Whereas, meridional ray occur only within the critical angle (less than θc) as predicted by the Fresnel law. It is observed from the results that the leaky skew rays are smaller but their contribution is distributed over larger range. As a result in certain application the evanescent wave absorption of leaky skew rays should be explained for the analysis of the experimental results. Fig. 5 shows the percentage of power transmitted by the meridional rays to the total power transmitted through the optical fiber. It can be observed that the proportion of meridional rays is less than 50 % when the RI of the absorbing medium is close to that of core RI (weakly guiding condition).

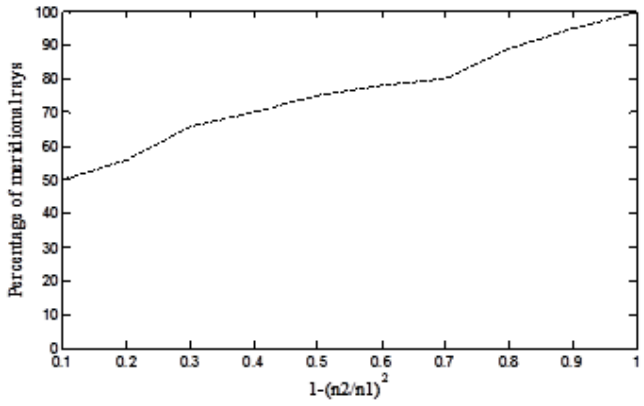

Fig. 5 Percentage of light power transmitted by meridional rays to total power transmitted through the fiber

4. CONCLUSION

The importance of meridional and skew rays in evanescent field based absorption for application in chemical sensing is studied in detail. A three dimensional model of uncladded step index optical fiber considering the principle of geometric optics is formulated. The optical fiber is modeled to be immersed in different absorbing media i.e. the chemical sample. Results of this study shows that evanescent wave absorption of meridional rays is more pronounced compared to the skew rays but the extent of absorption for skew rays is prominent for wide range of incident angle. This theoretical work can be utilized to optimize the design of evanescent field based fiber optic chemical sensor.

5. ACKNOWLEDGEMENT

The research work is supported by the sponsored project (No. GAP0141) from DST, Govt. of India. The author would like to acknowledge the support of the Director, CGCRI, Dr. Mukul Paul, Dr. M. Pal and Dr. Shyamal Das of FOPD, CGCRI, Kolkata for their help.

6. REFERENCES

[1] Y. Xu, A. Cottenden, and N. B. Jones, "A theoretical evaluation of fibre-optic evanescent wave absorption in spectroscopy and sensors," *Opt. Lasers Eng.*, vol. 44, no. 2, pp. 93–101, Feb. 2006.

[2] M. Jiang, W. Zhang, Q. Zhang, Y. Liu, and B. Liu, "Investigation on an evanescent wave fiber-optic absorption sensor based on fiber loop cavity ring-down spectroscopy," *Opt. Commun.*, vol. 283, pp. 249–253, 2010.

[3] C. Wang, M. Kaya, and C. Wang, "Evanescent field-fiber loop ringdown glucose sensor.," *J. Biomed. Opt.*, vol. 17, p. 037004, 2012.

[4] A. Cozannet and M. Treheux, "Skew rays in optical fibers.," *Appl. Opt.*, vol. 14, no. 6, pp. 1345–50, Jun. 1975.

[5] B. D. Gupta and B. Das Gupta, *Fiber optic sensors: Principles and applications*. New India Publishing, 2006.

Design of optical finite impulse response filter generating arbitrary spectrum output

Arijit Saha[1], Kallol Bhattacharya[2] and Ajoy Kumar Chakraborty[2]

[1] Department of Electronics & Communication Engineering,
B P Poddar Institute of Management & Technology,
137, VIP Road, Kolkata, Pin 700052, India

[2]Department of Applied Optics & Photonics,
Calcutta University,
92, APC Road, Kolkata, Pin 700009, India
arijit_sh@yahoo.com

ABSTRACT

A procedure for the synthesis of an optical finite impulse response (FIR) birefringent filter generating arbitrary spectral output is presented. The basic filter consists of a cascaded system of *n* identical retarders between two polarizers at the two ends. A mathematical model of the optical FIR filter is introduced from the FIR theory of digital filter design. The parameters determined by the synthesis procedure are the angles of the optic axes of the crystals and the angle of the output polarizer. Classical FIR filter design method along with the optical backward transfer technique has been used. Two different arbitrarily specified spectral output profiles have been studied. However, the method is equally applicable for any periodic transfer function whose corresponding impulse response is real and causal.

Keywords. Birefringent chain filter, optical finite impulse response filter, arbitrary spectrum output, crystal birefringence

1 INTRODUCTION

Optical filter is one of the most important devices used in optical system spectrum crunching and optical signal processing. Present optical filters can be broadly classified into two types – birefringent filters and thin film filters. Birefringent filters are composed of a pile of birefringent elements which have the same or periodically repeating phase difference. The azimuths of the individual elements are arranged in prescribed manners with respect to the centre of the filter. The filter is placed in between two polarizers[1]. Since its inception, birefringent chain filters have undergone considerable development. Birefringent filters have been used widely, such as in the selection of laser wavelengths, endoscope imaging, observation of solar prominence, optical communication, etc.[2].

Though the idea of birefringent chain filters has appeared since a long time, but its application is limited to some extent due to the specific outputs it produces. The most common types are the Lyot and Solc filters. The retarders of varying thicknesses in Lyot filters are rotated in the same angle[3], while the retarders of identical thicknesses in Solc filters are arranged in spread-out fan or folded type[4]. This structural regularity results in simple narrowband spectrum output. However, in some other optical processing applications, like projection display and colour manipulations, a filter that is able to provide an arbitrary spectrum is required.

In this communication, we have proposed to design two different birefringent filters capable to produce two arbitrarily specified spectral outputs. We have concentrated on how to realize optical FIR filter producing arbitrary desired spectrums. The classical FIR theory in digital filter design is used to establish the mathematical model of this optical FIR filter. Once the coefficients are obtained they have been used to determine the actual orientation of each retarder by optical backward transfer technique. By the examples discussed here, we find that the main advantage of this filter is the ease of design and good performance of both spectrum and angle properties.

2 MODEL OF THE OPTICAL FIR FILTER

For a discrete and a causal system, the input and output of a digital filter can be described by a convolution in the time domain as[5]

$$y(n)=\sum_{k=-\infty}^{\infty}h(k)x(n-k) \tag{1}$$

where $x(n)$ is a discrete time series and $h(k)$ is the response of a unit sampling series $\delta(n)$. If $h(k)$ includes finite sampling dots only in the range $0 \le k \le N-1$ (N is finite), the system is called a finite impulse response digital filter. The frequency response of this FIR filter can be obtained by the Fourier transform.

$$H[\exp(i\omega T)]=\sum_{k=0}^{N-1}h(k)\exp(-ik\omega T) \tag{2}$$

In the frequency domain, a FIR filer is the sum of a finite Fourier series, and the coefficients of the Fourier series are unit impulse responses. This corresponds with an infinite discrete series distributed on the whole time axis.

The general structure of an optical FIR filter composed of a series of birefringent retarders is illustrated in figure 1. All the n birefringent crystal retarders are of identical length and composed of the same material. They are rotated at specific rotation angles and are between two polarizers. Due to the birefringence of the crystals, the o-light and e-light travel with different velocities and are separated. If a linear polarized light comes through the retarder, it is divided into two components along the fast-axis and the slow-axis, respectively, and they serve as the input of the second plate. The output of the second retarder can be combined into three different impulses in a time series along a fast-fast axis, fast-slow axis, and slow-slow axis, respectively. Hence, if we extend the filter for n identical crystals, then by analogy, we may say that $(n + 1)$ impulses will be produced with the identical time interval[6]. The corresponding impulse response is given by

$$\begin{aligned} C(t) &= C_0\delta(t)+C_1\delta(t-a)+C_2\delta(t-2a)+\cdots+C_n\delta(t-na) \\ &= \sum_{k=0}^{n}C_k\delta(t-ka) \end{aligned} \tag{3}$$

where a denotes the time interval of the impulse series and is given by

$$a = t_S - t_F = L\Delta\eta/c \tag{4}$$

Here t_S, t_F denote the time needed for the two impulses to pass through a single retarder, L is the length of birefringent crystal, c is the velocity of light in vacuum, and $\Delta\eta = n_e - n_o$, is the birefringence of the crystal. Birefringence is a function of frequency, but within the range of frequency under consideration, $\Delta\eta$ may be assumed to be constant. The phase difference caused by a single retarder is given by

$$\Gamma = \frac{2\pi\,\Delta\eta L}{\lambda} \tag{5}$$

where λ is the wavelength of the light. The exponential form of Fourier transform of Eq. (3) is expressed as:

$$\begin{aligned} C(\omega) &= C_0 + C_1\exp(-ia\omega)+C_2\exp(-i2a\omega)+\cdots+C_n\exp(-ina\omega) \\ &= \sum_{k=0}^{n}C_k\exp(-ika\omega) \end{aligned} \tag{6}$$

Now, we can express Eq. (6) in two other equaivalent ways as:

$$\begin{aligned} C(\omega) &= C_0 + C_1\exp(-i\Gamma)+C_2\exp(-i2\Gamma)+\cdots+C_n\exp(-in\Gamma) \\ &= \sum_{k=0}^{n}C_k\exp(-ik\Gamma) \end{aligned} \tag{7}$$

$$C(\lambda) = C_0 + C_1\exp\left(-i2\pi\Delta\eta\frac{L}{\lambda}\right)+C_2\exp\left(-i22\pi\Delta\eta\frac{L}{\lambda}\right)+\cdots+C_n\exp\left(-i2n\pi\Delta\eta\frac{L}{\lambda}\right)$$

$$= \sum_{k=0}^{n} C_k \exp\left(-ik2\pi\Delta\eta\frac{L}{\lambda}\right) \tag{8}$$

where $\omega = 2\pi f = 2\pi c/\lambda$ represents the angular frequency of the light wave. It changes the function which was non-periodic in spectrum into a periodic phase function. Theoretically the ideal frequency response should have been developed precisely as an infinite Fourier series, which corresponds to infinite number of retarders. But here we want to choose only a finite number of terms to approximate the actual target function. We can use different techniques used in digital FIR filter design to truncate the number of terms.

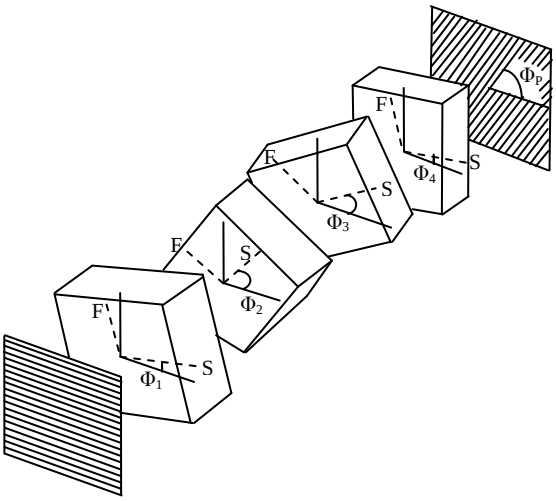

Fig. 1 Basic configuration of a four-stage optical FIR filter

3 OPTICAL IMPLEMENTATION OF THE FILTER

Here we have designed two different optical FIR filter. In the first case we have taken the arbitrary output spectrum to be a saw-tooth profile, whereas in the second example it is for a flat-top profile. We have shown the simulated profile for the saw-tooth case in figure 2. The flat-top profile output for the second filter designed, is illustrated in figure 3. Here we have shown the output transmittance with respect to wavelength in nm. We have used least-square filter design algorithm.

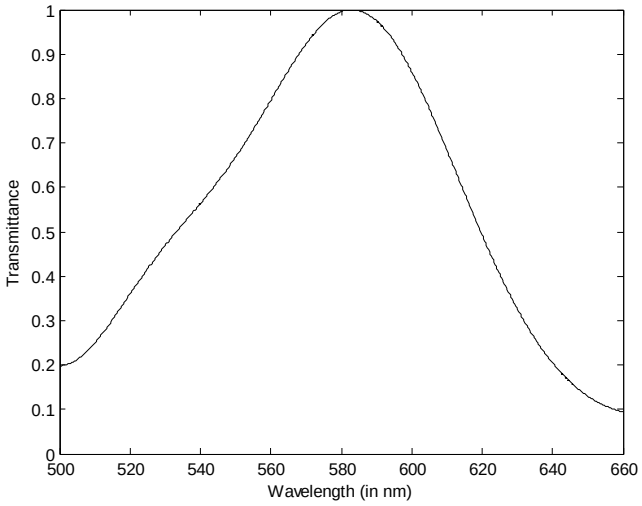

Fig. 2 Transmission of the designed saw-tooth spectral filter

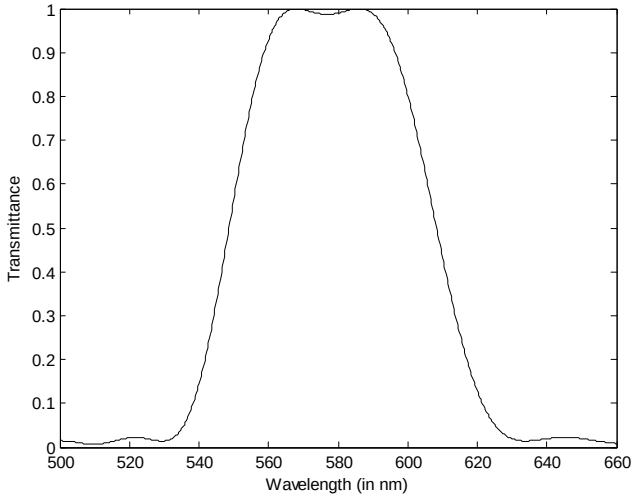

Fig. 3 Transmission of the designed flat-top spectral filter in the range 560 to 600 nm

Once the series of impulse responses is obtained, we now use the *optical backward transfer* method proposed by Harris *et al* [6]. Suppose the output component along the direction of the analyser is expressed in Eq. (6) and the corresponding perpendicular output is denoted by $D(\omega)$. It is of the same form as $C(\omega)$ and forms the complementary colour of $C(\omega)$. Hence,

$$D(\omega) = D_0 + D_1 \exp(-ia\omega) + D_2 \exp(-i2a\omega) + \cdots + D_n \exp(-ina\omega)$$

$$= \sum_{k=0}^{n} D_k \exp(-ika\omega) \tag{9}$$

If we ignore the crystal absorption, the two components satisfy the principle of energy conservation.

$$D(\omega)D^*(\omega) = I_0^2 - C(\omega)C^*(\omega) \tag{10}$$

where I_0^2 is the intensity of the incident light. In the optical system illustrated in figure 1, the direction of the polarizer is chosen along the *x*-axis. Rather than dealing with absolute angles of each crystal retarder relative to *x*, we define

$$\theta_1 = \Phi_1, \quad \theta_2 = \Phi_2, \ldots, \ \theta_n = \Phi_n - \Phi_{n-1}, \qquad \theta_p = \Phi_p - \Phi_n$$

as the relative angles of each retarder. The whole set of angles are determined from rear to front with the *optical backward transfer* method by using the relationship between the input and output of each retarder and its coordinates[6,7]. For the two filters designed, the corresponding C_k, D_k, and θ_k are listed in Table 1. Here $\theta_6 = \theta_p$ is the orientation of the final analyser.

Table 1 Numerical results of optical backward transfer method for the two filters designed

	Saw-tooth profile			Flat-top profile		
k	C_k	D_k	θ_k (in degrees)	C_k	D_k	θ_k (in degrees)
1	–0.0531	0.0308	30.6918	–0.0580	–0.4733	55.1006
2	0.0796	0.1478	54.8899	0.0346	–0.7782	56.1128
3	–0.1592	0.3815	47.4114	0.1037	–0.0844	–26.1767
4	–0.1592	0.7292	–21.8583	–0.2894	0.2834	–13.0251
5	0.0796	–0.4157	–70.4056	0.3796	–0.1780	20.6356
6	0.0531	0.0865	58.4887	–0.2894	0.0501	–9.8199

4 CONCLUSIONS

FIR filter design methodology is used to design optical filter with a structure of chain birefringent filters. From the mathematical model and the design algorithms we have designed two different optical birefringent filters capable of producing two arbitrarily specified spectral outputs. It is expected that if we increase the numbers of retarders then the transmitted spectrum will be more perfect saw-tooth and flat top profiles. The procedure can be extended to design any arbitrary spectrum which can be of great value in practical use.

5 REFERENCES

[1] Šolc, I., "Birefringent chain filters," J. Opt. Soc. Am 55(6), 621-625 (1965).

[2] Liang, Z. X., Li, G. H., Shao, W. D., and Wang, X., "Study of optimal thickness ratio of birefringent crystals," Chin. J. Lasers 27(7), 601-605 (2000).

[3] Lyot, B., "Un monochromateur à grand champ utilisant les interférences en lumière polarisée," C. R. Acad. Sci. (Paris) 197, 1593-1595 (1933).

[4] Šolc, I., "A new kind of double refracting filter," Czech. J. Phys 4(1), 53-66 (1954).

[5] Chen, C-T, [Digital Signal Processing Spectral Computation and Filter Design], Oxford University Press, New York, 295-297 (2001).

[6] Harris, S. E., Ammann, E. O., and Chang, I. C., "Optical network synthesis using birefringent crystals. I. Synthesis of lossless networks of equal-length crystals," J. Opt. Soc. Am 54(10), 1267-1279 (1964).

[7] Sharp, G. D., and Birge, J. R., "Retard stack technology for color manipulation", SID Symp. 30, 1072-1075 (1999).

Design and Development of Long Wave Pass Filter

MD. Nasheer*, S. Ramakrishna, N.J. Babu.
Hind High Vacuum Co.Pvt.Ltd, Phase I, Peenya Industrial Area, Bangalore-560058

ABSTRACT

In this work, design and development of Long Wave Pass Filter (LWPF) with tight edge tolerance of ± 2 nm has been demonstrated. These type of filters demands the use of multilayer designs with thicknesses which bear no relation from one to other. Error analysis study of the designs shows that each individual layer thickness needs to be controlled with in 1% of its original thickness to attain the tight edge tolerance and repeatability of the coatings. For this reason, these coatings have been executed using optical monitor with level monitoring technique.

Keywords: Long Wave Pass Filter, QWOT, Optical thickness monitor, level monitoring.

1. INTRODUCTION

Long Wave Pass Filters aimed at achieving > 90% transmission in the pass band and < 1% transmission in rejection region with cut on wavelength λ_c at 450nm. Cut on wavelength λ_c defined as wavelength at 50% of peak transmission. LWPS finds many applications in bio-metric scanners, fluorescence imaging, gas detectors and blocking filters for narrow band filters etc. These applications demands long wave pass filters to have tight edge tolerance in addition to high transmission in the pass band and high reflection in the rejection band. Conventional electron beam deposition with crystal monitoring possesses issues like high thickness errors and absorbing films resulting low transmission in the pass band and edge wavelength inconsistency. To overcome this problem, Ion assisted deposition is used to achieve near bulk material index and optical monitoring is used to get high precision cut-off of each individual layers.

2. DESIGN

Essential Macleod thin film software has been used to design and optimize the thicknesses of layers to meet the spectral performance. Tio2 and Sio2 materials have been used as high and low index alternative layers. Simplex optimization technique was used to optimize the design with targets aiming for λc at 450nm and steep transition from pass band to rejection band

In order to get steep transition from transmission band to rejection band and minimum variation in cut on wavelength LWPF designed with 49 alternative layers of TiO_2 and SiO_2 materials with quarter wave optical thickness (QWOT) on BK 7 glass. Theoretical performance of LWPF with QWOT shown in fig 1.This has kink at cut on wavelength which is not acceptable.

*nasheer@hhv.in, Phone: 0804193 1115/1000; www.hhv.in.

2.1Design Optimization

Simplex optimization technique was used to optimize the design with targets aiming for steep transition from pass band to rejection band. Layers close to air and glass interfaces optimized to obtain precise cut on wavelength, high transmission and rejection in separate spectral regions and it resulted in thicknesses which bear no relation from one to other at air and glass interfaces.

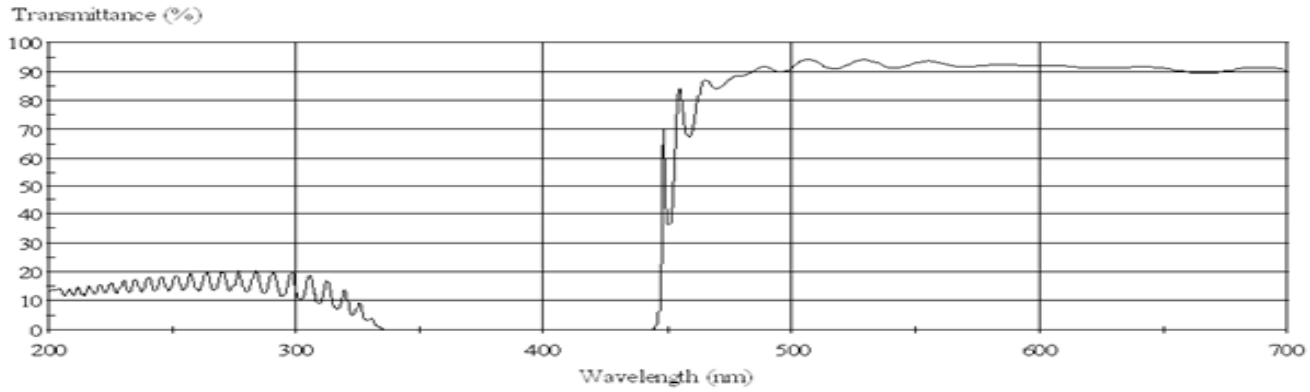

Fig 1: Designed performance of LWPF with QWOT.

The outcome of the optimization is the design consisting of 49 layers which have random optical thickness at air and glass interface. Designed performance of the final design shown in fig 2.

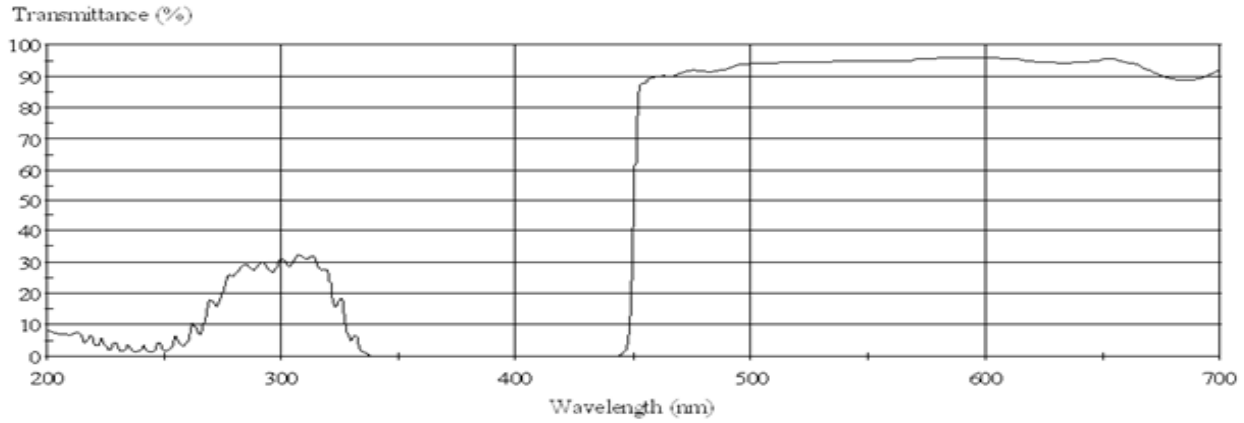

Figure 2: Designed performance of LWPF after optimization.

3. DEPOSITION OF LWPF

3.1 Coating Unit

For the experiment work Box Coater (BC 600) manufactured by Hind High Vacuum has been used. This system equipped with KRI end hall ion source, Telemark Optical thickness monitor, 3KW electron beam gun, Digital thickness monitor, Temperature controller, Mass flow controller and Rotary drive. Ion source used to maintain the stoichiometry of films. Box coater shown in fig 3 with Optical thickness monitor, electron beam gun power supplies. LWPF developed with electron beam ion assisted deposition method. Coating deposition was carried out at 150 °C. Ion gun parameters like ion source voltage and discharge current were fine tuned for minimal absorption and high density in the films. Ion source shown in fig 4 along with EB gun and substrate holder.

Optical thickness monitor used to precisely control layer thickness during execution. Appropriate monitoring wavelength has been selected for proper layer termination to avoid deviation from design values to practical results. As the design contains random layer thicknesses, level monitoring method has been selected.

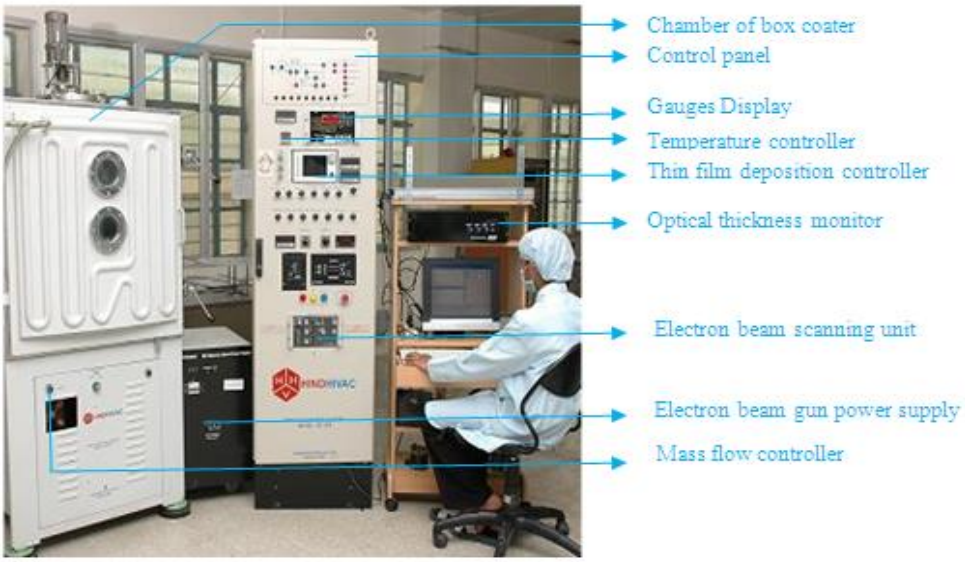

Figure 3: BC-600 Coating unit manufactured by Hind High Vacuum Co. Pvt.Ltd

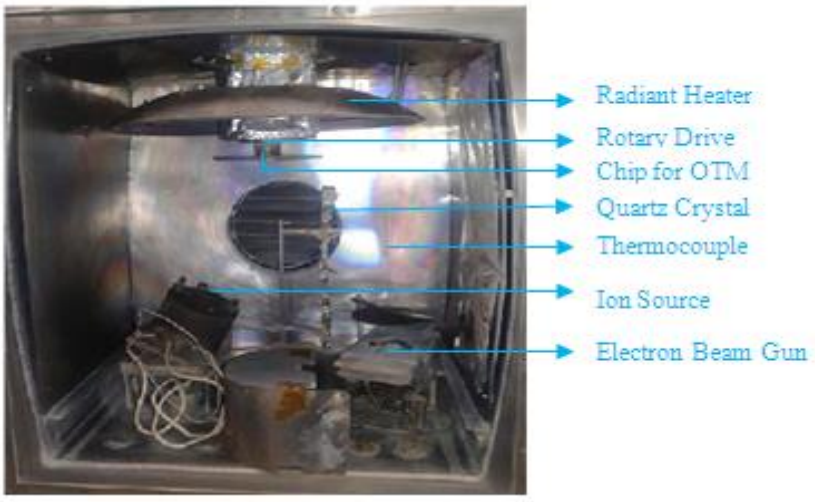

Fig 4: Inner view of Box Coater (BC- 600)

3.2 Level Monitoring

Layer thicknesses have no relation from one to other at boundaries resulted in complex design to execute. Monitoring wavelength chosen to terminate 49 layers using level monitoring method. Layers close to air and glass interface monitored carefully to meet precise cut on wavelength. During coating process maintained deposition parameters such as substrate temperature, deposition rate, partial pressure, Ion source discharge voltage, discharge current, emission current constant from batch to batch to ensure accuracy and reproducibility.

4. RESULTS

The following results shows the results of five consecutive coating runs which falls within in the desired edge wavelength accuracy ± 1 nm at 450nm and transmission, > 90% transmission in pass band and transmission < 1% in rejection region. The precise measurement of the evaluation of optical properties during actual construction of a filter allowed us to control layer thickness with very good accuracy. The spectral performance of LWPF has been measured using Shimadzu 1601 spectrophotometer.

.

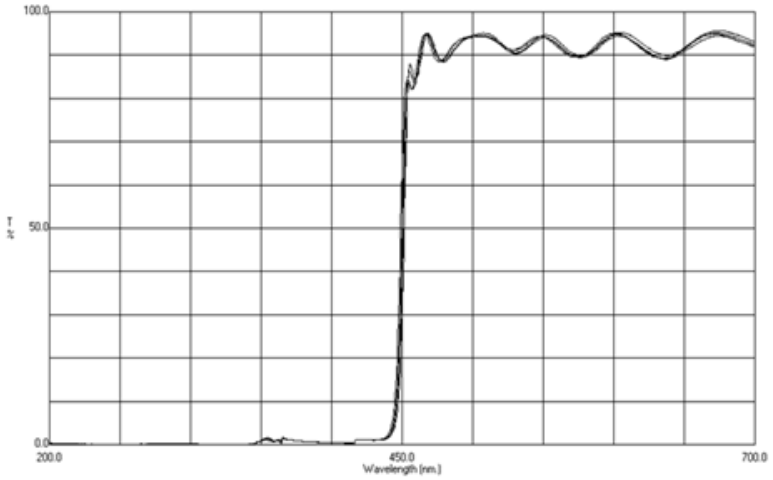

Figure 5: Spectral performance of five consecutive coating runs.

From the above results it is clear that level monitoring gives very good accuracy of the cut on wavelength and high transmission above cut on wavelength. Ripples in the transmission band are due to non-quarter wave optical thicknesses at interfaces.

CONCLUSION

Long Wave Pass Filter has been successfully demonstrated using the level monitoring technique by optical thickness monitor. Further work will be carried out to reduce ripples in the passband.

REFERENCES

[1]. Optical Coating Technology-Philip W Baumeister, SPIE Vol.No.PM137.

[2].Thin Film Optical Filter- H.A. Macleod, 2001.Institute of physics publishing.

[3].Thin Film Design Software-H.A. Macleod.

[4].Practical Design and Development of Optical Thin Film-Ronald.R.Wiley.

Larger Core Diameter Alternative to Single-mode Fiber

H. Mohapatra*[1] and S. I. Hosain[2]

[1]*Department of Physics, C. V. Raman College of Engineering, Janla, Bhubaneswar-752054, Odisha, India*
[2]*Department of Physics, Ravenshaw University, Cuttack-753003, Odisha, India*

ABSTRACT

An optical fiber, supporting first four LP modes propagating with zero intermodal dispersion, has been proposed. The refractive index profile of this fiber has power law refractive index variation with more than one profile exponents within the core over different radial distances from the axis. We also observed that the order of appearance of the modes depends on the parameters of this refractive index profile**.**

Key words: Few-mode Fiber, Zero Intermodal Dispersion, Order of Appearance of Modes

1. INTRODUCTION

In the initial stages of development, multimode fibers were used as the transmission medium in an optical telecommunication network because of the ease of coupling LEDs to them. An optical pulse incident at the input end of the fiber excites several modes. These modes propagate through the fiber with different group velocities and hence arrive at the output end of the fiber at different times although these are excited at the same instant of time at the input end. This results in broadening of the pulse which is of the order of ns/km and the phenomenon is known as intermodal dispersion. This limits the information carrying capacity of the system.

**hiranmayee.mohapatra@gmail.com(H. Mohapatra),sih_18@yahoo.co.in(S. I. Hosain)*

Intermodal dispersion is eliminated by using single-mode fibers which support only one mode (fundamental mode) in it. Single mode fibers were introduced in the later half of 1970s and are still in use. Due to smallness of core diameter (5-10μm), the splicing of two single mode fibers posed a big problem in those days. To overcome this difficulty, in the later half of 1970s and first half of 1980s, researchers suggested dual-mode fiber as a better alternative to single-mode fibers [1-3]. In a dual mode fiber the fundamental (LP_{01}) mode and the first higher order (LP_{11}) mode were allowed to propagate with the same group velocity by appropriately tailoring the fiber parameters. The core diameter of the dual-mode fiber would be obviously larger than that of the single-mode fiber as two modes propagate. However, with subsequent development of fusion splicing technique, the splicing of two single-mode fibers was no more a problem. Thus, research on dual-mode fibers was eventually discontinued.

Interest has again grown in the study of few-mode fibers (FMFs), particularly in astronomical telescopes [4], for dispersion tailoring [5] and for dispersion compensation [6]. A recent work by Yaman et al. [7] on long distance transmission using few-mode fiber utilises single-mode operation of few-mode fibers with negligible mode coupling in which the entire data is transmitted in the fundamental mode. In such fibers first few modes are allowed to propagate. An FMF can replace single mode fiber as transmission medium provided that it is made intermodal dispersion free. Investigating theoretically, we have proposed a refractive index profile for which the group velocities of the first four (LP_{01}, LP_{11}, LP_{02} and LP_{21}) modes are equal at an optimum set of values of the profile parameters and dimensionless frequency (or V number) of the fiber. This profile has power law refractive index variation with more than one profile exponent within the core over different radial distances from the axis. This optimum V-value should be less than the cut-off V-value of the fifth mode, which is true in our case. Hence knowledge of cut-off V-values of the various LP modes for this profile is very much essential so that one can easily know which one is the fifth mode. Using a numerical method developed by us, we have computed the cut-off V-values of the first 10 LP modes. While doing so, we have observed the interesting result that the order of appearance of LP modes is not unique. An LP mode that appears as the fifth mode for a particular set of parameters of the profile can become the sixth mode for a different set of values of the parameters of the same profile. The theory is briefly discussed in section 2 and the results and discussions are presented in section 3. Concluding remarks are presented in section 4.

2. THEORY

The refractive index profile proposed by us has the following expression:

$$n^2(R) = n_1^2 [1 - \delta f(R)] \qquad R \le 1$$
$$= n_1^2 [1 - \delta] = n_2^2 \qquad R > 1 \tag{1}$$

where

$$f(R) = (R/s_1)^{q_1} \qquad 0 \le R \le c$$
$$= R^{q_2} \qquad c \le R \le 1 \tag{2}$$

$$R = r/a, \quad c = r_1/a, \quad s_1 = c^{(1 - q_2/q_1)} \quad \delta = (n_1^2 - n_2^2) / n_1^2 \tag{3}$$

We have used the usual cylindrical coordinate system (r, φ, z) with the z-axis coincident with the fiber axis. Here a represents the core radius, R is the normalized radial coordinate, n_1 is the refractive index on the fiber axis and n_2 is the uniform refractive index of the cladding. The parameter c is the normalized boundary of the first annular region and the dimensionless parameter s_1 is obtained by matching the refractive index profile at $R = c$. The parameters q_1 and q_2 are the profile exponents in the two annular regions. This profile may be called as the composite two-q profile.

The normalized group delay of a mode is given by $d/dV(Vb)$, where $V = a.2\pi. (n_1^2 - n_2^2)^{1/2} / \lambda$, b is the usual normalized propagation constant [8] and λ is the free space wavelength. Using our numerical method and an optimization technique, we have obtained an optimum set of values of the profile parameters and V for which the group delays of the first four LP modes become equal. These optimum values are presented in the next section.

3. NUMERICAL RESULTS AND DISCUSSION

These optimum values are q_1=0.51, q_2=2.4099, c=0.7099 and V=6.99. Our calculation shows that the cut-off V values of LP_{21} and LP_{12} modes are respectively V_{21}= 5.8024 and V_{12}=7.5217, LP_{12} being the fifth mode. Thus at the optimum value of V=6.99 the fiber will support these four modes only. We would like to mention here that our fiber is only an intermodal dispersion free four-mode fiber which is equivalent to a larger core diameter single-mode fiber. Considering cladding to be of pure silica, for λ=1.55μm we find a~ 14.22μm for δ=0.007 and a~ 18.84μm for δ=0.004.

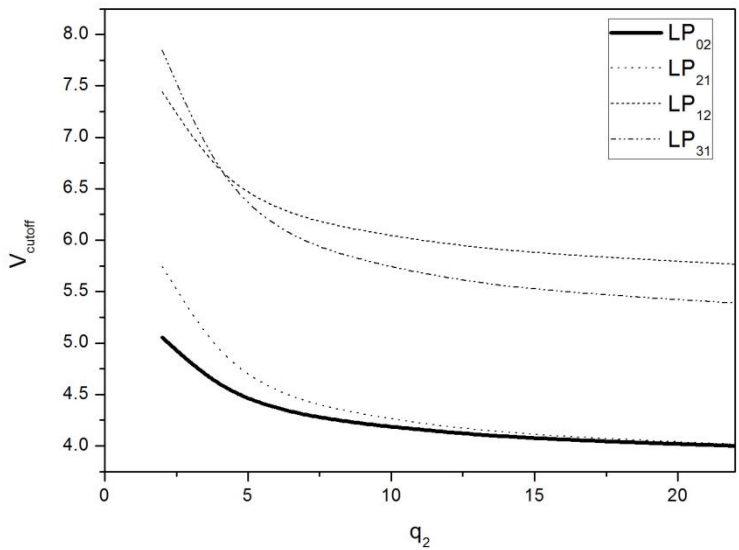

Fig. 1: Cut-off V value as a function of q_2 for q_1=20 and c=0.2 for various LP_{lm} modes

To illustrate how the order of appearance of the modes depends on the profile parameters, in Fig. 1, we have plotted cut-off V values as a function of q_2 for typical values of q_1=20 and c=0.2 for four lower order LP modes namely,LP_{02}, LP_{21}, LP_{12} and LP_{31}. From the figure one observes that for $q_2 < 3.9$, LP_{12} mode appears prior to LP_{31} mode and hence LP_{12} mode is the fifth mode whereas LP_{31} mode is the sixth mode. On the other hand, for $q_2 > 3.9$, LP_{31} mode appears prior to LP_{12} mode and hence LP_{31} mode becomes the fifth mode whereas LP_{12} mode becomes the sixth mode. For our optimum profile we have checked that the LP_{12} is the fifth mode while LP_{21} is the fourth mode. The optimum V-value of 6.99 lies between the cut-off V values of LP_{21} and LP_{12} modes. Our investigation for other higher order modes with an explanation of this behaviour using symmetry property of the modes is under progress and will be reported elsewhere in future.

4. CONCLUSION

An intermodal dispersion free optical fiber has been proposed in which the first four modes (LP_{01}, LP_{11}, LP_{02} and LP_{21}) propagate with the same group velocity. The refractive index profile has power law variations with different profile exponents over different annular regions. The dependence of the order of appearance of the LP modes on the profile parameters has also been discussed.

REFERENCES

[1] Cohen, L. G., Mammel, W. L., Lin, C. And French, W. G., "Propagation characteristics of double mode fibers," Bell System Technical J. 59(6), 1061-1072 (1980).

[2] Sakai, J., I. and Kimura, T., "Large-core, broadband Optical fiber," Opt. Letters 1(5), 169-171 (1977).

[3] Hosain, S. I., Sharma, E. K., Sharma, A. and Ghatak, A. K., "Analytical approximations for the propagation characteristics of dual-mode fibers," IEEE J. Quantum Electron. QE-19(1), 15-21(1983).

[4] Corbett, J. C. W., "Sampling of the telescope image plane using single and few mode fiber arrays," Opt. Express, 17(3), 1885-1900 (2009).

[5] Ramachandran, S., "Dispersion Tailored Few-Mode Fibers: A Versatile Platform for In-Fiber Photonic Devices," J. Lightwave Technol., 23(11), 3426-3443 (2005).

[6] Ramachandran, S., Ghalmi, S., Chandrasekhar, S., Ryazanshy, I., Yan, M., F., Dimarcello, F., V., Reed, W., A. and Wisk, P., "Tunable dispersion compensators utilizing higher order mode fibers," IEEE Photonics Technol. Letters, 15(5) , 727-729, (2003)

[7] Yaman, F., Bai, N., Zhu, B., Wang, T. and Li, G., "Long distance transmission in few mode fibers,"Opt. Express, 18(12), 13250-13257, (2010).

[8] Ghatak, A. and Thygarajan, K., Cambridge University press, Cambridge, UK, (2002).

Development of a scalable generic platform for adaptive optics real time control

Avinash Surendran[a], Mahesh P. Burse[b], A. N. Ramaprakash[b], Padmakar Parihar[a]

[a]Indian Institute of Astrophysics, Koramangala 2nd Block, Bangalore - 560034, India
[b]Inter-University Centre for Astronomy and Astrophysics, No. 4, Ganeshkhind, Pune University Campus, Pune - 411007, India

ABSTRACT

The main objective of the present project is to explore the viability of an adaptive optics control system based exclusively on Field Programmable Gate Arrays (FPGAs), making strong use of their parallel processing capability. In an Adaptive Optics (AO) system, the generation of the Deformable Mirror (DM) control voltages from the Wavefront Sensor (WFS) measurements is usually through the multiplication of the wavefront slopes with a predetermined reconstructor matrix. The ability to access several hundred hard multipliers and memories concurrently in an FPGA allows performance far beyond that of a modern CPU or GPU for tasks with a well defined structure such as Adaptive Optics control. The target of the current project is to generate a signal for a real time wavefront correction, from the signals coming from a Wavefront Sensor, wherein the system would be flexible to accommodate all the current Wavefront Sensing techniques and also the different methods which are used for wavefront compensation. The system should also accommodate for different data transmission protocols (like Ethernet, USB, IEEE 1394 etc.) for transmitting data to and from the FPGA device, thus providing a more flexible platform for Adaptive Optics control. Preliminary simulation results for the formulation of the platform, and a design of a fully scalable slope computer is presented.

Keywords: FPGA, Adaptive Optics, ELT

1. INTRODUCTION

The technology of AO is used to correct the fast-changing blurring caused by the Earth's atmosphere in real time. The most distinctive components of an adaptive optics system are: the DM which dynamically corrects for the optical aberrations of the incoming signal; the WFS which measures the shape of the instantaneous wavefront distortions due to atmospheric turbulence; and the control system which interfaces both the DM and WFS to correct for atmospheric turbulence at a high frequency. The technique is now helping astronomers attain near-diffraction limited resolution images at IR wavelengths with the largest existing telescopes, without the cost and difficulty associated with sending them to space. The landscape of adaptive optics has reached a level which demands abstraction of its core functions, where a large part of the computational algorithms used for AO control are common irrespective of the telescope that they are used on. With the advent of extremely large telescopes (30 m – 100 m), we find the need for incorporating AO as an indispensable part of these telescopes. Hence, there needs to be a way to implement the same with a minimal development overhead and with a great flexibility of wavefront sensing and correction resources. The Thirty Meter Telescope would pave the way as the first telescope designed with AO as an integral system element.[1]

The most computationally intensive processes for an AO system are slope computation and phase reconstruction. For a standard least-squares reconstructor algorithm, the computational complexity scales as FLOPS $\sim D^4$ most of which is contributed by full matrix-multiply operations.[2] For e.g., extreme-AO on TMT would require 10^5 times the processing power of the current Keck AO system.[3] This level of parallelism and high performance computing requirement of AO have conventionally been implemented with GPUs[4] (Graphical Processing Units), and multi-core CPUs.[1] FPGAs are semiconductor devices that are based around a matrix of configurable logic blocks (units of logic gates and flip-flops) connected via programmable interconnects, and can be reprogrammed

Further author information: (Send correspondence to A.S.)
A.S.: E-mail: asurendran@iiap.res.in

to implemement any digital design. The FPGA leads in the ability to easily interface high speed I/O and a reduced memory latency but it is slower at floating point operations compared to the GPU.[5] We need to explore FPGAs as a viable alternative to GPUs and multi-core CPUs in providing increased system performance at lower costs and a better power efficiency for industrial adaptive optics systems. The use of FPGAs for the next generation of high-end ground based telescope AO controllers has already been explored by a number of researchers,[6–8] but a truly scalable and generic platform still doesn't exist.

In Section 2, we show the requirements of the Real Time Controller (RTC) and the rationale behind choosing them. In Section 3, we present the implementation of a fully scalable wavefront processing unit (WPU). In Section 4, we present the results including the logic resources and the timing summary.

2. RTC REQUIREMENTS AND CHALLENGES

The key requirements of the RTC are as follows:

1. To create a generic platform for adaptive optics, which can incorporate current and future wavefront sensing and correction techniques through abstraction of the wavefront sensing and correction geometries, as described by Southwell.[9]
2. To incorporate the flexibility of different I/O protocols for wavefront sensing, correction and telemetry into the FPGA module.
3. To make it scalable to fulfill short term requirements of flexibility in telescope mirror size, atmospheric conditions, the frame rate of acquisition, and the number and nature of guide stars used.

2.1 Error Budgets

We have set a target Strehl ratio of 0.5 at a wavelength of 1 μm owing to the extreme AO capability that would be required for the next generation of Extra Large Telescopes (ELTs) and the limitations of error budgets that can be achieved with current technology. A Strehl ratio of 0.5 corresponds to a total RMS wavefront error (WFE) of about 130 nm at a wavelength of 1 μm, according to Marechal approximation.[2] The degrees of freedom (DOF) of an AO system is determined by the the spatial resolution of wavefront detection and correction, and thus directly contributes to the fitting error.[10] A 10,000 DOF system translates to a fitting error of 64 nm for a 30 m telescope, which is an acceptable limit for achieving the required Strehl ratio.

2.2 Interface Control Requirements

The function of the WPU is mainly pixel acquisition and slope computation. It should also have the capability for preliminary image processing of the RAW CCD frame including (but not limited to) dark subtraction, flat fielding and background correction. The WPU is initially assumed to be able to interface to a Shack-Hartmann (SH) sensor which uses Fried geometry.[11] The error budget is used to derive the WPU interfacing requirements which are enumerated as follows:

1. It should be able to interface four WFS CCDs of size 512 x 512 pixels at 16-bit/pixel, through a maximum of a total of 16 fibre channels.
2. It should be able to read out an entire CCD frame in 0.5 ms.
3. Pixels per subaperture should be flexible anywhere between 2 x 2 to 8 x 8 pixels.

The above requirements translate to a memory bandwidth of 256 MB/s for a single fiber channel, which in turn leads to a requirement of 1 GB/s for a single CCD through 4 fibre channels and 4 GB/s for 4 CCDs through 16 fibre channels.

2.3 AO Reconstructor Requirements

Zonal reconstruction using a conventional Matrix Vector Multiply (MVM) operation will be initially adopted for its simplicity and scalability.[12] If we assume a sensor size of 512 x 512 pixels with each subaperture consisting of 4 x 4 pixels, the number of slopes along a single spatial dimension is 128 and the number of WF slopes generated by a single sensor would be 32,768. For a single conjugate AO (SCAO) system, the size of the reconstruction matrix would be 32,768-by-16,641, where 16,641 is the number of actuators of the DM without any form of phase interpolation. If we assume that each element of the reconstruction matrix can be represented in 2 byte fixed-point format, it would occupy 1 GB. For a Multi-Conjugate AO (MCAO) system with 4 sensors, it would scale up to a 131,072-by-16,641 matrix which would occupy 4 GB. An AO control loop frequency of 800 Hz would require a computational power of 3.48 TFlops for AO reconstruction. The memory bandwidth would heavily depend on the hardware used and the method of implementation.

3. IMPLEMENTATION OF A SCALABLE WPU

3.1 MATLAB AO Simulator

A basic scalable SCAO simulator was made using MATLAB wherein one could change the number of subapertures and the pixels per subaperture of a basic SH (Shack-Hartmann) sensor in a Fried geometry configuration. It is coupled with a test-bench where the Von-Karmann phase screen could be generated with atmospheric input parameters including but not limited to Fried parameter, aperture diameter, the inner and outer scales of turbulence etc. The phase screen generation can be scaled upto very large aperture diameters and is based on the work by Sedmak.[13] Testing of all slope computation and AO reconstruction algorithms is done on this simulator before implementation on an FPGA.

3.2 Test Platform

The Xilinx VC-709 Connectivity Board[14] is chosen as the test platform mainly owing to the powerful Virtex-7 XC7VX690T FPGA coupled with the ability of flexible and fast hardware interfacing options like multiple small form-factor pluggable (SFP) transceiver ports, Peripheral Component Interconnect Express (PCIe) 3.0 x8, FPGA Mezzanine Connector (FMC) and 2 banks of 4 GB DDR3-1866 memory modules.

3.3 Objectives

The first step is to design a fast pixel acquisition platform coupled with a pipelined and fully scalable slope computer for an SH sensor. The WPU is designed based on the following assumptions:

1. The platform should support a full-frame readout time of 0.5 ms for a 4-quadrant 512 x 512 pixel CCD (from Section 2.2), which translates to a pixel clock period of 7.629 ns, or a clock frequency of 131.072 MHz.
2. The architecture should be scalable with respect to the number of subapertures and the pixels per subaperture, and be modular for testing different slope computation algorithms.
3. A similarly scalable VHDL test-bench should be linked with MATLAB AO simulator for quick troubleshooting and validation.

3.4 Implementation

3.4.1 Dataflow

A combination of Dual-port Block RAM (BRAM), Finite State Machine (FSM) design and clock management techniques are used to implement a fast, scalable and efficient WPU. For slope computation, we use a conventional Centre of Gravity (CoG) algorithm[10] for the sake of demonstration. Division essentially consists of repeated subtraction, and hence the CoG takes a large datapath delay. The design is divided into two clock domains, one for fast pixel acquisition which runs at the CCD pixel clock frequency and the other for slope computation which runs at $\frac{1}{16}$th the frequency of the pixel clock. The BRAM is used to isolate the 2 clock domains as shown in Figure 1. The 'Input Addressing and Chip Select' unit identifies the pixel location in the CCD and generates

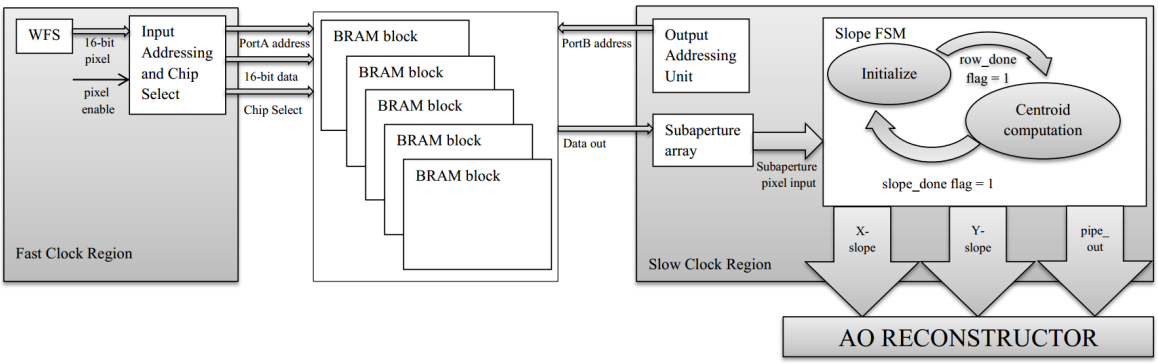

Figure 1. WPU Dataflow

the address and BRAM block to be selected where the pixel is to be stored. The pixel acquisition unit can work at a maximum frequency of 131.072 MHz.

The state of any FSM is decided by its current state and any input variables associated with it. The slope FSM starts at the 'Initialize' state and waits till enough pixel data is available in the BRAM for slope computation. When the last pixel of a particular row of subapertures is read out into the BRAM, enough information is available to commence slope computation and the state of the FSM changes to 'Centroid Computation'. The number of x-slopes and y-slopes which are available at the output at every clock cycle depends on the value of a user-defined parameter called 'iter'. A larger 'iter' translates to a faster slope computation at the expense of the FPGA logic resources. 'pipe_out' gives the information of the number of slopes that have already been computed, to the AO reconstructor. Both the pixel acquisition and slope computation occur in parallel without one affecting the performance of the other. The FSM can be operated at a maximum frequency of around 10 MHz.

3.4.2 BRAM configuration example

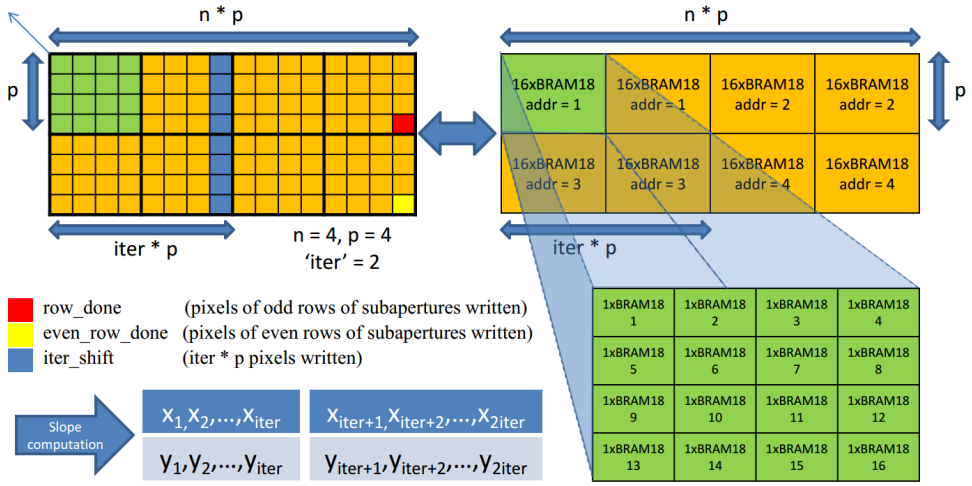

Figure 2. BRAM Configuration example. n is the number of subapertures, p is the pixels per subaperture and iter is the number of slopes which are computed per clock cycle.

BRAM36 is a BRAM primitive present in the Virtex-7 series of FPGAs and can be divided into two BRAM18 primitives. It has a 32-bit datawidth with one block being able to store 1K datawords. In the example shown in Figure 2, the number of subapertures along a row (n) is set to 4, the pixels per subaperture along a row (p) is set to 4 and the slopes to be computed per clock cycle (iter) is set to 2. The pixels of every 'iter' subapertures

are stored in different BRAM blocks as all the associated pixels need to be concurrently accessed for slope computation in a single clock cycle. The pixels associated with the first two (as iter = 2) subapertures are stored in the first address of different BRAMs for concurrent access. The pixels of the third and fourth subaperture are stored in the second address of the same set of BRAM blocks, and the pattern continues for two rows of subapertures. When the slope is being computed for one row of subapertures, the pixels of the next row of subapertures will be written into the BRAM. Hence, memory access for the pixels of two rows of subapertures are required at a time as shown in Figure 2. The flag, 'row_done' signifies the end of each row of subapertures and triggers the FSM to start centroid computation. 'even_row_done' signifies the completion of readout of the pixels of an even number of subapertures and resets the addressing logic.

4. RESULTS AND CONCLUSION

The final slope computer is fully scalable with respect to the number of subapertures (n), pixels per subaperture (p) and the slopes to be computed per clock cycle of the FSM (iter). The architecture is modular, wherein the CoG algorithm can be replaced by any other slope computation algorithm with negligible programming effort. The slopes are obtained in a binary fixed-point format with 8 decimal places. The difference in accuracy when the decimal accuracy was increased to 16 decimal places was found to be negligible in AO reconstruction, using the MATLAB AO simulator. The simulated output of the WPU was compared with the results from the MATLAB AO simulator and they agreed to the 8th binary decimal place, as expected. From Table 1 and Table 2, we can see that the logic resource usage is independent of the number of subapertures (n). It only depends on the pixels per subaperture (p) and the slopes to be computed per clock cycle (iter). We can also conclude that the WPU design is meeting the logic resource limits and timing requirements, and is feasible to be implemented on the Xilinx VC-709 Connectivity Board. The same platform can also be implemented on cheaper Xilinx FPGAs with minimal changes, and can be used in small scale AO for telescopes having an aperture diameter of 2 – 4 m.

n	p	iter	Slice Registers	Slice LUT	BRAM36	WNS (ns)	DSP	FPGA utilization
32	4	16	650	40010	128	1.078	128	11%
		8	345	19837	64	1.3	64	5.40%
		4	194	9423	32	2.272	32	2.60%
32	8	16	1510	98378	512	0.626	128	27%
		8	797	48852	256	0.821	64	13.80%
		4	420	24718	128	1.279	32	7%
64	4	32	1269	79698	256	0.336	256	22%
		16	658	39903	128	1.198	128	11%
		8	349	19942	64	0.791	64	5.50%
64	8	32	2985	195959	1024	0.24	256	55%
		16	1541	97978	512	0.641	128	28%
		8	816	49005	256	0.896	64	13.80%
Total FPGA resources			866400	433200	1470		3600	

Table 1. FPGA resource usage and timing summary in terms of Worst Negative Slack (WNS) for the WPU interfaced to a single channel CCD. n is the number of subapertures, p is the pixels per subaperture and iter is the number of slopes which are computed per clock cycle.

n	p	iter	Slice Registers	Slice LUT	BRAM36	DSP	FPGA Utilization
64	4	16	2632	177475	512	512	45%
		8	1396	80172	256	256	22.20%
Total FPGA resources			866400	433200	1470	3600	

Table 2. FPGA resource usage for the WPU interfaced to a four channel CCD. n is the number of subapertures, p is the pixels per subaperture and iter is the number of slopes which are computed per clock cycle.

REFERENCES

1. G. Herriot, D. Andersen, J. Atwood, C. Boyer, P. Byrnes, K. Caputa, B. Ellerbroek, L. Gilles, A. Hill, Z. Ljusic, J. Pazder, M. Rosensteiner, M. Smith, P. Spano, K. Szeto, J.-P. Véran, I. Wevers, L. Wang, and R. Wooff, "NFIRAOS: first facility AO system for the Thirty Meter Telescope," in *Society of Photo-Optical Instrumentation Engineers (SPIE) Conference Series*, *Society of Photo-Optical Instrumentation Engineers (SPIE) Conference Series* **9148**, p. 10, July 2014.
2. D. T. Gavel, "Adaptive optics control strategies for extremely large telescopes," in *Adaptive Optics Systems and Technology II*, R. K. Tyson, D. Bonaccini, and M. C. Roggemann, eds., *Society of Photo-Optical Instrumentation Engineers (SPIE) Conference Series* **4494**, pp. 215–220, Feb. 2002.
3. P. L. Wizinowich, D. Le Mignant, A. H. Bouchez, R. D. Campbell, J. C. Y. Chin, A. R. Contos, M. A. van Dam, S. K. Hartman, E. M. Johansson, R. E. Lafon, H. Lewis, P. J. Stomski, D. M. Summers, C. G. Brown, P. M. Danforth, C. E. Max, and D. M. Pennington, "The W. M. Keck Observatory Laser Guide Star Adaptive Optics System: Overview," PASP **118**, pp. 297–309, Feb. 2006.
4. L. Wang and B. Ellerbroek, "Computer simulations and real-time control of ELT AO systems using graphical processing units," in *Society of Photo-Optical Instrumentation Engineers (SPIE) Conference Series*, *Society of Photo-Optical Instrumentation Engineers (SPIE) Conference Series* **8447**, p. 23, July 2012.
5. U. I. Minhas, S. Bayliss, and G. A. Constantinides, "GPU vs FPGA: A comparative analysis for non-standard precision," in *Reconfigurable Computing: Architectures, Tools, and Applications*, pp. 298–305, Springer, 2014.
6. A. G. Basden and R. M. Myers, "The Durham adaptive optics real-time controller: capability and Extremely Large Telescope suitability," MNRAS **424**, pp. 1483–1494, Aug. 2012.
7. L. R. Ramos, J. D. Garcia, J. P. Meseguer, Y. M. Hernando, and J. R. Ramos, "FPGA-based slope computation for ELTs adaptive optics wavefront sensors," in *SPIE Astronomical Telescopes+ Instrumentation*, pp. 701530–701530, International Society for Optics and Photonics, 2008.
8. H. Zhang, Z. Ljusic, G. Hovey, J.-P. Veran, G. Herriot, and M. Dumas, "A high-performance FPGA platform for adaptive optics real-time control," in *SPIE Astronomical Telescopes+ Instrumentation*, pp. 84472E–84472E, International Society for Optics and Photonics, 2012.
9. W. H. Southwell, "Wave-front estimation from wave-front slope measurements," *JOSA* **70**(8), pp. 998–1006, 1980.
10. F. Roddier, *Adaptive optics in astronomy*, Cambridge university press, 1999.
11. D. L. Fried, "Least-square fitting a wave-front distortion estimate to an array of phase-difference measurements," *JOSA* **67**(3), pp. 370–375, 1977.
12. J. Herrmann, "Least-squares wave front errors of minimum norm," *JOSA* **70**(1), pp. 28–35, 1980.
13. G. Sedmak, "Implementation of fast-fourier-transform-based simulations of extra-large atmospheric phase and scintillation screens," *Applied optics* **43**(23), pp. 4527–4538, 2004.
14. Xilinx, *VC709 Evaluation Board for the Virtex-7 FPGA*, 12 2014. v1.4.

Conical Fresnel Zone Lens for Optical Trapping

A.Vijayakumar[a], Praveen Parthasarathi[b], Shruthi S. Iyengar[b], Rekha Selvan[b], Sharath Ananthamurthy[b], Shanti Bhattacharya[a] and Sarbari Bhattacharya[b]
[a]Centre for NEMS and Nanophotonics, Department of Electrical Engineering, Indian Institute of Technology Madras, Chennai – 600036, India; [b]Department of Physics, Bangalore University, Bangalore – 560056

ABSTRACT

The phase of a negative axicon is combined with that of a Fresnel zone lens (FZL) to obtain an element labelled as conical FZL, which can generate a focused ring pattern at the focal plane of the FZL. The phase integration is achieved by modifying the location and width of zones of FZL in accordance with the phase variation of the negative axicon. The element was designed for a high power laser with a wavelength of 1064 nm, focal length and diameter of conical FZL of 30 mm and 8 mm respectively and for a ring diameter of 50 μm. The element was fabricated using photolithography. The pattern was transferred from the resist layer to the borosilicate glass plates by dry etching to achieve an etch depth of 1064 nm. The etch depth measured using confocal microscope was 1034 nm at the central part and 930 nm for the outermost part of the device with a maximum error of 12.5% at the outermost part and 3% at the central part. The element was used in an optical trapping experiment. The ring pattern generated by the conical FZL was reimaged into the trapping plane using a tightly focusing microscopic objective. Polystyrene beads with diameters of 3 μm were suspended in deionized distilled water at the trapping plane. The element was found to trap multiple particles in to the same trap.

Keywords: Fresnel zone lens, axicon, multiplexing, optical trapping, photolithography, reactive ion etching

1. INRODUCTION

Focused ring patterns are used for many applications like optical trapping[1], corneal surgery[2], micro drilling[3], etc. The scheme employed for the generation of ring pattern varies with the dynamics of the ring pattern required at the application plane. Ref [1] and Ref [3] deals with the generation of a ring pattern with a fixed ring radius while Ref [2] uses a scheme for generation of a ring pattern with variable radius at the application plane. In all the above cases, the optical configuration is bulkier and involves many optical components.

In diffractive optics, it is possible to design multifunctional single elements[4,5]. The generation of a ring pattern by combining a binary axicon with a binary Fresnel zone lens (FZL) has been demonstrated earlier[6]. However, due to the method used to combine the independent elements, the generated element had very fine feature sizes[7] making fabrication difficult. Furthermore the maximum efficiency of this element is only 32%, which is 8% smaller than that of a standard binary diffractive element. In order to overcome the above difficulties, a modified scheme to combine an axicon with a FZL to obtain a conical FZL for the generation of focused ring patterns was proposed[8].

The proof of concept was done by fabrication of the device with a device diameter of 2 mm on an electron beam resist (PMMA) as the optical power of the source is only 2 mW. However for optical trapping applications, the optical power is higher with a magnitude of hundreds of mW. Hence, it is necessary to transfer the pattern from the resist layer to the glass substrate through etching. In most of the reported[9] plasma etching of borosilicate glass, the etching was carried out with constant period (constant aspect ratio) designs like a grating. In this case, the period of the structure varies across the device and so it is difficult to optimize the processes to achieve constant etch depths across the device. In this paper, we discuss the fabrication of a conical FZL on a borosilicate glass using plasma etching. The result of implementation of the device for trapping multiple particles is also presented.

*physics.vijay@gmail.com,

2. DESIGN OF CONICAL FZL

A conical FZL is designed by combining the phase of an axicon with that of an FZL[8]. The optics configuration for generation of ring pattern using a conical FZL is shown in Fig.1 (a) and the profile of the negative axicon is shown in Fig.1 (b) for a radius R of the element and a maximum optical thickness of $X\lambda$.

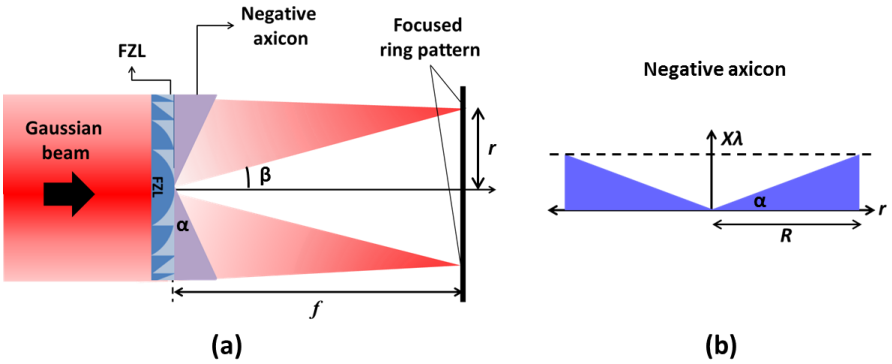

Figure.1 (a) Optics configuration for generation of a focused ring pattern using a Fresnel zone lens and a negative axicon.(b) Profile of a negative axicon with a maximum optical thickness of $X\lambda$ and radius R.

The optical path profile of an axicon is added to the path difference of an FZL as shown in equation (1).

$$\sqrt{f^2+r^2}-f=n\lambda+\left[\frac{X\lambda r}{R}\right], \tag{1}$$

where f is the focal length of the FZL and r is the radial coordinate.

The element was designed for λ = 1064 nm, R = 4 mm, f = 30 mm, radius of ring pattern r_0 = 25 μm and optical power P = 1W. The maximum optical path $X\lambda$ can be calculated from the above values and trigonometry. The radii of zones were calculated for the above design values. The gap between the zones varied from 67 μm to 4 μm across the device.

3. FABRICATION OF CONICAL FZL

The element was fabricated using photolithography as the minimum feature size was > 1 μm. A chromium mask of the pattern was fabricated using Heidelberg Instruments DWL66. S1813 photoresist was used and a borosilicate glass plate was used as substrate. The resist was spin coated to a thickness of 1.5 μm and prebaked at 80 ^{o}C for 17 minutes followed by an exposure in the UV lithography system (λ = 365 nm) for 12 seconds. The post exposure baking was carried out at 90 ^{o}C for duration of 10 minutes. The resist was developed with sodium hydroxide developer and post baked at 120 ^{o}C for > 45 minutes. The baking conditions were optimized to harden the S1813 resist to withstand the etching processes. Wet etching with 10% HF showed poor vertical walls. Hence, the pattern was etched in to the substrate with dry etching.

This etching was carried out using Ar, SF_6 gases with a pressure of 20 mT with a forward power of 200 W and ICP power of 50 W, which resulted in an etch rate of 60 nm/sec. The period of the structure decreased radially outward with the minimum features at the outermost part of the device. The etch rate was higher for larger openings than that for smaller openings. Measurements showed a strong etch depth dependence with feature size and aspect ratio. The etch depth was 1034 nm at the central part and 930 nm for the outermost part of the device with corresponding maximum errors of 3% and 12.5% respectively. The optical microscope images of the central and outermost parts are shown in

Fig. 2 (a) and 2 (c) respectively. The profile of the fabricated structure shown in Fig. 2 (b) and 2 (d) were measured using a confocal microscope. The profile shows reasonable verticality for larger as well as smaller periods.

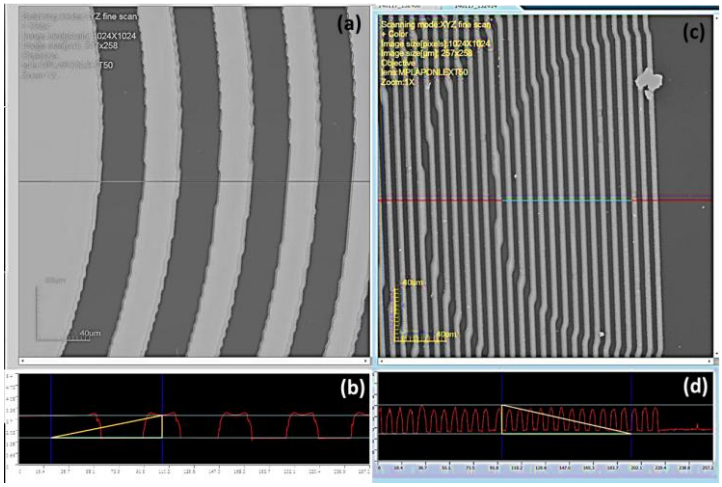

Figure. 2 Optical microscope image of the (a) central part and (c) outermost part of the device. Profile of the (b) central part and (d) outermost part of the device measured using confocal microscope.

4. OPTICAL TRAPPING WITH CONICAL FZL

The configuration for trapping multiple particles in a ring is shown in Fig. 3 (a). The element was introduced in the optical trapping set up[10] as shown in Fig. 3 (b). The ring pattern was reimaged into the trapping plane using a tightly focusing microscopic objective of Numerical Aperture (NA) 1.4. The image of the beam without and with the element is shown in Fig. 3 (c) and (d) respectively.

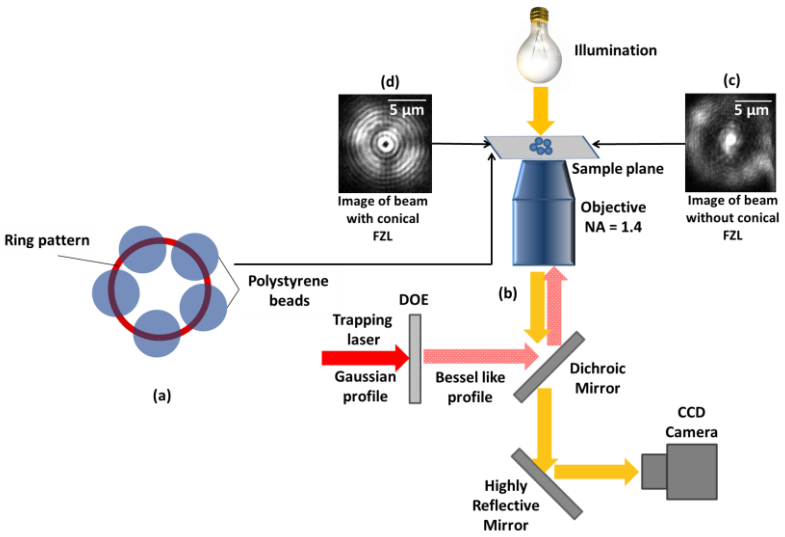

Fig. 3 (a) Schematic of the optical trapping set up with conical FZL. Image of the beam at the trapping plane (b) without conical FZL and (c) with conical FZL

At the focal plane, the spot size was about 1 μm and therefore images of a trapped 3 μm bead with and without the optical element look similar. However, when 1 μm sized beads were used, while a single particle was trapped without the optical element in the path, a cluster of beads were seen to be trapped with the optical element introduced in the path. The trapped 1 μm particles were confined to a region which is about 1-2 μm in size and thus they appeared as a single cluster when imaged. We are currently trying to improve our imaging by adapting a camera of higher resolution and are also trying to image the arrangement of these micro beads as a function of trap geometry by using objectives of different NA values.

5. CONCLUSION

The phase of an axicon is added to the phase of a standard FZL to obtain an element providing annular focus at its focal plane. The single composite element was implemented in an optical trapping experiment to trap multiple particles onto the same trap. The entire process was recorded and these results will be presented. Initial studies are promising and this set-up could potentially be used to understand the interaction between two biomolecules to magnetic nanoparticles.

ACKNOWLEDGEMENTS

The authors thank Center for NEMS and Nanophotonics (CNNP) for the use of their fabrication facilities and the Ministry of Communication and Information Technology (MCIT) for funding this project.

REFERENCES

[1] Halder, A., Pal, S., B., Roy, B., Gupta, D., and Banerjee, A., "Self-assembly of microparticles in stable ring structures in an optical trap," Phys. Rev. A 85**,** 033832 (1-9) (2012).

[2] Ren, Q., and Birngruber, R., "Axicon: a new laser beam delivery system for corneal surgery," IEEE J. Quant. Electron. 26**,** 2305-2308 (1990).

[3] Belanger, P., A., and Rioux, M., "Ring pattern of a ring-axicon doublet illuminated by a Gaussian beam," Appl. Opt. 17, 1080-1086 (1978).

[4] Vijayakumar, A., and Bhattacharya, S., "Design, fabrication, and evaluation of a multilevel spiral-phase Fresnel zone plate for optical trapping: Erratum," Appl. Opt. 52, 1148-1148 (2013).

[5] Vijayakumar, A., and Bhattacharya, S., "Phase-shifted Fresnel axicon: Erratum," Opt. Lett. 38, 458-458 (2013).

[6] Vijayakumar, A., and Bhattacharya, S., "Quasi-achromatic Fresnel zone lens with ring focus," Appl. Opt. 53, 1970-1974 (2014).

[7] Vijayakumar, A., and Bhattacharya, S., "Multi-functional diffractive optical elements,". Proc. SPIE 9194, Laser Beam Shaping XV, 91940Q (September 25, 2014).

[8] Vijayakumar, A., and Bhattacharya, S., "Conical Fresnel zone lenses with ring focus," ICOL 2014, Intl. Conf. on Optics and Optoelectronics, Dehra Dun, India, March 2014.

[9] Parka, J., H., Lee, N.-E., Lee, J., Park, J., S., and Park, H., D., "Deep dry etching of borosilicate glass using SF6 and SF6/Ar inductively coupled plasmas," Microelectron. Eng. 82, 119–128 (2005).

[10] Parthasarathi, P., Nagesh, B., V., Lakkegowda, Y., Iyengar, S., S., Ananthamurthy, S., and Bhattacharya, S., "Orientational dynamics of human red blood cells in an optical trap," J. Biomed. Opt. 18(2):025001-025001 (2013).

Effect of cadmium sulphide nanoparticles on polymer light emitting diodes

P Chandran[1], M Sebastian[1], M A G Namboothiry[2], C P G Vallabhan[1], P Radhakrishnan[1], V P N Nampoori[1,3]

[1]International School of Photonics, Cochin University of Science and Technology, Cochin 682022, Kerala, India;
[2]School of Physics, Indian Institute of Science Education and Research, Thiruvananthapuram 695016, Kerala India;
[3]Department of Optoelectronics, University of Kerala, Thiruvananthapuram 695037, Kerala, India

ABSTRACT

Here we report the effect of cadmium sulphide nanoparticles on different layers of fluorene based polymer light emitting diodes. The hole transporting layer, light emitting polymer and electron injection layer were doped with the nanoparticles, prepared by precipitation technique. The current densities and luminance curves of the LED with respect to bias voltage were compared. We observe that the nanoparticle based devices show improved conductivity, reduced turn on voltage and better luminance performance.

Keywords: cadmium sulphide; nanoparticles; polymer; LED;

1. INTRODUCTION

In the last decade, organic light emitting diodes (OLEDs) have attracted great interest scientifically and commercially and they pose as a potential next generation technology for flat panel displays and lighting systems. OLED prototypes have now been transformed in to marketable products such as mobile phones, digital cameras and televisions. Polymer LEDs in particular, promise potential savings in terms of production cost and energy, because of easy fabrication techniques such as inkjet printing leading to flexible electronics. OLEDs offer numerous advantageous over the conventional inorganic counterpart such as increased brightness, easy fabrication techniques, high yield. However research is still directed towards increasing the stability, lifetime and efficiency of organic light emitting diodes by using multilayer architecture, new active and buffer materials.

Recently, hybrid organic/inorganic light emitting diodes (HLEDs) were demonstrated by employing various metal oxides[1,2] and nanoparticles[3]. Such devices combine the electrical and mechanical stability of conducting oxides/ semiconducting nanoparticles and the processing flexibility of conjugated light emitting polymers (LEP). Air stable electron injection layers have been proposed by incorporating metal-oxides such as titanium dioxide, zinc oxide[4,5], molybdenum oxide. They also offer good mechanical compositional stability and transparency. Quantum dots based HLEDs involving conjugated polymer and luminescent nanocrystals offer advantages like tunable emission, color purity, chemical and optical stabilities and increased luminous efficiency. Increased electrical conductivity has been achieved by doping metal nanoparticles in hole transporting PEDOT:PSS[6-9] (Poly(3,4-ethylenedioxythiophene)-poly(styrenesulfonate)).

Here, we incorporate semiconducting cadmium sulphide (CdS) nanoparticles in different layers of polymer light emitting diode. CdS nanoparticles of size less than 10 nm were synthesized by precipitation technique and were embedded into hole transporting layer, emissive layer and electron injection layer. The HyLEDs show enhanced performance in terms of turn on voltage and brightness.

*chandran@cusat.ac.in; phone +91 0484 2575845; fax +91 0484 2576714; photonics.cusat.edu

2. EXPERIMENTAL

2.1 Materials and Methods

The CdS nanoparticle (NP) was prepared using cadmium acetate and thiourea in the presence of ammonium hydroxide as described elsewhere[10,11]. All polymers and Aluminum used in this study were procured from Sigma Aldrich (USA). The hole transporting PEDOT:PSS (HTL) of 1.3 wt% dispersion in water was used as received without further dilution. The polymer was stirred for 2 hours and filtered using 0.45 μm PVDF syringe filter. The light emitting polymer (LEP) used was a blend of PFO (Poly(9,9-di-n-octylfluorenyl-2,7-diyl)) and F8BT (Poly(9,9-dioctylfluorene-*alt*-benzothiadiazole)) of concentration 15mg/ml in toluene and mixed in a volume ratio of 19:1. Additionally PFN (EIL, poly [(9,9-bis(3'-(N,N-dimethylamino)propyl)-2,7-fluorene)-alt-2,7-(9,9–dioctylfluorene)) was used as electron injection layer dissolving it in methanol at a concentration of 2 mg/ml with a few drops of acetic acid. For nanoparticle:polymer blend, CdS nanoparticles were added to all the polymers at a concentration of 10 mg/ml.

2.2 Device fabrication

The standard device was prepared on a cleaned ITO glass substrate in the following structure, along with the thickness of each layer. The multilayer structure of LED prepared is ITO/PEDOT:PSS (80 nm)/PFO:F8BT (55 nm)/PFN (45 nm)/LiF (2 nm)/Al (100 nm). The ITO glass substrates were cleaned by sonication in various solvents, blowing with N_2 gas and treating with UV/O_3. Here all polymers were filtered using a suitable syringe filter of pore size 0.45 μm prior to spin coating, while Lithium Fluoride and Aluminum were deposited by thermal evaporation. The NP based devices were prepared by replacing the corresponding polymer with their nanoparticle blend.

2.3 Device Characterization

The thickness of polymer layers are measured by optical reflectance system using ThetaMetrsis (FR-pOrtable) The polymer LEDs were characterized by supplying bias voltage and measuring current through the device through Keithley 2000 SMU and simultaneously measuring the luminance using a calibrated photodiode connected to Keithley 2000 digital multimeter. The electroluminescence was measured using Ocean Optics HR4000 spectrometer.

3. RESULTS AND DISCUSSIONS

The current density - bias voltage (J-V) and luminance - bias voltage (L-V) characteristics of all devices are presented in figure 1a and 1b. It can be observed that the CdS nanoparticles enhances the electrical conductivity of the devices and the NP doped in HTL showed maximum conductivity among all the other devices. The turn on voltage of NP doped in HTL decreased by 1.6 V, and in LEP by 1 V, from 6.8 V of that of the standard. However we also perceive from inset on figure 1b, that the maximum luminance decreased by 45% from 1576 cd/m^2 at a typical current density of 56 mA/cm^2. However there is no change in maximum luminance for devices with NP in LEP and EIL, when compared with standard device.

The luminance performance with respect to current density is shown in figure 2a. We see a decreased performance in luminance of NP in HTL device. All other doped devices show no change with the standard device from 0 – 60 mA/cm^2. Beyond the current density of 60 mA/cm^2, all the NP based devices show considerable increase in luminance performance.

The EL spectra of standard device ranges from 500 nm to 600 nm with a dominant peak at 530 nm. The EL spectra for NP in HTL device showed two shoulder peaks at 560 and 580 nm apart from the dominant 530 nm, depicted in figure 2b. The devices with NP in LEP and EIL showed no change from the standard device. Such additional peaks were also observed while incorporating gold nanoparticles in PEDOT:PSS[12]. Comparing the luminance and EL spectra, it is noted that by incorporation of CdS on PEDOT:PSS the full-width half-maximum of the emission spectra is increased by 20 nm with decrease in maximum luminance.

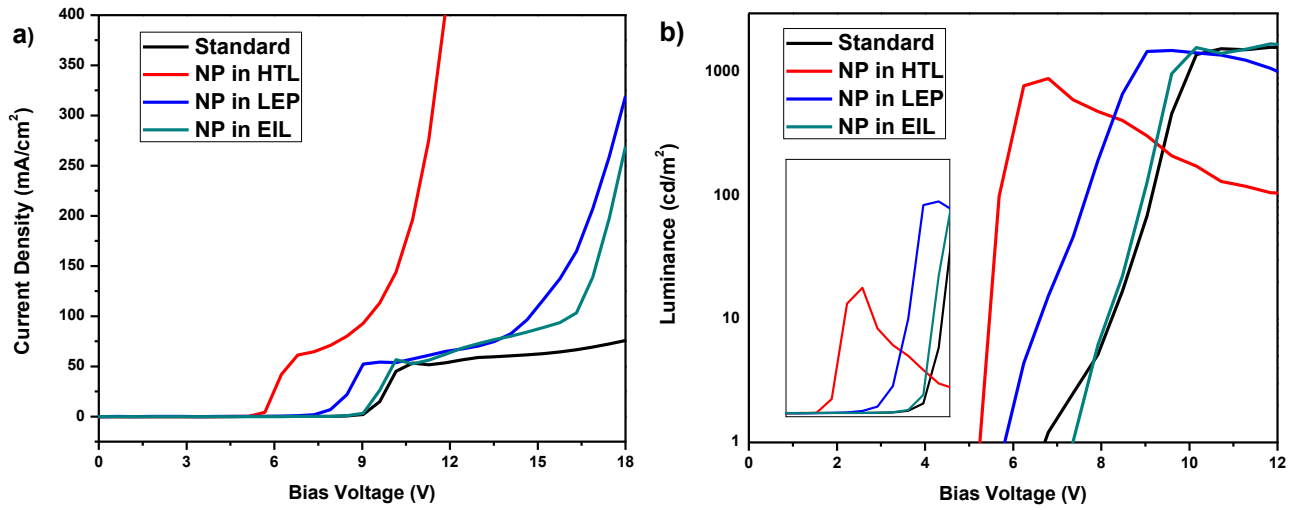

Figure 1: Current density – bias voltage characteristics (a) and Luminance – bias voltage characteristics (b) of nanoparticle based and standard polymer devices. The inset in figure 1b shows the Y-axis in linear scale.

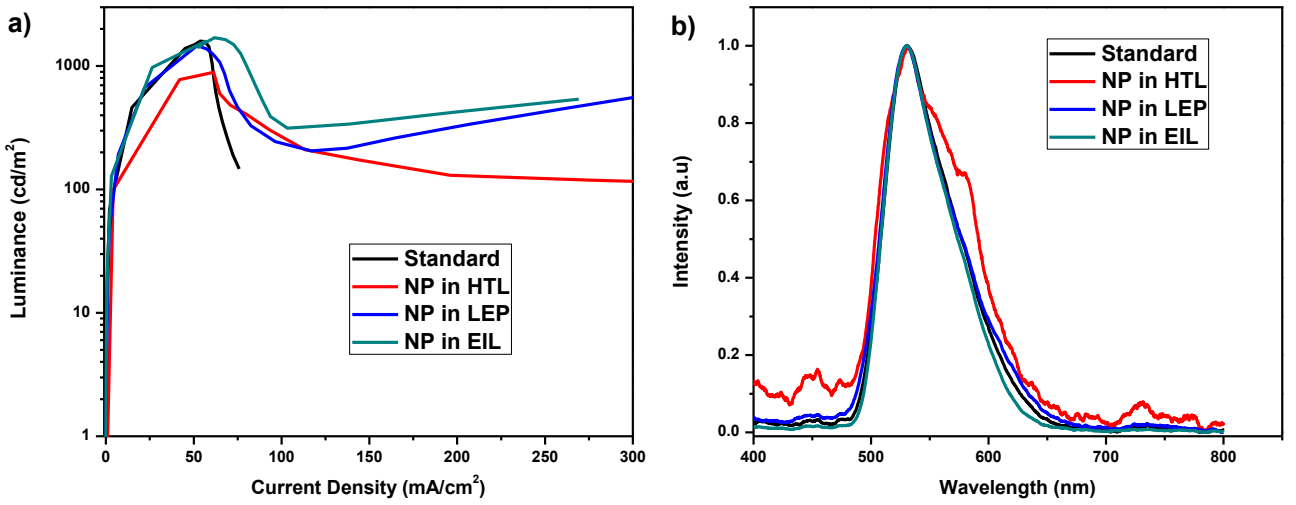

Figure 2: Luminance performance with respect to current density (a) and electroluminescence (b) of nanoparticles based and standard polymer devices

4. CONCLUSION

In summary, we synthesized CdS nanoparticles and incorporated into hole transporting layer (PEDOT:PSS), light emitting polymers (FPO:F8BT) and electron injection layer (PFN). We found increase in conductivity of the device and have a considerable reduction in turn on voltage. The turn on voltage was reduced by 1.6 V when NP was doped in PEDOT:PSS and by 1 V when doped in PFO:F8BT. We also observed that the brightness was reduced by half, in device with NP based HTL along with two additional peaks in electroluminescence spectra. We also observe an increase in the luminance performance of the nanoparticle doped devices over the standard. Further studies such as varying the concentration and size of the nanoparticles will reveal more information related to the effect of nanoparticles in polymer LEDs.

ACKNOWLEDGEMENTS

Authors are thankful to Department of Science and Technology (DST), Government of India for financial support through PURSE program.

REFERENCES

[1] H J Bolink, H Brine, E Coronado, M Sessolo, "Hybrid organic-inorganic light emitting diodes: effect of the meatal oxide", J. Mater. Chem., 2010, 20, 4047 (2010)
[2] M Sessolo, H J Bolink, "Hybrid organic-inorganic light emitting diodes", Adv. Mater., 23, 1829, (2011)
[3] D Shrivastava, M M Malik, "Enhancing efficiency of organic light emitting diodes through doping of cadmium sulphide nanocrystals", Int.J. Nanotechnol Appl., 4, 1, (2014)
[4] H J Bolink, E Coronado, M Sessolo, "White hybrid organic-inorganic light emitting diode using ZnO as the air-stable cathode", Chem. Mater. 21, 439, 2009.
[5] M V M Rao, Y K Su, T Huang, M Tu, S Wu, C Y Huang, "Enhanced performance of polymer light emitting devices using zinc oxide nanoparticle with poly(vinylcarbazole)", J. Electrochem. Soc., 157, H832, (2010)
[6] M Mumtaz, B Ouvrard, L Maillaud, C Labrugere, E Cloutet, H Cramail, M Delville, "Hybrid PEDOT-metal nanoparticles – new substitutes for PEDOT:PSS in electrochromic layers- towards improved performance", Eur. J. Inorg. Chem. 2012, 5360, (2012)
[7] R Pacios, R Marcilla, C Pozo-Gonzalo, J A Pomposo, H Grande, J Aizpurua, D Mecerreyes, "Combined electrochromic and plasmonic optical responses in conducting polymer/metal nanoparticle films", J. Nanosci. Nanotechnol., 7, 2938, (2007)
[8] R G Melendez, K J Moreno, I Moggio, E Arias, A Ponce, I Llanera, S E Moya, "On the influence of silver nanoparticle size in the electrical conductivity of PEDOT:PSS", Mater. Sci. Forum, 644, 85, (2010)
[9] H Choi, S Ko, Y Choi, P Joo, T Kim, B R Lee, J Jung, H J Choi, M Cha, J Jeong, I Hwang, M H Song, B Kim, J Y Kim, "Versatile surface plasmon resonance of carbon-dot-supported silver nanoparticles in polymer optoelectronic devices", Nat. Photon., 7, 732, (2013)
[10] D Lincot, R Ortega-Borges, M Froment, "Epitaxial growth of cadmium sulphide layers on indium phosphide from aqueous ammonia solutions", Appl. Phys. Lett., 64, 569, 1994.
[11] P Raji, C Sanjeeviraja, K Ramachandran, "Thermal propreties of nano crystalline CdS", Cryst. Res. Technol. 39, 617, 2004
[12] Pradeep Chandran, Ramkumar Sekar, Manoj A G Namboothiry, C P G Vallabhan, P Radhakrishnan and V P N Nampoori, "Effect of gold nanoparticles doped PEDOT:PSS in polymer light emitting diodes", Photonics 2014, 12th International Conference on Fiber optics & Photonics, December 13-16, 2014, IIT Kharagpur, India. (post-deadline paper, T3A.84)

Recording of Holographic Multiplex Grating for Beautification

Vadivelan.V[1] and Chandar Shekar. B[2]

[1]Research Scholar, Research and Development Centre, Bharathiar University, Coimbatore – 641046, Tamilnadu, India
[2]Assistant Professor, Nanotechnology lab, Physics Department, KASA, Coimbatore- 641029
vvelan@gmail.com

ABSTRACT

Recorded holographic optical elements by holographic dual - beam multiplexing technology is simple and effective. We created a variety of symmetric patterns in photoresist under controlled exposure sensitivity. Fabricated symmetric structures examined by laser diffraction pattern, Optical Microscope and Scanning Electron Microscope. The repeatable and uniform attractive symmetric patterns in both transmissions as well as reflection direction by illuminating lasers provides an initiation for proto – type product for beautification. Low power laser illuminating symmetric structures are applied for indoor beautification. These periodic symmetric patterns were replicated into metal by electroforming method and it is applied for outdoor illumination by using high power lasers and its diffraction pattern illumination can cover large area.

Holography, Holographic Optical Elements, Periodic Symmetric Patterns, Laser, Diffraction, Beautification, Multiplexing.

1. Introduction

Holography is well known Optical technology applied to record the 3-Dimensional image of the object[1]. At present its usage is unlimited from micro to macro scale, security, product authentication, weapons, communications, displays etc. Nowadays portrait and true color holograms are eye catching and attractive for beautification. Art holograms are recently very famous for display. The light gathering at the recording medium by interference is an interesting technique for recording periodic structures because the interference pattern is three dimensional. Thus, three dimensional structures with comparable to light wavelength known as photonic crystals can be recorded, simultaneously in areas of several square milli – centimetres[2,3]. Holography is one of a promising and inexpensive technique to fabricate large area and defect free periodicity[4]. Dual beam multiple exposure holographic technique is one of a simplest methods for periodicity fabrication compare to three beams, four beams interference and other methods[5]. Two beams interference technique possesses many advantages over the commonly used multiple beam interference technique, such as easy to fabricate different structures and high contrast between the minimal and maximal intensities of interference pattern due to the identical polarization of two laser beams interference area. Recently several groups have employed in this technique[6-8]. Recording and reconstruction of whole information of the objects play an important role in holography for beautification. The three – dimensional image recording in holographic photosensitive material paid great attention for the last few decades[9]. Our positive aim is to utilize the holographic optical elements for beautification. For this, we recorded holographic optical elements in photoresist, we adopt dual beam multiplexing technology and successfully created various symmetric patterns, In particular we used circular symmetric periodic structures for beautification. When this periodic pattern illuminated by 200mW DPSS laser source, we felt that it is like galaxy, after that we decide to use this circular symmetric periodic structures for outdoor and indoor beautification and also we replicated these patterns in metal and polycarbonate by electroforming and recombination methods respectively. Metallic structures applied for high power laser

illumination for large area lighting and replication in polycarbonate is used for indoor light decorating application. Already we have developed prototype products called “Holo-Drizzler” and “Holo- Shower”. In this, we used the recorded periodic structures in photoresist emulsion coated on glass substrate. Our enhanced version of newly developed proto-type product is mainly used metallic and polycarbonate periodic structures for beautifying by its laser diffraction symmetric circular pattern to illuminate the lobby of the hotels, buildings walls, night parties, disco clubs, shopping malls, etc.

2. Theory

When two beams of coherent equally polarized monochromatic optical plane waves of equal intensity intersect with each other, a standing wave pattern will be formed in the region of intersection. The combined intensity distribution forms a set of straight equally spaced bright and dark fringes. Thus holographic photosensitive plate would record a fringe patterns, a sinusoidal varying interference pattern is found at the surface of a substrate placed perpendicular to these planes. Dual beam interference pattern forms a series of straight parallel fringe planes, whose intensity maxima and minima are equally spaced throughout the region of interference. So the plane grating recorded. Multiple - interferences on the same plate with different angular rotation creates overlapping of plane gratings will result different symmetric patterns.

3. Experimental Arrangement

In this experiment, He-Cd continuous wave laser of 100mW power with wavelength 441.6nm from Kimmon is used for main light source for our experiment. Shipley 1500 series photoresist emulsion coated on glass substrate is used to record the holographic multiplex grating. The output narrow laser beam is divided into two by using variable density beam splitter (BS). This beam splitter controls the required beam ratio for optimal recording of gratings in photoresist. These separated two beams are reflected by front coated broad band aluminum mirrors (M1&M2). The mirrors controls the laser beams for desired angle (Θ) at the recording plate. The separated beams are called object and reference beam. These object and reference beams spatially cleaned by using spatial filters (SF1 & SF2). The filtered beams are collimated by using two collimating lenses (L1 & L2). The two beams are interfered at recording plate (PR) with desired angle with equal intensity. We adopt dual beam multiple interference technique in our experiment to create uniform symmetric patterns in holographic plates. The recording plate holder was fixed with rotational stage (PH), this precision control rotational stage is used for many symmetric patterns creation. Uniblitz electronic shutter (ES) controls the exact exposure of laser beam on recording plate. Circular, square and hexagonal symmetric patterns creation depends on number of exposures on holographic plates with desired angular rotation. The detail description of the patterns was explained in the next part. The whole experimental arrangement was placed on the top of vibration free isolation table and is shown in figure 1.

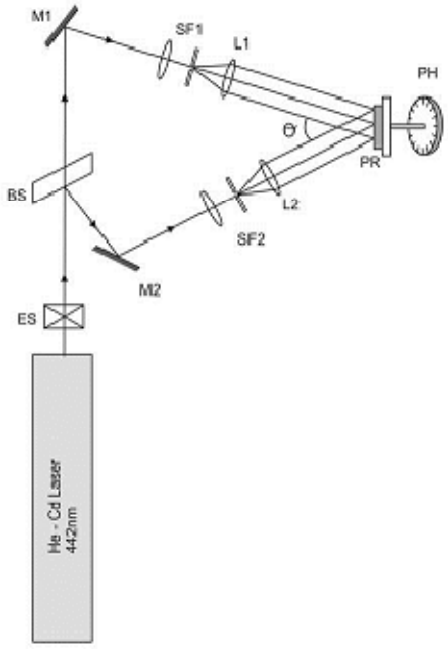

Fig -1: Experimental arrangement for the fabrication of holographic symmetric patterns

4. Result and Discussion

The laser exposure sensitivity was optimized by trial and error method for different periodic symmetries. The optimized exposure sensitivity is in the range of 1200 - 1500μJ/cm^2. The laser exposed multiplex holographic grating in photoresist with optimized power was developed by commercially available developer. During chemical development, photoresist that have been exposed to laser light are dissolved and surface relief pattern is formed. The recorded holograms are shown in Figure - 2.

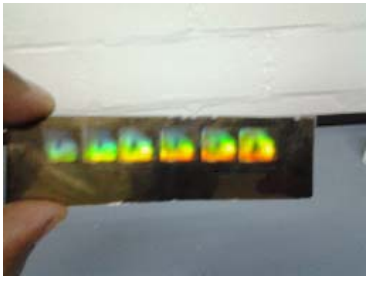

Fig - 2: The recorded multiplexed holographic grating in photoresisit

The recorded hologram reflects and diffracts the incident laser beam into symmetric periodic patterns and is shown in figure 3.

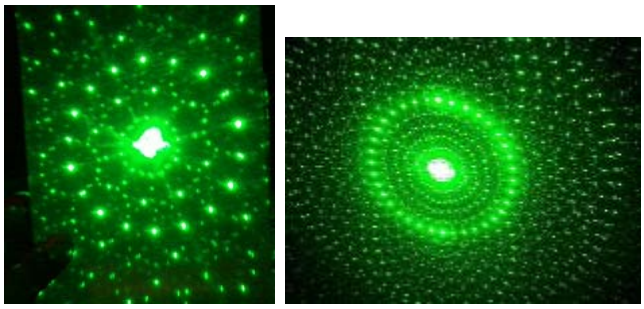

Fig – 3: Laser diffraction pattern of circular periodic symmetry

The periodicity was examined by optical microscope and Scanning Electron Microscope is shown in figure 4.

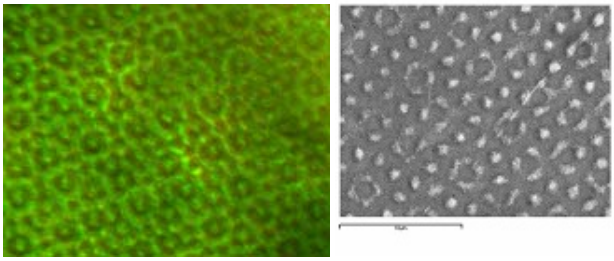

Fig - 4: Optical microscopic and Scanning Electron Microscopic images

Fabricated uniform circular symmetric structures in photoresist is converted into metal through electroforming and the metal hologram for laser high power application for out door illumination is shown in figure 5.

Fig – 5: metal holographic multiplex grating for outdoor beautification

The multiplexed holographic grating in metal is converted into polycarbonate sheet by using heat and pressure and this form was applied for indoor beautification and the proto-type product developed and named as Holo- Shower. The metal holographic multiplex grating is applied for large area outdoor beautification, here we used high power laser soruce for large area coverage and the developed proto-type product called as Holo-Drizzler. Both Holo-Shower and Holo-Drizzler are shown in figure 6.

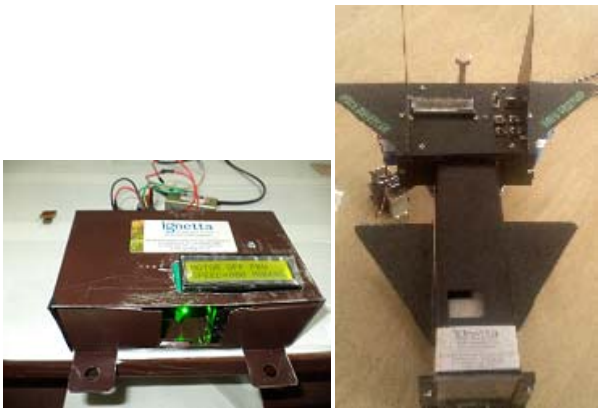

Fig – 6: Proto-type products for beautification

5. Conclusion

The multiplex holographic grating was successfully recorded with controlled exposures for selective periodic structures in photoresist. The fabricated structures are confirmed with laser diffraction, optical microscope and scanning electron microscope. The converted circular symmetric periodic structures in metal and polycarbonate applied for outdoor and indoor beautification.

Acknowledgement

I would like to thank Mr. Thomas Rajan for his encouragement and grant facility to carry this work in Ignetta Holographic (P) Limited.

References

[1]. Saxby, [Practical Holography] Third edition, Institute of Physics Publication, Chapter 16, p 241- 250, (2004)
[2] S. R. J. Brueck, "Optical and Interferometric Lithography Nanotechnology Enablers", Proc. IEEE **93,** 1704 (2005)
[3]. A. Fernandez, J.Y. Decker, S.M. Heran, D.W. Phillion, D.W. Sweeney and M.D. Perry, "Methods for fabricating arrays of holes using interference lithography," J. Vac. Sci. Technol. B15, 2439-2443(1997)
[4]. M. Campbell, D.N Sharp, M.T. Harrison, R.G. Denning and A.J. Tuberfield, "Fabrication of photonic crystals for the visible spectrum by holographic lithography," Nature 404, 53-56 (2000)
[5].N. D. Lai, W. P. Liang, J. H. Lin, C. C. Hsu, and C. H. Lin, "Fabrication of two- and three- dimensional periodic structures by multiple – exposure of two beam interference technique" Optics Express Vol. 13, No.23, (2005)
[6]. S. C. Kitson, W.L. Barnes, J.R. Sambles, "The fabrication of submicron hexagonal arrays using multiple – exposure optical interferometry," IEEE Photon. Technol. Lett. 8, 1662-1664(1996)
[7]. L. Pang, W. Nakagawa, Y. Fainman, "Fabrication of two – dimensional photonic crystals with controlled defects by use of multiple exposures and direct write," Appl. Opt. 42, 5450-5456 (2003)
[8]. N.D. Lai, W.P. Liang, J.H. Lin, C.C. Hsu, " Rapid fabrication of large- area periodic structures containing well-defined defects by combining holography and mask techniques." Opt. Express 13, 5331-5337 (2005)
[9]. G Schmal and D. Rudolph "Holographic diffraction gratings" In progress in optics, 1976, 14, pp- 197.

Acknowledgement

I would like to thank Mr. Thomas Rajan for his encouragement and grant facility to carry this work in Ignetta Holographic (P) Limited.

Design and analysis of holographic optical element for daylighting the interiorofbuilding

Rishabh Raj[1*], Rajeev Ranjan[2], and R. Navamathavan[1*]

[1]Division of Physics, School of Advanced Sciences, VIT University Chennai, Vandalur – Kelambakkam Road, Chennai 600127, India
[2]Department of Physics, National Institute of Technology, Jamshedpur, India
*(*Email: rishabh.raj50@gmail.com; navamathavan.r@vit.ac.in)*

ABSTRACT

By optimizing processing parameters of recorded holograms, ultra violet and infrared radiation of solar spectrum can be filtered out by a single HOE enabling visible range of solar radiation to be transmitted to interiors of buildings.

Keywords:Daylighting, Solar radiation, Holographic optical element, Holographic lens, Dispersive system.

1. INTRODUCTION

Many applications and related studies of solar energy have been focused on guiding sunlight into the interiors of building for illumination purposes. To achieve this objective, one of the approaches is the use of a solar concentrator. The quality of light in the interiors of the building is very important. In an ambient solar radiation, ultraviolet and infrared accounts for 53% of radiation[1]. Holographic optical elements(HOE) may be used advantageously to filter out ultraviolet, infrared and remaining portion of useful solar radiation to diffract into interior of buildings[2, 3]. From the architectural point of view, HOEs have certain useful properties for light transmission and radiation control. Daylighting is an effective means of reducing both lighting and cooling costs of the buildings[4, 5]. Besides, sunlight for illumination has many benefits such as good quality and healthy illumination leading to workers productivity[6]. If interior of house does not get sufficient light then persons living in such rooms may suffer from deficiency of vitamin D and hormone production is also influenced which affects the seasonal change in mood.IR radiation is moderate in solar radiation, which is responsible for producing heat inside the interior and hence not suitable for hot climate. Further, prolonged exposure to solar UV radiation may result in acute and chronic health effects on skin, eye and immune system. Due to these reason collected light for lighting interior of a building should not contain UV and IR radiation.Most conventional daylighting techniques are heavy and bulky and require maintenance and adjustment for optimal performance. Daylight holograms, however provides an effective method for the even distribution of sunlight within a room. HOE can be used to create holographic windows for daylighting application in buildings. The function of HOE in daylighting applications is to redirect sunlight from the immediate window area into the rear of the room so as to illuminate the darker regions and to reduce glare. HOEs can function as gratings, lenses or any other type of optical element. Large optical apertures, light weight, thin film geometry, and lower cost are the main feature of HOEs. HOEs are wavelength selective and hence they can also be made to operate over a narrow wavelength band. In present work theoretical design of holographic optical element has been done to filter out ultraviolet, infrared solar radiation and to allow only visible spectrum to enter inside the interior of the room. Such system provides even distribution of sunlight within interior of a building which is hygienic and supportive to human health and activities as well as reduces energy demand. Further it is also shown that by optimizing the processing parameters suitably holographic lenses may exhibit larger acceptance angle which will help to minimize solar tracking. HOE may also provide better quality, light weighed low cost device for hazard free cool radiation of daylighting interior of a building.Holographic optical elements can make a valuable contribution to architectural design by controlling light and creating new concepts of colour and space. It is attractive for architecture not only for its paradoxical representation of the 3-D space, but also for its physical characteristics, dispersion and diffraction of light.

2. THEORY

2.1 Principle of recording and reconstruction of a transmission Holographic optical element

A hologram is a photographic plate which has been exposed to laser light and produced in such a way that when illuminated appropriately it produces a 3-D image[7]. Thearrangement for recording and reconstruction of the hologram is shown in Fig.1 and 2 respectively.

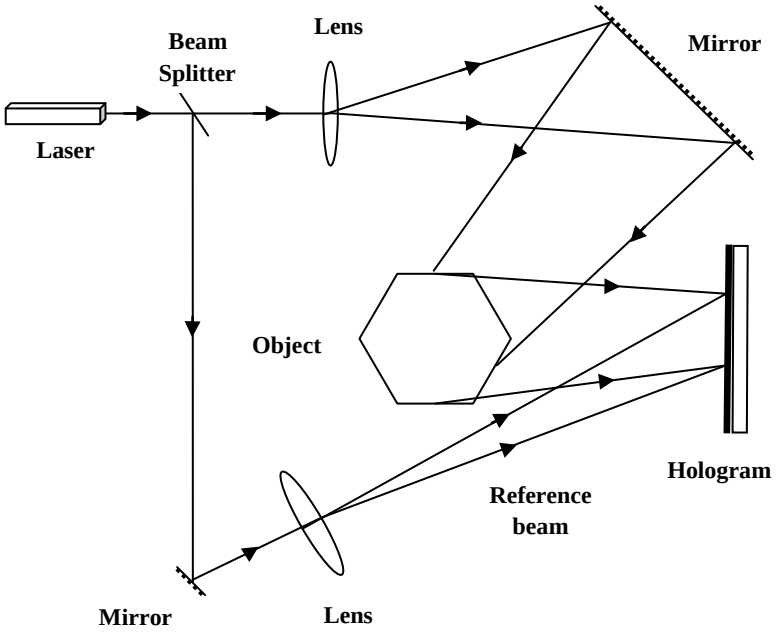

Fig. 1 Schematic of recording geometry for hologram

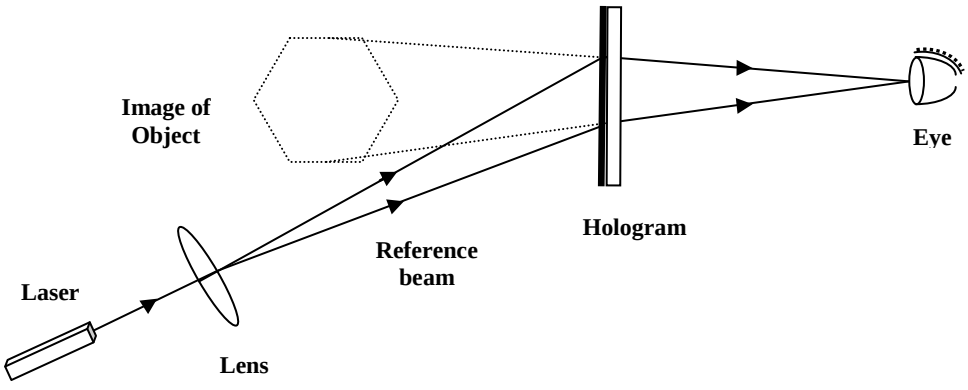

Fig. 2 Schematic of reconstruction geometry

2.2 Mathematical theory of recording and reconstruction of a hologram

To make the mathematics simple, let us take reference wave[8] as a plane wave (collimated beam) represented as

$$r(x,y) = r\exp(i2\pi\xi_r x) \quad (1)$$

The complex amplitude due to the object beam at any point (x, y) on the photographic plate can then be written as

$$O(x,y) = |O(x,y)|\exp[-i\phi(x,y)] \quad (2)$$

Where, $\xi_r = (\sin\theta)/\lambda$;

The resultant intensity at the photographic plate is given by

$$I(x,y) = |r(x,y) + o(x,y)|^2 \quad (3)$$

On solving equation (3), we get,

$$I(x,y) = r^2 + |o(x,y)|^2 + 2r|o(x,y)|\cos[2\pi\xi_r x + \phi(x,y)] \quad (4)$$

Where, the complex amplitude may be written as a real constant r.

Since the amplitude transmittance of the photographic plate after processing is linearly related to the intensity in the interference pattern, the amplitude transmission of hologram can be written as,

$$\begin{aligned} t(x,y) = t_0 + \beta T \{ & |o(x,y)|^2 \\ & + r|o(x,y)|\exp[-i\phi(x,y)]\exp[-i2\pi\xi_r x] \\ & + r|o(x,y)|\exp[i\phi(x,y)]\exp[i2\pi\xi_r x] \} \end{aligned} \quad (5)$$

Where, t_o = is a constant background transmittance

T = is the exposure time

β = is a parameter determined by thephotosensitive material used and the processing conditions

When recorded hologram is illuminated with same reference beam $r(x,y) = r\exp(i2\pi\xi_r x)$

we get transmitted wave as

$$\begin{aligned} u(x,y) &= r(x,y)t(x,y) \\ &= u_1(x,y) + u_2(x,y) + u_3(x,y) + u_4(x,y) \end{aligned} \quad (6)$$

where $u_1(x,y) = t_0 r\exp(i2\pi\xi_r x)$ (7)

$$u_2(x,y) = \beta Tr|o(x,y)|^2\exp(i2\pi\xi_r x) \quad (8)$$

$$u_3(x,y) = \beta Tr^2 o(x,y) \quad (9)$$

$$u_4(x,y) = \beta Tr^2 o^*(x,y)\exp(i4\pi\xi_r x) \quad (10)$$

The first term $u_1(x,y)$ in equation (6) is merely the attenuated reference beam, which is a plane wave directly, transmitted through the hologram. The directly transmitted beam is surrounded by a halo due to the second term $u_2(x,y)$ which is spatially varying.

The third term $u_3(x,y)$ is identical with the original object wave, except for a constant factor and generates a virtual image of the object in its original position; this wave makes an angle θ with the directly transmitted wave. The fourth term $u_4(x,y)$ gives complex conjugate to the object beam which gives real image.

Thus on reconstruction real image (complex conjugate to object wave) as well as virtual image (object wave) is generated.

Hologram of a point source generated by recording interference pattern of a plane wave and a spherical wave derived from the same laser sourcebehaves as a hololens.

3. EXPERIMENTAL

3.1 Holographic lens recording and reconstruction

Experimental setup for recording holographic lens is shown in Fig. 3.For present work a holographic lens has been recorded on commercially available high resolution silver halide plate PFG-01(film thickness d = 8 μm and average refractive index n = 1.61) using a He-Ne Laser (λ = 0.6328 μm) of power 12 mW. The recorded hologram is processed using standard procedure[9].

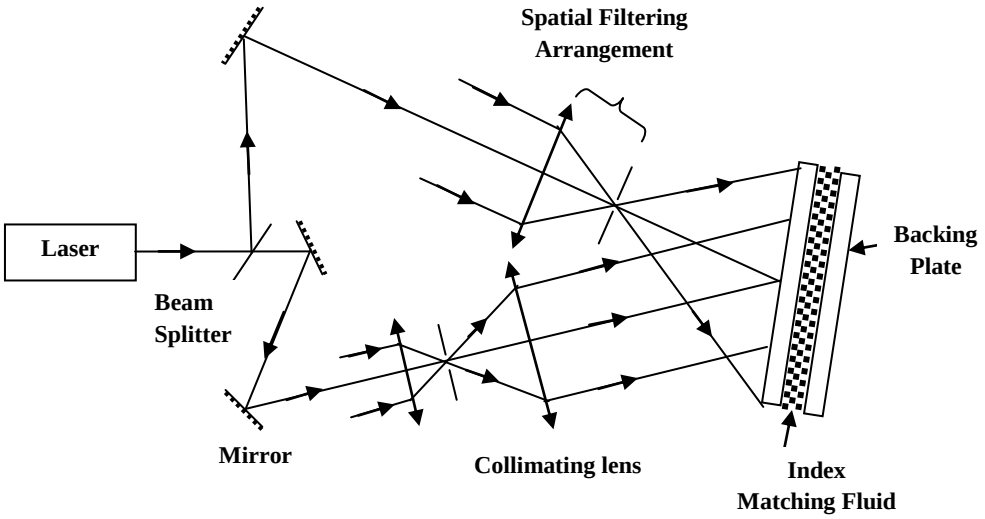

Fig. 3 Schematic of the geometry for recording holographic lens

When recorded holographic lens is illuminated with white light, chromatic dispersion will occur. Schematic of chromatic dispersion through hololens is shown in Fig. 4whereas experimental evidence is in Fig. 5.

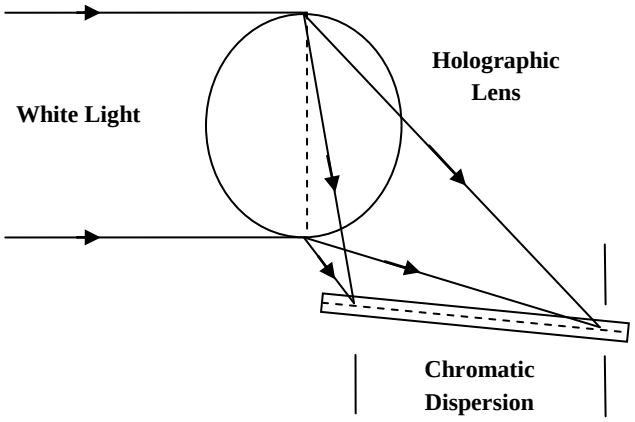

Fig. 4 Schematic of the reconstruction setup of holographic lens

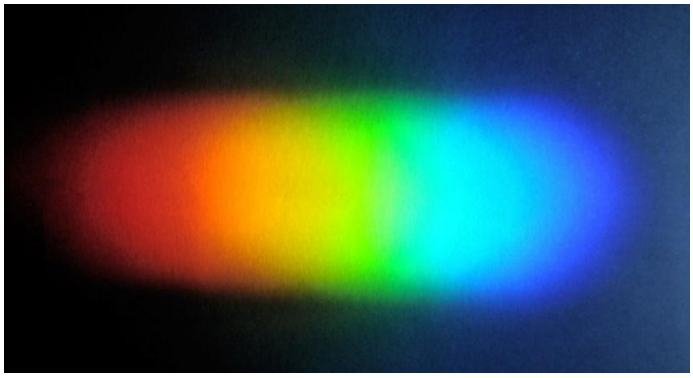

Fig. 5 Photograph of the Spectrum of white light diffracted by a typical holographic lens

4. SIMULATION

4.1 Optimization of processing parameters for filtering UV & IR radiation

The formula for diffraction efficiency (η) of thick phase transmission holographic lens, which is illuminated (reconstructed) at Bragg's angle is given by coupled wave theory[10] assuming refractive index variation to be sinusoidal as

$$\eta = \sin^2 \nu \qquad \text{where, } \nu = \frac{\pi n_1 d}{\lambda \cos\theta} = \frac{\pi n_1 d}{\lambda \sqrt{1-\sin^2\theta}} \quad (11)$$

Here n_1 is the depth of refractive index modulation, d is the film thickness, λ is the free space wavelength of the reconstruction light beam and θ is Bragg's angle.

Bragg's angle 'θ' is related to the fringe spacing (Λ), recorded in the holocons through the relation given by

$$\sin\theta = \frac{\lambda}{2n\Lambda} \quad (12)$$

Thus for illumination/reconstruction at Bragg's angle, diffraction efficiency (η) can be given as

$$\eta = \sin^2 \left(\frac{\pi n_1 d}{\lambda \left\{ 1 - \left(\frac{\lambda}{2n\Lambda} \right)^2 \right\}^{\frac{1}{2}}} \right) \quad (13)$$

Using Eq. (13) variation in diffraction efficiency (η) for a holocon with wavelength at Bragg's angle for different values of depth of refractive index modulations of holocon recording has been plotted. While drawing the curves care has been taken to ensure that criteria for thick phase transmission holographic lens are fulfilled for which Eq. (13) holds good. A holographic lens is said to be thick if its Q parameter $\left(Q = \frac{2\pi\lambda d}{n\Lambda^2} \right)$ is greater or equal to 10.

Wavelength selective properties of holographic lenses can be controlled by varying film thickness and depth of refractive index modulation. Fig. 6 reveals that properly recorded holographic lens can efficiently split up white light into its constituent wave lengths with reasonably good diffraction efficiency. Further tracking requirement of holographic lenses can also be minimized by proper optimizing the processing parameters.

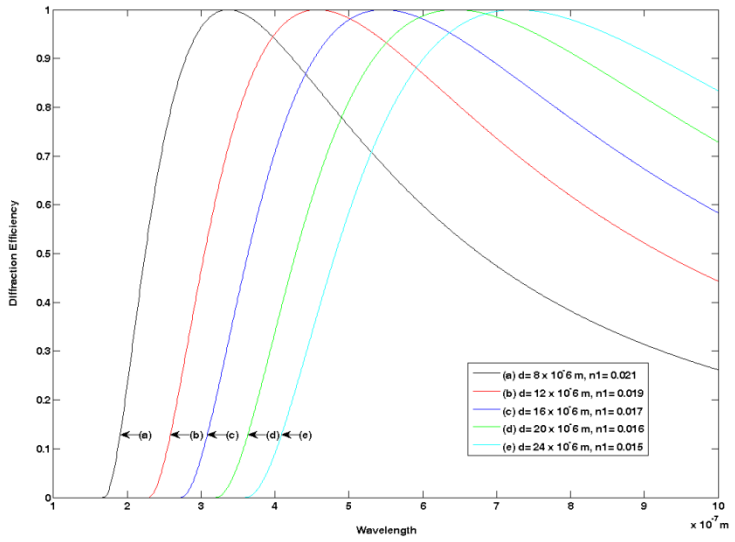

Fig. 6 Variation of diffraction efficiency with wavelength for different values of film thickness and depth of refractive index modulation (n_1) at fixed value of Λ =1.66 μm& n=1.61.

5. CONCLUSION

Present investigation reveals that properlydesigned holographic optical elements may disperse and transit solar spectrum into interior of building. This ensures that HOE may provide better quality, light weighed, low cost device for hazard free (UV & IR) cool radiation of daylighting interior of a building.

REFERENCES

[1] Lavery, N.P., "Mathematical framework for predicting solar thermal build-up of spectrally selective coatings at the Earth's surface," Applied Mathematical Modelling 31, 1635–1651 (2007).

[2] Ludman, J.E., "Holographic Solar Concentrators", Appl. Opt. 21, 3075 (1982).

[3] Ghosh, Abhijit, Ranjan, R., Nirala, A.K., Yadav, H.L., "Design and analysis of processing parameters of hololenses for wavelength selective light filters," Optik 125, 2191–2194 (2014).

[4] Benton, C.C., "Daylighting can improve the quality of light and save energy," Architectural Lighting 1, 46-48 (1986).

[5] Whang, A.J.-W., Chen, Y.-Y., and Wu, B.-Y, "Innovative design of cassegrain solar concentrator system for indoor illumination utilizing chromatic aberration to filter out ultraviolet and infrared in sunlight," Solar Energy 83, 1115-1122 (2009).

[6] Oddo, S., "Surprising discoveries about why you need more natural light," House and Garden 148, 78–79 (1976).

[7] Hui, Sam C.M., and Muller, Helmut F.O., "Holography: Art and Science of Light in Architecture," Architectural Science Review 44, 221-226 (2001).

[8] Hariharan, P., [Optical Holography], Cambridge University Press, Cambridge, 13-15 (1984).

[9] Saxby, G., [Practical Holography], Prentice hall international, UK (1985).

[10] Kogelnik, H., "Coupled wave theory for thick hologram grating," Bell Syst. Technol. J. 48,2909–2947 (1969).

Imaging characteristics of a birefringent lens with primary spherical aberration under broadband illumination

Surajit Mandal
Department of Electronics & Communication Engineering,
B. P. Poddar Institute of Management & Technology,
137, V.I.P. Road, Kolkata-700052, India

ABSTRACT

This paper reports the imaging behavior of an optical system consisting of a uniaxial birefringent lens sandwiched between two linear polarizers suffering from primary spherical aberration. The optic axis of the birefringent crystal is perpendicular to the lens axis. The said system is illuminated with a polychromatic beam of light having flat-top spectral profile and the quality of image formed by the system is evaluated by means of the intensity point spread function (IPSF) and optical transfer function (OTF). The proposed system has high tolerance to primary spherical aberration under broadband illumination.

Keywords: Image evaluation, optical design, birefringence, uniaxial crystal lens, OTF, IPSF, spherical aberration characteristics.

1. INTRODUCTION

Optical systems with high depth of focus and less effect of spherical aberration are often used for many practical applications in robotics, microelectronics, microscopy and medical imaging. The use of optical filters at the pupil plane of the objective is one of the standard methods for correcting aberrant images and to increase the focal depth of the system. Welford[1] successfully employed annular apertures for achieving large focal depth of the optical imaging systems. Mino and Okano[2] reported that the judicious use of an apodizer may increase the focal depth without significant image degradation. The use of semitransparent and phase annuli to enhance the resolving power as well as focal depth of optical instruments was suggested by Taylor *et al.*[3] Tsujiuchi[4] and Asakura *et al.*[5-7] pointed out that an appropriate modification of the pupil function of the optical systems may also lead to a suppression of the residual aberrations inherent in the unmasked pupil. The use of spatial filters for achieving a high focal depth as well as for simultaneous reduction of the effects of spherical aberration as reported by Castaneda *et al.*[8-11] needs special mention. Recently, Mezouari *et al.*[12] employed phase filters for reduction of defocus and spherical aberrations. Comparative studies of the effects of amplitude-only, phase-only and complex filters on the pupil plane reveal that phase masks are undoubtedly more effective than amplitude masks. However, practical implementation of such filters is beset with technological problems.

In the recent past we reported an alternative approach for generation of complex filter at the pupil plane of an optical system consisting of a uniaxial birefringent lens sandwiched between two linear polarizers under strictly monochromatic illumination.[13-16] A uniaxial crystal lens with its optic axis perpendicular to the principal axis of the system has two foci, one for the ordinary rays and the other for the extraordinary rays and these two foci are longitudinally separated along the system axis. Such a lens, when placed between two linear polarizers at suitable orientations, behaves as an ordinary lens with a radially varying complex mask at the pupil plane.[13,14] The nature of this virtual mask and hence the imaging and focusing characteristics of the said system may be modified by changing the design parameters of the birefringent lens and/or the orientation of the transmission axes of the two polarizers included in the system. Since this complex virtual mask is generated on the lens aperture as a result of an interference phenomenon, it is self-aligned and no light loss occurs due to scattering in the masking element. [13,14] The construction of our proposed system is shown in Fig. 1.

The imaging and focusing characteristics of aberration-free birefringent lenses under broadband illumination were reported in some of our previous publications.[17-19] The proposed system exhibits high depth of focus for large spectral

surajitmandal@yahoo.co.in; telefax: +91-33-25739401

spread of the polychromatic input illumination.[17] A single system may provide both enhanced resolution and apodization properties as revealed by the polychromatic IPSF and polychromatic OTF curves.[18,19] The said system also has larger depth of focus than an equivalent isotropic lens in presence of primary spherical aberration and this property does not change significantly when illuminated with a polychromatic source of light.[20] However, the polychromatic image quality of the birefringent lens in presence of primary spherical aberration was not studied in detail. Here, we intend to study the imaging characteristics of the birefringent lens with primary spherical aberration under polychromatic input illumination having flat-top spectral profile.

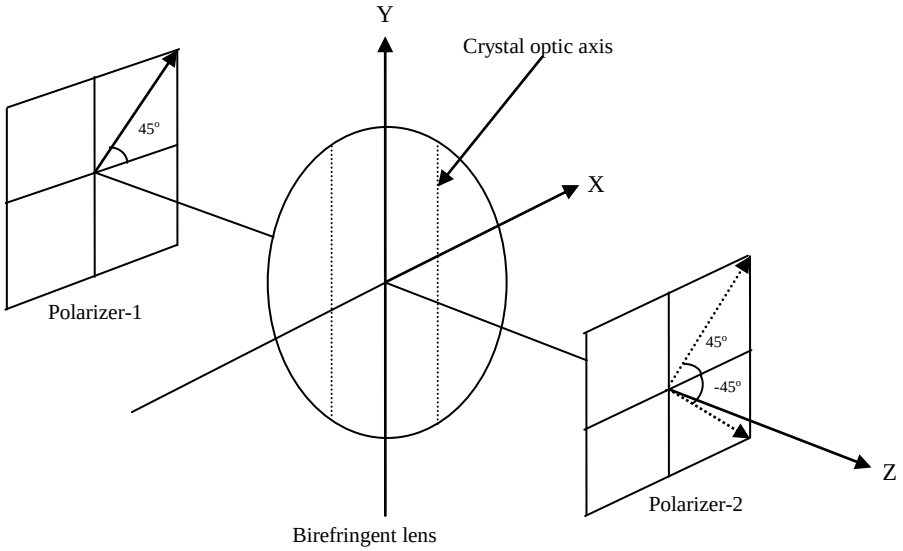

Figure 1. Construction of the proposed system

2. MATHEMATICAL FORMULATION

In presence of primary spherical aberration and defocus, the effective pupil function of the proposed system for both parallel- and crossed-polarizer configuration is given by[16]

$$\Omega_{-}^{+}(r,\alpha,\overline{W}_{20},W_{40}) = \begin{matrix}\cos\\ \sin\end{matrix}\left[k\,\alpha\,\left(1-r^2\right)\right]e^{\,i\,k\left(\overline{W}_{20}\,r^2+W_{40}\,r^4\right)} \tag{1}$$

where $k=2\pi/\lambda$ is the propagation constant, W_{40} is the primary spherical aberration coefficient, $\overline{W}_{20}=W_{20}-\sigma$ is the effective defocus and W_{20} is the defocus coefficient. $\alpha=\delta n\Delta/2$ and $\sigma=(\bar{n}-1)\Delta=2(\bar{n}-1)\alpha/\delta n$ are two design parameters of the birefringent lens, $\delta n=n_e-n_o$ is the birefringence of the lens material, $\bar{n}=(n_o+n_e)/2$ is the mean refractive index of the lens material and Δ is the central thickness of the lens.[13-15]

For a polychromatic input illumination having flat-top spectral profile with mean wavelength λ_0 and a spread of $2\delta\lambda$, the corresponding IPSF is obtained as

$$\mathrm{IPSF}_{-\,poly}^{+}=\frac{4}{2\,\delta\lambda}\int_{\lambda_0-\delta\lambda}^{\lambda_0+\delta\lambda}\left[\int_0^1\begin{matrix}\cos\\ \sin\end{matrix}\left[k_\lambda\alpha_\lambda\,(1-r^2)\right]\cos\left[k_\lambda\{(W_{20}-\sigma_\lambda)\,r^2+W_{40}r^4\}\right]J_0(\rho_\lambda r)rdr\right]^2 d\lambda$$

$$+\frac{4}{2\,\delta\lambda}\int_{\lambda_0-\delta\lambda}^{\lambda_0+\delta\lambda}\left[\int_0^1\begin{matrix}\cos\\ \sin\end{matrix}\left[k_\lambda\alpha_\lambda\,(1-r^2)\right]\sin\left[k_\lambda\{(W_{20}-\sigma_\lambda)\,r^2+W_{40}r^4\}\right]J_0(\rho_\lambda r)rdr\right]^2 d\lambda \tag{2}$$

The monochromatic OTF for the system is obtained from the autocorrelation of the pupil function. The polychromatic OTF of our proposed system in presence of primary spherical aberration and defocus comes out as

$$\mathrm{OTF}^{+}_{-poly} = \frac{1}{\int_{\lambda_1}^{\lambda_2} N^{+}_{-}(\alpha_\lambda)\,d\lambda} \int_{\lambda_1}^{\lambda_2} \int_{x=0}^{a_\lambda} \int_{y=0}^{b_\lambda} \Bigg[\cos\left\{ 4k_\lambda W_{40} s_\lambda x \left(x^2 + y^2 + \frac{{s_\lambda}^2}{4} \right) + 2k_\lambda \left(\overline{W}_{20_\lambda} + \alpha_\lambda \right) s_\lambda x \right\}$$

$$+ \cos\left\{ 4k_\lambda W_{40} s_\lambda x \left(x^2 + y^2 + \frac{{s_\lambda}^2}{4} \right) + 2k_\lambda \left(\overline{W}_{20_\lambda} - \alpha_\lambda \right) s_\lambda x \right\}$$

$$\pm \cos\left\{ \left(2k_\lambda \alpha_\lambda + 4k_\lambda W_{40} s_\lambda x \right) \left(x^2 + y^2 + \frac{{s_\lambda}^2}{4} \right) + 2k_\lambda \overline{W}_{20_\lambda} s_\lambda x - 2k_\lambda \alpha_\lambda \right\}$$

$$\pm \cos\left\{ \left(2k_\lambda \alpha_\lambda + 4k_\lambda W_{40} s_\lambda x \right) \left(x^2 + y^2 + \frac{{s_\lambda}^2}{4} \right) + 2k_\lambda \overline{W}_{20_\lambda} s_\lambda x - 2k_\lambda \alpha_\lambda \right\} \Bigg] dx dy \qquad (3)$$

where $a_\lambda = 1 - s_\lambda / 2$, $b_\lambda = \left[1 - \left(x + s_\lambda / 2 \right)^2 \right]^{\frac{1}{2}}$ and $\overline{W}_{20_\lambda} = W_{20} - \sigma_\lambda$. $N^{+}_{-}(\alpha) = \pi \left[1 \pm \mathrm{sinc}\left(4\alpha_\lambda / \lambda \right) \right] / 2$ is the normalizing factor of the OTF for the proposed system and $\mathrm{sinc}(\chi) = \sin(\pi\chi)/\pi\chi$. In order to maintain the maximum value of the normalized spatial frequency (s) at 2, all the wavelength-dependent parameters are normalized by the terms corresponding to the minimum available value of λ in the given wavelength range.

.

3. RESULTS AND DISCUSSIONS

Previous studies[16] revealed that the birefringent lens with $\alpha = 0.285\lambda$ exhibits higher Strehl ratio at the best focal plane than that of a clear-aperture isotropic lens for monochromatic input illumination and the value is nearly uniform between spherical aberration values 0 and λ under parallel-polarizer configuration. Consequently, greater manufacturing tolerance may be permissible during the fabrication of such a lens. This motivated us to carry out a thorough investigation on the imaging characteristics of said system for this value of α under broadband illumination. In order to achieve this small value of α, the uniaxial crystal should also have low value of birefringence. For this reason crystal quartz is selected as the lens material for our present study.[21] The transmittance of this material is also very high and almost uniform within the visible range of the electromagnetic spectrum.

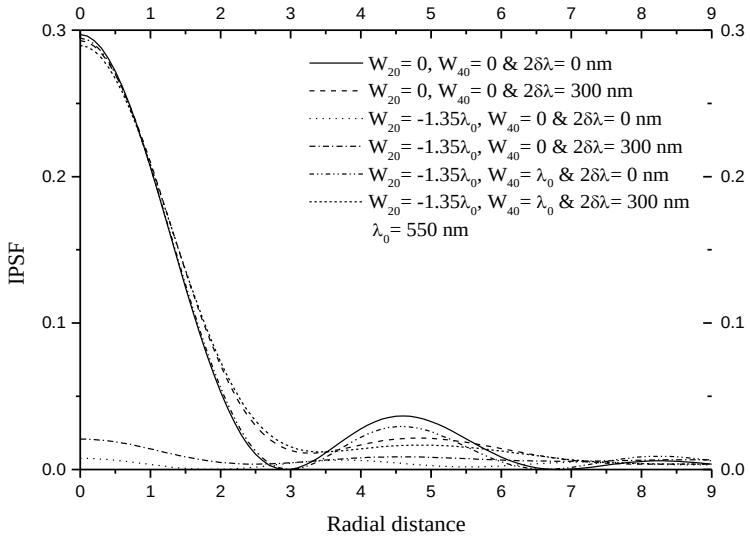

Figure 2. IPSF curves for the birefringent lens with $\alpha = 0.285\lambda_0$ under parallel-polarizer configuration

Fig. 2 depicts the variation of IPSF curves with radial distance for the birefringent lens having $\alpha = 0.285\lambda_0$ under parallel-polarizer configuration at the mean wavelength $\lambda_0 = 550\,\text{nm}$ for different spectral spreads. As evident from the figure, The IPSF curve at the Gaussian image plane does not change appreciably even when the bandwidth ($2\delta\lambda$) is 300 nm around the mean wavelength. The characteristics start deteriorating with the increase of defocus for both monochromatic and polychromatic input illumination as expected. With the introduction of spherical aberration, the system's performance is found to improve significantly. For $\overline{W}_{20} = -1.35\lambda_0$ and $W_{40} = \lambda_0$, the IPSF curves are almost similar to those obtained at the Gaussian image plane. In this connection it may be mentioned that the image plane corresponding to $\overline{W}_{20} = -1.35\lambda_0$ is the best focal plane for this birefringent lens when $W_{40} = \lambda_0$.

The OTF curves for different spectral spreads ($\Delta\lambda = \lambda_2 - \lambda_1$) of the polychromatic beam of light under parallel-polarizer configuration are shown in Fig. 3 when $\alpha = 0.285\lambda_1, \overline{W}_{20} = -1.35\lambda_1, W_{40} = \lambda_1$ and $\lambda_1 = 400\,\text{nm}$. The same under crossed-polarizer configuration are drawn in Fig. 4 corresponding to its best focal plane ($\overline{W}_{20} = -0.83\lambda_1$ and $W_{40} = \lambda_1$). As evident from the figures, the birefringent lens with $\alpha = 0.285\lambda_1$ yields suppression of low-middle frequencies and enhancement of high frequencies under parallel-polarizer configuration for both monochromatic and polychromatic input illumination. On the contrary, a less transmission of high frequencies with an enhancement of low frequencies takes place under crossed-polarizer configuration. Thus, a single system may be used for enhanced resolution with parallel-polarizer configuration and apodization with crossed-polarizer configuration under broadband illumination. As mentioned earlier,[17] the said system has larger depth of focus than an a conventional lens under similar conditions. Thus, the birefringent lenses suffering from primary spherical aberration may show the same properties as exhibited by an aberration-free birefringent lens. It is concluded that the proposed system may be suitable for different applications in robotics, microelectronics, microscopy and medical imaging.

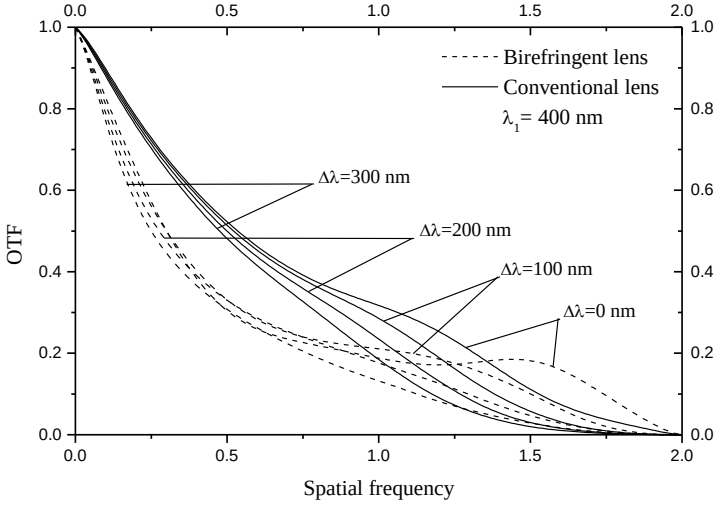

Figure 3. OTF curves for the birefringent lens with $\alpha = 0.285\lambda_0$ under parallel-polarizer configuration

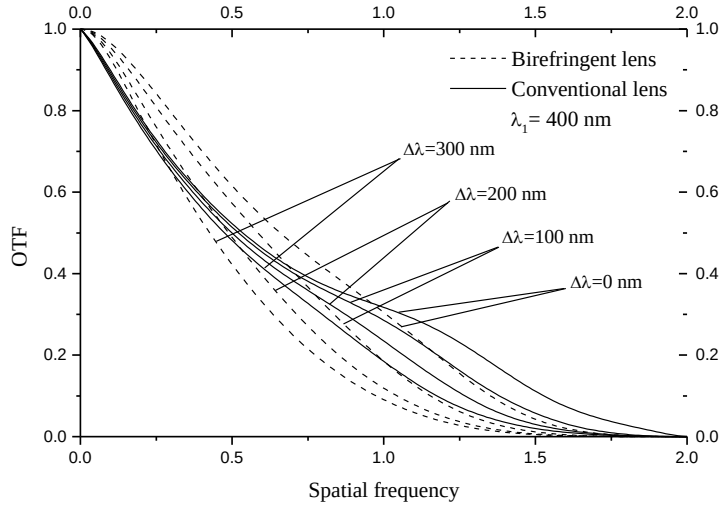

Figure 4: OTF curves for the birefringent lens with $\alpha = 0.285\lambda_0$ under crossed-polarizer configuration

REFERENCES

[1] Welford W. T., "Use of annular aperture to increase focal depth," J. Opt. Soc. Am. 50 (8), 749-752 (1960).

[2] Mino M. and Okano Y., "Improvement in the OTF of a defocused optical system through the use of shaded apertures," Appl. Opt. 10 (10), 2219-2225 (1971).

[3] Taylor C. A. and Thompson B. J., "Attempt to investigate experimentally the intensity distribution near the focus in the error-free diffraction patterns of circular and annular apertures," J. Opt. Soc. Am. 48 (11), 844-846 (1958).

[4] Tsujiuchi J., "A density filter improving aberrant optical image," J. Phys. Soc. Jpn. 12 (6), 744-752 (1957).

[5] Asakura T. and Barakat R., "Annular and annulus apertures with spherical aberration and defocusing," Oyo Butsuri 30 (10), 728-735 (1961).

[6] Asakura T., "Axial intensity distribution for an annular aperture with primary spherical aberration," Oyo Butsuri 31 (3), 243-244 (1962).

[7] Asakura T. and Mishina H., "Irradiance distribution in the diffraction patterns of an annular aperture with spherical aberration and coma," Jpn. J. Appl. Phys. 7 (7), 751-758 (1968).

[8] Ojeda-Castaneda J., Berriel-Valdos L. R. and Montes E., "Line-spread function relatively insensitive to defocus," Opt. Lett. 8 (8), 458-460 (1983).

[9] Ojeda-Castaneda J., Berriel-Valdos L. R. and Montes E., "Spatial filter for increasing the depth of focus," Opt. Lett. 10 (11), 520-522 (1985).

[10] Ojeda-Castaneda J., Andres P. and Diaz A., "Annular apodizers for low sensitivity to defocus and to spherical aberration," Opt. Lett. 11 (8), 487-489 (1986).

[11] Ojeda-Castaneda J. and Berriel-Valdos L. R., "Arbitrarily high focal depth with finite apertures," Opt. Lett. 13 (3), 183-185 (1988).

[12] Mezouari S. and Harvey A. R., "Phase pupil functions for reduction of defocus and spherical aberrations," Opt. Lett. 28 (10), 771-773 (2003).

[13] Sanyal S., Bandyopadhyay P. and Ghosh A., "Vector wave imagery using a birefringent lens," Opt. Eng. 37 (2) 592-599 (1998).

[14] Sanyal S. and Ghosh A., "Imaging characteristics of birefringent lenses under focused and defocused condition," Optik 110 (11) 513-520 (1999).

[15] Sanyal S. and Ghosh A., "High focal depth with a quasi-bifocus birefringent lens," Appl. Opt. 39 (14) 2321-2325 (2000).

[16] Sanyal S. and Ghosh A., "High tolerance to spherical aberrations and defects of focus with a birefringent lens," Appl. Opt. 41 (22) 4611-4619 (2002).
[17] Mandal S., Sanyal S. and Ghosh A., "Imaging characteristics of a birefringent lens under broadband illumination," Optik 118 (7) 335-339 (2007).
[18] Mandal S. and Ghosh A., "Polychromatic intensity point spread function of a birefringent lens," Optik 123 (18) 1623-1626 (2012).
[19] Mandal S., "Evaluation of polychromatic image quality of a birefringent lens by means of optical transfer function," Optik 125 (1) 121–125 (2014).
[20] Mandal S. and Ghosh A., "The effect of broadband illumination on the imaging characteristics of a birefringent lens suffering from primary spherical aberration," J. Opt. (India) 40 (4) 198-205 (2011).
[21] Clarke D. and Grainger J. F., [Polarized Light and Optical Measurement], Pergamon Press, New York, 90, (1971).

Effect of Lattice Filling Factor for Different Material Systems on Photonic Bandgap in Two-Dimensional Structure for TM Mode Propagation

Joydeep Ghatak[1], Manasi Chakraborty[1], Arpan Deyasi[2], Subhro Ghosal[1]

[1]A.P. C College, New Barrackpore, West Bengal, INDIA
[2]RCC Institute of Information Technology, Kolkata, West Bengal, INDIA

ABSTRACT

Complete photonic bandgap having Butterworth characteristics is formed in two-dimensional photonic crystal based filter under TM mode propagation. Structure is constructed by inserting cylindrical rods in otherwise square lattice. Maxwell's equation is solved using plane wave expansion method and eigen equations for TE and TM modes are obtained using appropriate boundary conditions. Magnitude of bandgap and mid-band frequency depends on difference on the permittivity of the two materials. Ratio of dimensions of the two materials i.e., lattice filling factor critically controls the relative position and magnitude of bandgap. Hence, design of 2D photonic crystal based bandpass filter will be tailored by choice of material system and lattice filling factor

lattice filling factor, plane wave expansion method, relative permittivity difference, 2D photonic crystal, photonic bandgap, photonic bandpass filter

1. INTRODUCTION

Photonic crystal can exhibit bandgap for certain frequency ranges by restricting propagation of e.m waves in one, two or three-dimensions[1]. This property can efficiently be used in optical communication[2] and information processing[3] replacing existing counterparts due to superior performance. Among the different structures, 1D photonic crystal is studied a lot in recent days due to ease of theoretical computation[4-5] with lack of confinement in other two spatial directions. Since three-dimensional microstructures are not easy to realize in IR and optical spectra, and analysis of its properties is very difficult from computational point-of-view also; hence attention has recently been focused on the properties of 2D crystal[6]. Moreover, performance of photonic filter greatly depends on the material parameters, and hence choice of the suitable composition becomes critically important prior to fabrication[7]. Hence calculation of band structure becomes extremely important along with accurate estimation of the photonic bandgap width with relative position in frequency scale.

Existence of photonic bandgap in 2D structure is experimentally verified after theoretical predictions a decade ago[8]. Researchers studied the effect of defect on TE and TM mode propagations to observe modification in bandgap[9]. Different numerical methods are also proposed very recently to compute PBG in defected structures[10-11]. El-Dahshory et. al. framed design equations 2D PBG structures using full wave analysis from PWM approach considering the physical dimensions[12]. Magnitude of PBG is also computed for asymmetric structure[13]. However, effect of filling factor on magnitude and relative position of photonic bandgap for particular mode is not studied as far the knowledge of the authors.

In this paper, band structure of 2D photonic crystal is computed using plane wave expansion method for three different material systems considering TM mode propagation. Results show the dependence of bandgap width and mid-band frequency on relative permittivity difference of the constituent materials. Simulation also exhibits that bandgap width critically depends on the lattice filling factor, which will play pivotal role in designing photonic crystal based filter for optical signal processing.

2. MATHEMATICAL MODELING

Maxwell's equation for e.m wave propagation can be written as:

$$\nabla \times \frac{1}{\varepsilon(r)} \nabla \times \vec{H}(r) = \frac{\omega^2}{C^2} \vec{H}(r) \tag{1}$$

Using Bloch's theorem, mode in a periodic structure can be expressed as a sum of infinite number of plane waves:

$$H(r) = \sum_{\vec{G}_i, \lambda} h_{G_i, \lambda} e^{i(\vec{k}+\vec{G}_i).\vec{r}} \hat{e}_\lambda \tag{2}$$

where λ=1, 2, also k denotes the wave vector of the plane wave, $\vec{G}$ is the reciprocal lattice vector , $\hat{e}_\lambda$ is used to denote the two unit axis perpendicular to the propagation direction $\vec{k}+\vec{G}$, $h_{G_i,\lambda}$ is used to represent the coefficient of the H component along the axes $\hat{e}_\lambda$. One thing may be noted that ($\hat{e}_1, \hat{e}_2, \vec{k}+\vec{G}$) are perpendicular to each other. Now, using the Fourier transform, the dielectric function can also be written as

$$\varepsilon(\vec{G}) = \frac{1}{V} \iiint_{\Omega} \varepsilon(r) \exp(-i\vec{G}.r) \tag{3}$$

where Ω is the unit cell and V is the volume of the unit cell. Helmholtz's equation can be expressed in the form of standard eigenvalue problem

$$\sum_{\vec{G}'} |k+G\|k+G'| \varepsilon^{-1}(G-G') \begin{bmatrix} \hat{e}_2\hat{e}_2' & -\hat{e}_2\hat{e}_1' \\ -\hat{e}_1\hat{e}_2' & \hat{e}_1\hat{e}_1' \end{bmatrix} \begin{bmatrix} h_1' \\ h_2' \end{bmatrix} = \frac{\omega^2}{C^2} \begin{bmatrix} h_1 \\ h_2 \end{bmatrix} \tag{4}$$

Here, $\begin{bmatrix} \hat{e}_2\hat{e}_2' & -\hat{e}_2\hat{e}_1' \\ -\hat{e}_1\hat{e}_2' & \hat{e}_1\hat{e}_1' \end{bmatrix}$ matrix gives us the direction of the wave vector propagation when it strikes a lattice site; i.e. causes diffraction on hitting a Bragg plane in the first Brillouin zone. $\begin{bmatrix} h_1' \\ h_2' \end{bmatrix}$ is an N × 1 matrix which satisfies the number of plane waves that is being considered. Since Eq. (4) is identical for both TE and TM modes, total number of equations can be reduced from 2N to N. Then eigen equation can be approximated to a N × N equation group

$$\sum_{G'} |k+G\|k+G'| \varepsilon^{-1}(\vec{G}-\vec{G}') = \frac{\omega^2}{C^2} h(\vec{G}) \tag{5}$$

Here, D and H are in the x and y plane respectively.

In case of oblique incidence or in-plane propagation, both K and G are in the same x-y plane, which leads to the following simplifications

$$\begin{bmatrix} \hat{e}_2\hat{e}_2' & -\hat{e}_2\hat{e}_1' \\ -\hat{e}_1\hat{e}_2' & \hat{e}_1\hat{e}_1' \end{bmatrix} = \begin{bmatrix} 1 & 0 \\ 0 & \cos(\theta-\theta') \end{bmatrix} \tag{6}$$

i.e., the 2N × 2N equation group is decoupled into two equation groups: the TE and TM. Among them, one group only contains H component along $\hat{e}_1$, and no components along $\hat{e}_2 = \hat{z}$, and so is called TM wave. It can be formulated as:

$$\sum_{G'} |k+G||k+G'|\varepsilon^{-1}(\vec{G}-\vec{G}')h_1(\vec{G}') = \frac{\omega^2}{C^2} h_1(\vec{G}) \tag{7}$$

3. RESULTS & DISCUSSION

Using Eq.(7) derived in earlier section, band structure of 2D photonic crystal is computed and plotted for three different material systems considering TM mode propagation for identical lattice filling factor (r = 0.2a), shown in Fig 1. From the plot, it is shown that with increase of permittivity of the outer layer (by suitable choosing different materials) w.r.t the direction of wave propagation keeping the other material same; magnitude of photonic bandgap increases. Also the number of forbidden region increases inside the first Brillouin zone along with increase in permittivity. Simulation is carried out for air-SiO2, air-Alumina and air-Si system as graphically represented in Fig. 1a, Fig. 1b and Fig. 1c respectively.

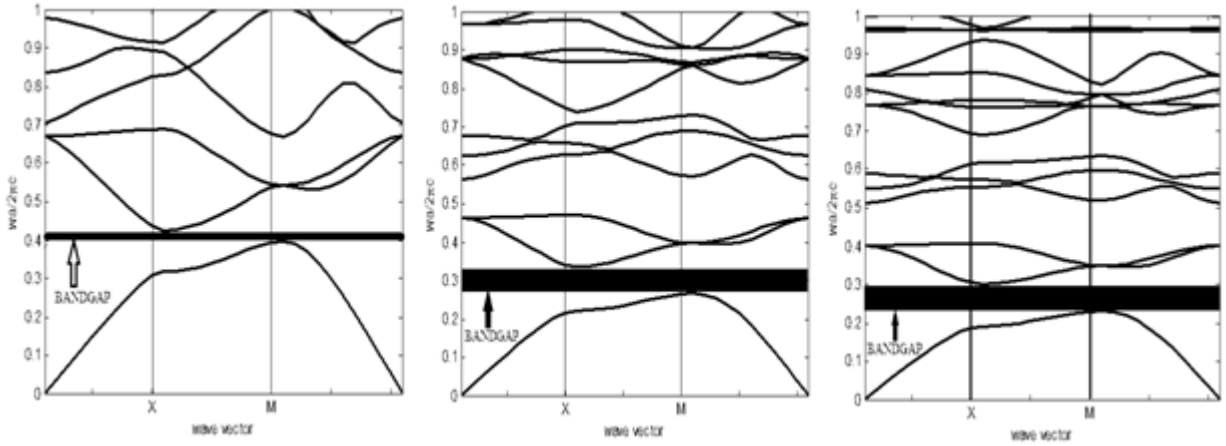

Fig 1: Band structure of 2D photonic crystal for (a) air-SiO_2, (b) air-alumina, (c) air-Si system for TM mode propagation

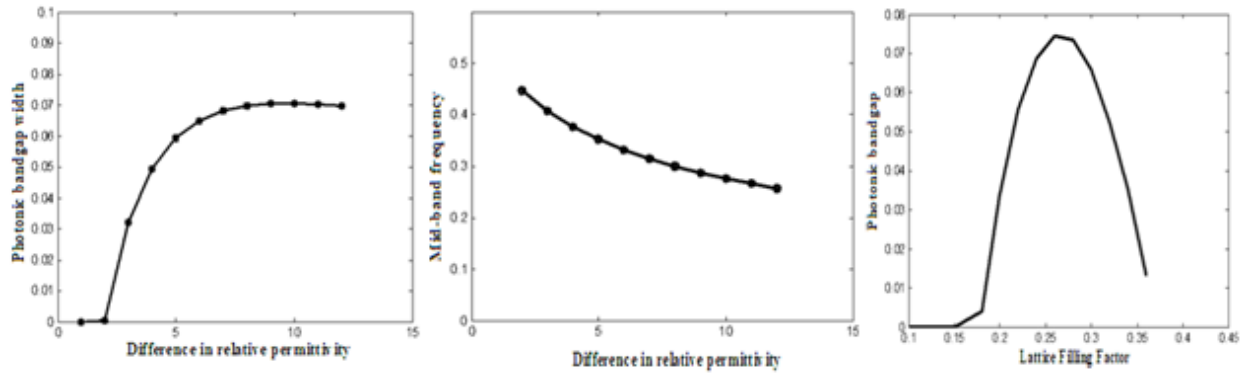

Fig 2:(a) Photonic bandgap with relative permittivity difference; (b) Mid-band frequency with relative permittivity difference; (c) Photonic bandgap with lattice filling factor

Observation reveals that with increase of relative permittivity contrast, extent of photonic bandgap first increases, and then becomes almost constant. This is exhibited in Fig 2a. Also as the difference of permittivity increases, mid-stopband frequency (in normalized scale) decreases as evident from Fig 2b which is very important in designing bandpass filter for photonic

integrated circuit. The stopband shows excellent Butterworth feature due to almost absence of any ripple. Here one key feature may be noted down that for TE mode propagation, complete bandgap is not formed, as for this mode, displacement vector is oriented along the surface of the plane ($\vec{D}(\vec{r}).\hat{z} = 0$) whereas they are perpendicular for TM mode. Splitting is observed at X and M points due to band repulsion.

Lattice filling factor is one of the important parameter for designing photonic crystal as it determines the size of the cylinders w.r.t crystal lattice constant. By increasing the size of cylinders inside the square lattice, it is observed that extent of photonic bandgap enhances for TM mode propagation upto a critical ratio. Further increment of cylinder size reduces the bandgap. Results are computed and plotted in Fig 3 for three different ratio values. The nature of bandgap with lattice filling factor is graphically represented in Fig 2c. From the plot, it may be noted that with increasing the filling factor, photonic bandgap increases, reaches at a peak value, and then starts decreasing. Hence magnitude of bandgap can be tuned by controlling the lattice filling factor, which solely depends on the dimensions of the layers. Since complete bandgap formation is not possible in TE mode, hence this effect is pronounced for TM mode propagation only.

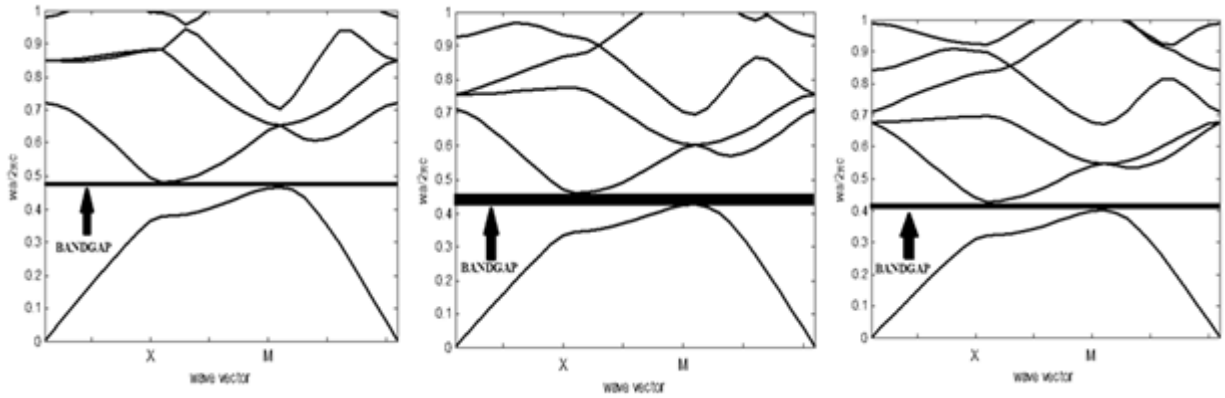

Fig 3: Photonic bandgap in 2D square lattice with air cylinders for (a) r/a=0.2, (b) r/a=0.25, (c) r/a=0.3 for TM mode propagation

Thus photonic bandgap can be tuned by varying the size of the cylinders inserted in the square lattice. It also depends on the relative permittivity differences of the constituent materials. Hence filling factor along with material composition play key roles in designing bandpass/notch filters in photonic circuit.

4. CONCLUSION

Complete photonic bandgap is formed in two-dimensional photonic crystal for TM mode propagation whose relative position and magnitude depends on the material composition, more precisely, on their relative difference in permittivity. With increasing index difference, magnitude of bandgap becomes almost constant, though mid-stopband frequency monotonically decreases. Lattice filling factor plays key role in determining the magnitude of bandgap for any material system, and it has a critical value for obtaining highest bandgap. Results are important in designing bandpass/band-reject filters for photonic circuit with Butterworth-type characteristics.

REFERENCES

1. Andreani, L., C., Agio, M., Bajoni, D., Belotti, M., Galli, M., Guizzetti, G., Malvezzi, A., M., Marabelli, F., Patrini, M. and Vecchi, G., "Optical Properties and Photonic Mode Dispersion in Two-Dimensional and Waveguide- Embedded Photonic Crystals", Synthetic Metals, 139, 695–700 (2003).
2. D'Orazio, A., De Palo, V., De Sario, M., Petruzzelli, V. and Prudenzano, F., "Finite Difference Time Domain Modeling of Light Amplification In Active Photonic Bandgap Structures", Progress In Electromagnetics Research, PIER39, 299-339 (2003).

3. Russell, P., S., J., “Photonic-Crystal Fibers”, Journal of Lightwave Technology, 24, 4729-4749 (2006).
4. Prasad, S., Singh, V. and Singh, A., K., “To Control the Propagation Characteristic of One-Dimensional Plasma Photonic Crystal using Exponentially Graded Dielectric Material”, Progress In Electromagnetics Research M, 22, 123-136 (2012).
5. Sanga, Z., F. and Li, Z., Y., “Optical Properties of One-Dimensional Photonic Crystals containing Graded Materials”, Optics Communications, 259, 174-178 (2006).
6. Robinson, S. and Nakkeeran, R., “Photonic Crystal Ring Resonator based Add-Drop Filter using Hexagonal Rods for CWDM Systems”, Optoelectronics Letters, 7, 164-166 (2011).
7. Dyogtyev, A., V., Sukhoivanov, I., A., Rue, R., M., D., L., Dyogtyev; A., V. and Sukhoivanov, I., A., “The Influence of Photonic Cystal Parameters on Photonic Band-gaps”, Proceedings of SPIE, 7009 (2008).
8. Meade, R., D., Brommer, K., D., Rappe, A., M. and Joannopoulos, J., D., “Existence of a Photonic Bandgap in Two Dimensions”, Applied Physics Letters, 61, 5495-5497 (1992).
9. Hillebrand, R., Hergert, W. and Harms, W., “Theoretical Band Gap Studies of Two-Dimensional Photonic Crystals with Varying Column Roundness”, Physica Status Solidi (b), 217, 981-989 (2000).
10. Popescu, D., G. and Sterian, P., “FDTD Analysis of Photonic Crystals with Square and Hexagonal Symmetry”, Journal of Advanced Research in Physics, 2, 021105 (2011).
11. Badaoui, H., Feham, M. and Abri, M., “Photonic-Crystal Band-pass Resonant Filters Design using the Two-dimensional FDTD Method”, International Journal of Computer Science Issues, 8, 127-132 (2011).
12. El-Dahshory, M., A., Attiya, A., M. and Hashish, E., A., “Design Equations of Two-Dimensional Dielectric Photonic Bandgap Structures”, Progress In Electromagnetics Research, 74, 319-340 (2007).
13. Kalra, Y. and Sinha, R., K., “Modelling and Design of Complete Photonic Bandgaps in Two-Dimensional Photonic Crystals”, Pramana Journal of Physics, 70, 153-161 (2008)

Air-slice and dielectric-slot Assisted Low Loss Hybrid Plasmonic Waveguide for Sub-wavelength Optical Confinement with Long Rang Propagation

Tarun sharma and Mukesh Kumar

Department of Electronics and Communication Engineering at Thapar University, Patiala-147004,

Punjab, India

**Corresponding author: Sharma.tarun23@gmail.com, mukesh.kr@thapar.edu*

Abstract: A hybrid-Plasmonic-waveguide for nano-scale-optical-confinement is proposed which exhibits large-propagation-length with low-modal-propagation-loss. SiO_2-slot under air-slice provides us a large-propagation-length of 224-μm with low-modal-propagation-loss of 0.019- dB/μm.

OCIS CODES 250.5403 Plasmonic, 350.4233 nanophotonics and photonic crystals

Nanophotonics is promising for on-chip data processing & transmission in large-scale integrated photonic circuits. It is key for various applications in sensing and optical communication. Plasmonic waveguides and devices have been attracting an ever increasing interest. For the device integration on nanoscale, the confinement and controlling the light beyond the diffraction-limit are major issues that can be addressed by Plasmonics. However, such desirable features for 'nanophotonics' come at a cost, namely, high propagation losses associated with field penetration in metal regions. Thus, significant efforts have been directed in reducing or compensating for the inherent resistive losses of plasmonic waveguides, through elaborate geometrical/material configurations. A typical challenge for plasmonic waveguides is the trade-off between propagation loss and field confinement.

In other words, they can perform either low propagation loss with a diffused field e.g., long-range surface plasmon polaritons (SPP) or compact mode size at the expense of large losses e.g., metal–insulator–metal waveguides. Recently a novel type of plasmonic waveguide called hybrid plasmonic (HP) waveguide is proposed to attempt both low propagation loss and strong field confinement. Plasmonics as major part of the emerging field of the nanophotonics explore how electromagnetic field can be confined on the scale much smaller than the operating wavelength .Integrated Photonics circuit speed up the on chip processing information and useful in other photonics related applications [1, 2]. Plasmonic waveguide have a capability to guide optical signal in deep subwavelength scale, and can be used in the large-scale integrated photonic circuits [3, 4]. Different type of the waveguides have been proposed, among them hybrid plasmonic waveguide is found to be relatively superior [5, 6]. In this paper a hybrid plasmonic waveguide with subwavelength optical-confinement, large propagation length and low modal-propagation-loss is proposed. The low-loss guiding of hybrid plasmonic mode is reported by introducing an SiO_2 slot in the silicon under the air-slice. The reported results will be useful in realizing nanophotonic devices based on hybrid plasmonic waveguide for applications in large-scale photonic integration [7-11].

The proposed waveguide design of the Hybrid Plasmonic Waveguide is shown in the Fig.1. It consists of Air slice sandwiched between Au and Si to guide and confine the HP mode. The waveguide width is w and the thickness of the dielectric (Air) is t_d. To form an HP mode the coupling of field confined in the Si with SPP mode is controlled through the intermediate dielectric layer between metal and Si. The appropriate choice of the dielectric which enables us the

induction of the gain, compensation of the loss in metal and increases the SPP signal propagation length. We choose Au, which have good conductivity among the metals in the wavelength range and Si, which have higher value of the relative permittivity, help to enhance more electric field in the dielectric region. The height of the Si is h_{is} = 100 nm and thickness of the gold layer is t_{au} = 100 nm. The width of the SiO_2 slot under the air slice is w_{SiO2} = 50 nm and height is 100 nm and these values are kept fixed. For low loss and strong field confinement the minimum value of thickness of air slice is t_d = 10 nm, below which the mode behaves as the SPP[8].

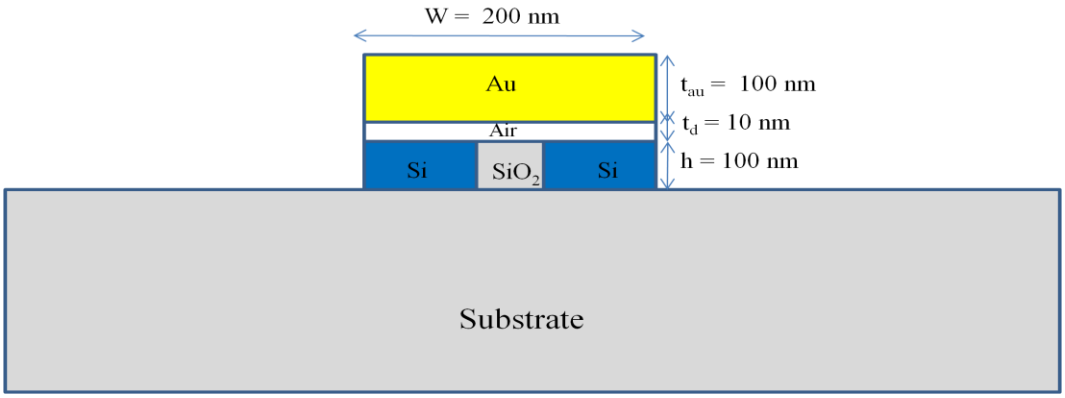

Fig.1 Proposed design of hybrid-plasmonic waveguide in which an air-slice of thickness t_{air} and width W_{air} is formed on silicon under the top gold layer of thickness 100 nm. The slot width= 50 nm and height = 100 nm is kept fixed under the air slice.

The field distribution E_y of the fundamental TM mode of the HPW, in line graph and pictorial graph, are shown in Fig.2(a) and 2(b). Fig.2(a) shows the HP field confinement when the air is there between metal and the Silicon. Fig.2(b) shows the HP field confinement when the SiO_2 is introduced below air slice in the Silicon. The real part of the refractive index is n_{eff} = 2.64 in the first case, while it is 2.59 when we introduce the SiO_2 slot below the air slice. Where w_d is the width of the waveguide. The strong field enhancement in the SiO_2 is due to the combination of SPP at Ag and SiO_2 interface and the discontinuity in the field confinement E_y from at Si-SiO_2 interface. The field will travel longer in the second case.

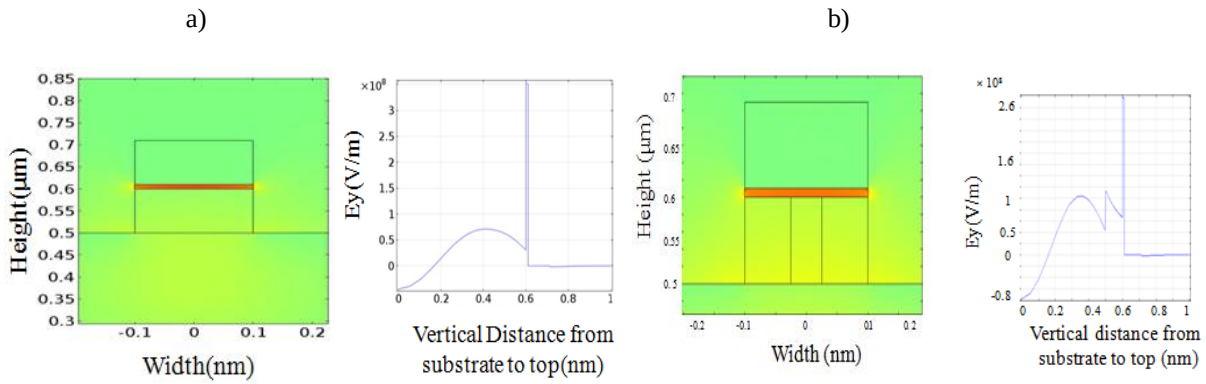

Fig.2. Field distributions E_y of the fundamental TM mode of the hybrid plasmonic waveguide (a) for hollow waveguide. Width and height of air slice are respectively 200 nm and 10 nm. The real part of the n_{eff} is 2.64 for [3](a) and it is 2.59 for (b)

Geometrical parameters of the proposed waveguide design can be significantly control the guiding performance of the HPW by observing the effect of the thickness and width of the SiO_2. The n_{eff} of the guided mode raised as the width of the waveguide increases. The simulation of the guiding characteristic is done using Finite Element Method (FEM).The propagation length for the guided hybrid HP mode is given by $L_{prop}(\mu m) = \frac{\lambda}{4\pi(neff)imaginary}$ [7], and modal propagation loss is given by $L_m(db/um) = (2K_0(img.)n_{eff}) \times 4.34$ [7], effective mode area is given as $A_m (/\mu m^2) = \frac{\int_{-\infty}^{\infty} p(x,y)dxdy}{\max[p(x,y)]}$ [8].

As we know that at t_d = 10 nm, we have tight mode confinement with lesser modal propagation loss with improved propagation length [3]. Fig.3(a). shows the variation of the propagation length with width of waveguide. It is observed that at constant dielectric thickness t_d = 10 nm, the propagation length decreases with increase in the dielectric width w_d. At w_d = 50 nm both type of waveguide have same value of the Propagation Length. As we introduced the SiO_2 slot below the air slice the propagation length enhanced with the lesser modal propagation loss. At w_d = 100 nm the L_p = 142 μm for air slice and it is L_p = 224 μm when slot is introduced. The dotted line for the air slice propagation length and solid black line for the Silica slot based Propagation Length. Fig.3(b) shows the analysis of the modal propagation loss. The modal propagation loss is decreasing with decreasing the width of the waveguide. At w_d = 100 nm we have modal propagation loss for air slice is = 0.03 dB/μm and it is 0.019 dB/μm for SiO_2 slot under the air slice.

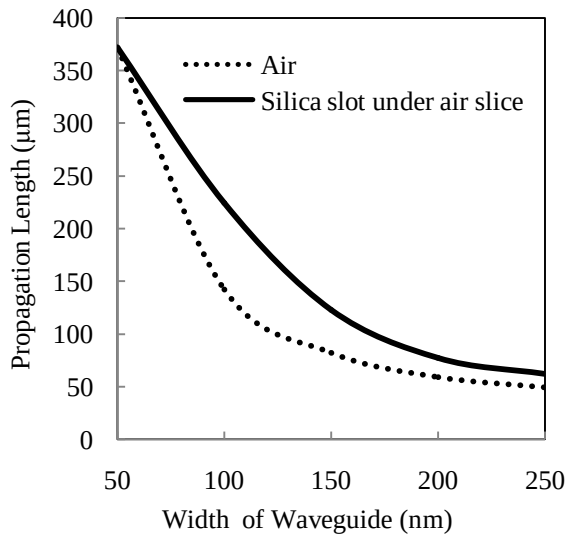

Fig.3(a)

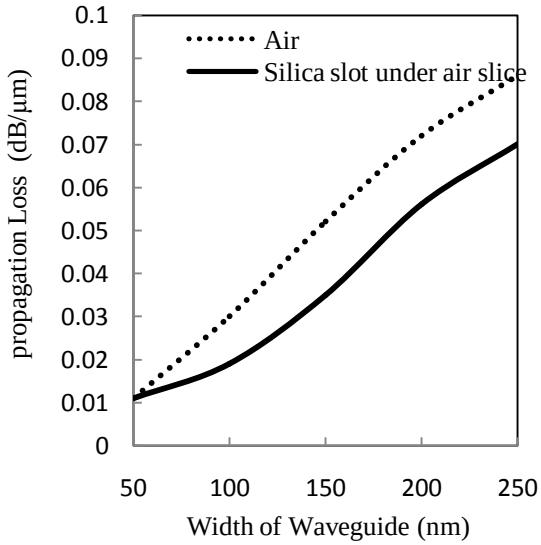

Fig.3(b)

Fig. 3(a)Variation of Propagation Length with width of air slice and with silica slot under air slice. The silica slot height and width is kept constant h_{aio2} = 100 nm and w_{SiO2} =50 nm. We kept the air slice thickness t_d = 10 nm constant.(b) Change in modal propagation loss with width of air slice and with silica slot under air slice. The silica slot height and width is kept constant h_{sio2} = 100 nm and w_{SiO2} =50 nm.

Conclusion

A nanophotonic waveguide for subwavelength optical-confinement is proposed. The Propagation characteristics of the proposed waveguide are improved by an innovative design. The introduction of the SiO_2 slot below the air slice increases the propagation length with acceptable small propagation loss. As compared to hybrid

mode compared in the air slice the SiO_2 slot based waveguide have smaller mode area A_m = 0.00023 /μm^2, larger propagation Length L_p = 224 μm and lesser modal propagation loss L_m = 0.019 dB/μm at optimized value of the width and thickness. The proposed design of waveguide is easy-to-fabricate and will be useful for the realization of the integrated nanophotonics devices for large-scale photonic integrated circuits.

6. References

[1] S. A. Maier, P. E. Barclay, T. J. Johnson, M. D. Friedman, and O. Painter, "Low-loss fiber accessible plasmon waveguide for planar energy guiding and sensing," Appl. Phys. Lett. **84** (20), 3990 (2004).

[2] S. A. Maier, P. G. Kik, H. A. Atwater, S. Meltzer, E. Harel, B. E. Koel, and A. A. G. Requicha, "Local detection of electromagnetic energy transport below the diffraction limit in metal nanoparticle plasmon waveguides," Nat. Mater. **2**(4), 229–232 (2003).

[3]. Tarun Sharma and Mukesh Kumar, "Hollow Hybrid Plasmonic Waveguide for Nanoscale Optical Confinement with Long Range Propagation", *Appl. Opt.*, vol.53, no.9, pp 1954-1957, (2014).

[4].M. Z. Alam, J. Meier, J. S. Aitchison, and M. Mojahedi, "Super mode propagation in low index medium," in Conference on Lasers and Electro-Optics/Quantum Electronics and Laser Science Conference and Photonic Applications Systems Technologies, OSA Technical Digest Series (CD) (Optical Society of America, 2007), paper JThD112.

[5]. R. F. Oulton, V. J. Sorger, D. A. Genov, D. F. P. Pile, and X. Zhang, "A hybrid plasmonic waveguide for subwavelength confinement and long-range propagation," Nat. Photonics **2**(8), 496–500 (2008).

[6]. M. Z. Alam, J. Stewart Aitchison, and Mo Mojahedi, "Theoretical Analysis of Hybrid Plasmonic Waveguide", *IEEE J. Sel. Topics Quantum Electron.*, vol. 19, no. 3, **4602008** , (2013).

[7] Yao Kou, Fangwei Ye, and Xianfeng Chen, "Low-loss hybrid plasmonic waveguide for compact and high-efficient photonic integration", *Opt. Express*, vol. 19, no.12, pp. 11746-11752, (2011).

[8] Linfei Gao, Liangxiao Tang, Feifei Hu, Ruimin Guo, Xingjun Wang, and Zhiping Zhou, "Active metal strip hybrid plasmonic waveguide with low critical material gain", *Opt. Express*, vol 20, no. 10,pp.11487-11495, (2012).

[9] Yi Song, Jing Wang, Qiang Li, Min Yan, and Min Qiu, "Broadband coupler between silicon waveguide and hybrid plasmonic waveguide" *Opt. Express*, vol 18, no. 12,pp.13173-13179, (2010).

[10] M. Z. Alam, J. Stewart Aitchison and M. Mojahedi, "Compact and silicon-on-insulator compatible hybrid plasmonic TE-pass polarizer" *Opt. Letters, Vol. 37, No. 1, 55-57(2012).*

[11] Tarun Sharma and Mukesh Kumar, "Hybridization of Plasmonic and Photonic Modes for Subwavelength Optical Confinement with Longer Propagation and Variable Nonlinearity," Accepted for the publication in the applied optics.